# Modeling the Mechanics and Failure of Discrete Viscoelastic Fiber Networks

A DISSERTATION SUBMITTED

TO THE FACULTY OF

THE UNIVERSITY OF MINNESOTA

BY

**Rohit Dhume**

IN PARTIAL FULFILLMENT OF THE REQUIREMENTS

FOR THE DEGREE OF

DOCTOR OF PHILOSOPHY

Professor Victor H. Barocas

October 2018

# Acknowledgments

As I begin writing this, I realize that there are too many people I need to thank who have helped me get where I am today, and whom I am extremely fortunate to have in my life. Clearly, I won't be able to mention everyone in this acknowledgment, but I will at least attempt to list a few who have had a major influence on me over the course of this dissertation. To everyone else who go unnamed, please know that I am eternally grateful for your support as well.

First and foremost, I want to thank my advisor and academic mentor Dr. Victor Barocas. A superb scientist, a witty wordsmith, and a wonderful human being, he has always supported me in my academic and career choices. His humility and integrity have been a true inspiration to me, and this work would not have been possible without his constant support and guidance.

Members of the Barocas lab, past and present, have been incredibly supportive and a pleasure to work with. I am grateful to Hallie Wagner, Tina Nagel, Colleen Witzenburg, Amy Claeson, and Sarah Hunt for being outstanding senior lab members, and for welcoming me in the lab. I thank Lazarina Gyoneva and Julia Quindlen for being good friends, and for patiently introducing me to the multiscale code. David Nedrelow, Chris Korenczuk, Ryan Mahutga, and Emily Bermel have all been fantastic labmates. I thank Lauren Bersei and Shannen Kizilski – the next "keepers of the code" – for all the insightful questions and countless discussions about the multiscale code. My brilliant batchmate Vahhab Zarei, deserves tremendous praise for being a great friend, and a constant companion throughout this journey.

My incredibly supportive friends in Minneapolis who made this place feel like home deserve special credit. So do the members of the UMN Squash Club who are some of the most warmhearted and welcoming people I have had the pleasure of knowing. Closer to home, I am thankful for the unconditional friendship and support of my Kharagpur friends – Rahul Das, Sridhar Iyer, Anoop S., Tushar Kumar, and

Anurag Priyam.

My family have always been a pillar of strength, and without their love and support, this dissertation would have been impossible. My uncle and aunt, Sunil and Geeta, and my cousins, Soni and Saurabh, have helped me tremendously along the way. My parents, Yeshwant and Chitra, have sacrificed a lot to help me in more ways than I can count. I am eternally grateful for their unwavering and unconditional love and support.

# Abstract

Network problems arise in all aspects of bioengineering, including biomechanics. For decades, the mechanical importance of highly interconnected networks of macromolecular fibers, especially collagen fibers, has been recognized, but models at any scale that explicitly incorporate fiber-fiber interactions into a mechanical description of the tissue have only started to emerge more recently. The mechanical response of networks shows an inherent non-linearity arising from the network architecture, and the non-affine deformations occurring within it. Thus, the overarching goal of this dissertation was to model the steady-state and time-dependent behaviors of discrete fiber networks to understand better how the behavior of an individual fiber differs from that of a network, and to study the effect of a network's structure on its mechanics. First, viscoelastic relaxation of networks composed of linear viscoelastic fibers was analyzed, throwing light on two different contributions to the network relaxation process: a material contribution due to the intrinsic viscoelasticity of the fibers, and a kinematic contribution due to the structure of the network. The effect of network composition on its relaxation spectrum was also analyzed revealing a constant evolution of structure-dependent characteristic relaxation times with changing composition. Next, network fatigue behavior was modeled using a fiber-based cumulative damage model to obtain stress-life (SN) curves for the network, and to compare fatigue behaviors of different network structures. Finally, the network model was used in a multiscale finite element approach to model actin-myosin motor-driven cell cytoskeletal contraction. The multiscale model was also used to highlight the importance of the choice of microstructure in predicting tissue pre-failure and failure behaviors.

# Contents

# List of Tables

# List of Figures

# Chapter 1

# Introduction

## 1.1 Background

Networks of different kinds are extremely common in nature (Figure 1.1). In biological systems, networks formed from interconnected fibers and filaments (e.g., collagen, elastin) greatly influence the mechanics of most load-bearing tissues, e.g., skin, tendons, ligaments. Networks of actin in the cytoskeleton of a cell allow it to make drastic changes to its shape and apply forces on its external environment. Vascular networks play an important role in the circulation of blood, and networks of neurons determines the complex response of organisms to external stimuli. To understand better these phenomena, it is crucial to gain an insight into the behavior and the effects of the underlying network structure.

In the latter half of the $20^{\text{th}}$ century, understanding the mechanics of networks became important for modeling the behavior of crosslinked polymers such as rubber under large strains and complex deformation states. The need to match the nonlinear behavior of such materials in various deformation states drove the development of constitutive equations utilizing networks. Initial attempts [Gordon, 1976] assumed

[1]Image (a) courtesy V. Lai; for more information, see [Lai et al., 2012], Image (b) courtesy P. Alford; for more information, see [Win et al., 2014], Image (c) courtesy R. Tranquillo; for more information, see [Morin et al., 2013], Image (d) courtesy V. Zarei

Gaussian statistics (i.e., the fibers never attained their fully extended length), and affine deformations to obtain an expression for strain energy. Follow-up work modified these models to include larger deformations and utilized non-Gaussian fibers in networks composed of three [Wang and Guth, 1952] and four [Flory and Rehner, 1943, Treloar, 1946] chains. This was followed by the Arruda-Boyce model [Arruda and Boyce, 1993] which used a cubic representative element with eight chains, connected to a common node at the center, extending along the main diagonals to the corners of the cube (Figure 1.2). The models assumed the tissue to deform in an *affine* manner. The affine assumption is very useful as it eliminates the need to consider microstructural interactions, and it dates back to the work of Lanir [Lanir, 1983]. Another constitutive equation assuming affine deformation was proposed by Holzapfel et al. [Holzapfel and Gasser, 2000]. This model took into account fiber alignment in the material. Subsequent modifications to this model included parameters to define concentration of fibers and distribution around a given primary direction [Driessen et al., 2005]. While the models described above performed better at capturing the mechanics of polymer networks compared to a bulk model (e.g., neo-Hookean), they were passive, and assumed the tissue to deform in an affine manner. They did not model the various network components along with their interactions individually. In reality, the deformation of networks is not necessarily affine (Figure 1.3).

More recent attempts have incorporated the non-affine motion of fibers into the network model while some have also included fiber-fiber and fiber-matrix interactions as well. These non-affine models have used networks of various geometries (selected based on histological studies, desired accuracy of the results, available computational resources, etc). Some models (lens capsule by Bird [Burd, 2008] and lung alveolar wall models by Suki et al. [Oliveira et al., 2014, Suki et al., 2012, Ritter et al., 2009, Black et al., 2008]) have used regular polygonal networks with pin joints to model the underlying collagen construct within tissues. Regular polygonal networks

violate the Maxwell constraint [Maxwell, 1864], and thus must use external constraints to stabilize the network simulation (e.g., adding a rotational energy term to the pin jointed network which essentially transforms the truss into a frame [Black et al., 2008]). Other models have chosen a more stochastic approach to generating network models, e.g., Hoger et al. [Hansen et al., 1996] used appropriately generated Delaunay networks to model the RBC cytoskeleton, Huisman et al. [Huisman et al., 2007] used a random network generation scheme to study the mechanics of networks. The methods used for simulating these fiber networks and their mechanics have also varied. Some models have represented the fibers as linear [Ritter et al., 2009, Burd, 2008, Oliveira et al., 2014] or non-linear [Black et al., 2008, Maksym et al., 1998] spring elements, some have used a molecular dynamics approach [Li et al., 2007] while others have discretized the fibers into finite beam elements, e.g., Timoshenko beam elements [Abhilash et al., 2014, Žagar et al., 2015, Ma et al., 2013]. These different models have shown that the network structure and its numerical representation are both crucial to obtain an accurate numerical representation of the tissue being modeled.

The underlying network structure becomes particularly important at large strains. Numerous experiments probing the nonlinear stress-strain response of biopolymer networks have observed a strain stiffening behavior [Gardel et al., 2004a, Gardel et al., 2004b, Shin et al., 2004, Wagner et al., 2006, Gardel et al., 2006]. This stiffening is also accompanied by an increase in the shear modulus of the network. Zagar et al. [Žagar et al., 2015] have shown that during deformation, a rigidly cross-linked network passes through two phases. The first phase occurs at low strains and is mainly bending dominated. In this phase, stretching the network leads to realignment of fibers and pulling out of fiber undulations. This phase also leads to the presence of a *toe* region in the stress-strain curve. The second phase, at large deformations, is dominated by the axial loading of fibers and cross-links. This phase leads to considerable increase in the stiffness of the network. Several studies have looked into relating this transition to

network topological parameters (e.g., [van Dillen et al., 2008] quantified the network connectivity using mean fiber length and the cross-linking density and derived a scaling relation between connectivity and network modulus). Similar scaling relations have also been derived for other types of networks (e.g., entangled networks [Picu, 2011]). Keeping in mind this influence of network geometry on its mechanics, it is thus important to identify topological measures that affect a network's response to mechanical deformation.

Biological tissues are also viscoelasatic in nature. Figure 1.4 shows the viscoelastic relaxation response observed in a collagen gel. Some viscoelastic tissue models, e.g. [Bottino, 1998] have assumed a perfectly elastic network immersed in a viscous fluid. This approach models the network mechanics as well as its interaction with the surrounding nonfibrillar matrix. Others [Tanaka and Edwards, 1992] have chosen to represent the network fibers using appropriate viscoelastic constitutive equations, e.g. as Maxwell or Kelvin-Voigt elements.

While several network models, purely elastic as well as viscoelastic, have been proposed to simulate various biological tissues, there is still a need to develop a more general network model taking into account the interactions between the fibrous and non-fibrous components. The time-dependent behavior of such networks also needs to be investigated.

## 1.2 Research aims

Several aims have shaped the course of this dissertation, and these aims have evolved over the duration of this research. The overall goal of this project was to develop an accurate model to simulate the mechanics of viscoelastic fiber networks, and to apply this model to study how non-affinity within the network architecture affects the passive mechanical characteristics, the time-dependent mechanical response, and the

failure properties of networks. Broadly, the following three aims guided the research:

- *Aim 1*: Model the viscoelastic relaxation of fiber networks to investigate the presence of structure-dependent relaxation times in the relaxation spectra
- *Aim 2*: Model fatigue failure of networks undergoing cyclic loading to study how the fatigue behavior of an individual fiber differs from that of a network, and how network architecture affects it's fatigue life
- *Aim 3*: Model active contraction of network fibers to simulate the effect of actin-myosin kinetics in the cytoskeleton of cells, and to incorporate this active fiber model in a multiscale finite element modeling method to simulate the contraction of cells fixed on substrates

## 1.3 Resulting research

The research studies resulting from the above mentioned aims form the chapters of this dissertation, and address a single aim, or a combination of aims. A brief overview of the chapters follows below.

**Relaxation spectra of viscoelastic networks (Chapter 2)**

Viscoelasticity plays an important role in the mechanical behavior of biological tissues undergoing dynamic loading. Exploring viscoelastic relaxation spectra of the tissue is essential for predicting its mechanical response. Most load-bearing tissues, however, are also composed of networks of intertwined fibers and filaments of, e.g., collagen and elastin. In this work, we showed how non-affine deformations within fiber networks affect the relaxation behavior of the material leading to the emergence of structure-dependent time scales in the relaxation spectra. In particular, we see two different contributions to the network relaxation process: a material contribution due

to the intrinsic viscoelasticity of the fibers, and a kinematic contribution due to non-affine rearrangement of the network when different fibers relax at different rates. We also present a computational model to simulate viscoelastic relaxation of networks, demonstrating the emergent time scales and a pronounced dependence of the network relaxation behavior on whether components with different relaxation times percolate the network. Finally, we observed that the simulated relaxation spectrum for Delaunay networks is comparable to that measured experimentally for reconstituted collagen gels by others.

**Fatigue failure of fiber networks (Chapter 3)**

Fatigue as a mode of failure becomes increasingly relevant with age in tissues that experience repeated fluctuations in loading. While there has been a growing focus on the mechanics of networks of collagen fibers, which are recognized as the predominant mechanical components of soft tissues, the network's fatigue behavior has received less attention. Specifically, it must be asked (1) how the fatigue of networks differs from that of its component fibers, and (2) whether this difference in fatigue behaviors is affected by changes in the network's architecture. In the present study, we simulated cyclic uniaxial loading of Voronoi networks to model fatigue experiments performed on reconstituted collagen gels. Collagen gels were cast into dog-bone shape molds and were tested on a uniaxial machine under a tension-tension cyclic loading protocol. Simulations were performed on networks modeled as trusses of, on average, 600 non-linear elastic fibers connected at freely rotating pin joints. We also simulated fatigue failure of Delaunay, and Erdős-Rényi networks, in addition to Voronoi networks,to compare fatigue behavior among different architectures. The uneven distribution of stresses within the fibers of the unstructured networks resulted in all three network geometries being more endurant than a single fiber or a regular lattice under cyclic loading. Among the different network geometries, for low to moderate external loads,

the Delaunay networks showed the best fatigue behavior while at higher loads, the Voronoi networks performed better.

**Multiscale model of contractile response of cells on substrates (Chapter 4)**

Cell cytoskeletal contraction is a crucial phenomenon in various cellular functions such as cell migration, and morphogenesis. The interconnected network of filamentous biopolymers in the cytoskeleton, notably actin, plays an important role in bearing both external loads acting on the cell, and contractile forces generated within the cell. In this study, the contractile response of the actin cytoskeleton was modeled using a multiscale approach and a discrete fiber microstructure. Tension generation within fibers was achieved by adapting a previously published 2-D phenomenological constitutive equation of actin-myosin motor kinetics. The model was used to simulate the behavior of cells fixed on concave substrates, and with appropriate calibration, it accurately captured the steady-state shape and stress-fiber distributions observed in experiments. The effect of microstructure on the steady-state configuration of the cell was also investigated using three different network architectures – Delaunay, Voronoi, and Arruda-Boyce. The steady-state shape of the cell showed a significant difference for the three microstructure choices, with the inherently affine and isotropic Arruda-Boyce-like networks showing little effect on the shape of the cell as compared to the non-affine Delaunay and Voronoi networks.

**Structure-based multiscale model of failure of porcine aorta (Chapter 5)**

The ascending thoracic aorta is poorly understood mechanically, especially its risk of dissection. To make better predictions of dissection risk, more information about the multidimensional failure behavior of the tissue is needed, and this information must be incorporated into an appropriate theoretical/computational model. Toward the creation of such a model, uniaxial, equibiaxial, peel, and shear lap tests were performed on healthy porcine ascending aorta samples. Uniaxial and equibiaxial tests showed

anisotropy with greater stiffness and strength in the circumferential direction. Shear lap tests showed catastrophic failure at shear stresses (150-200 kPa) much lower than uniaxial tests (750-2500 kPa), consistent with the low peel tension (≈60 mN/mm). A novel multiscale computational model, including both prefailure and failure mechanics of the aorta, was developed. The microstructural part of the model included contributions from a collagen- reinforced elastin sheet and interlamellar connections representing fibrillin and smooth muscle. Components were represented as nonlinear fibers that failed at a critical stretch. Multiscale simulations of the different experiments were performed, and the model, appropriately specified, agreed well with all experimental data, representing a uniquely complete structure-based description of aorta mechanics. In addition, the model demonstrates the very low strength of the aorta in radial shear, suggesting an important possible mechanism for aortic dissection.

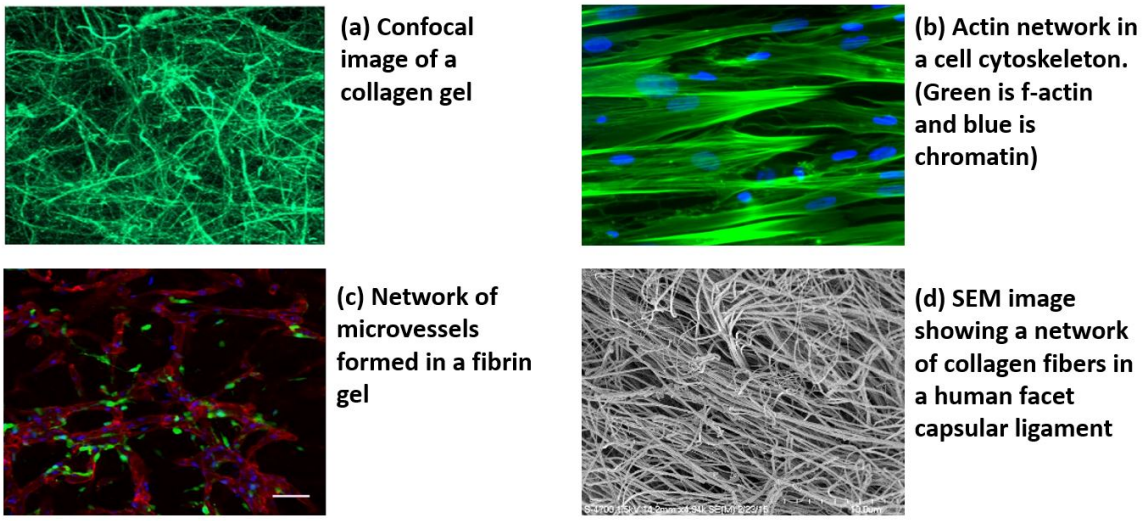


Figure 1.1: Examples of networks in nature[1]

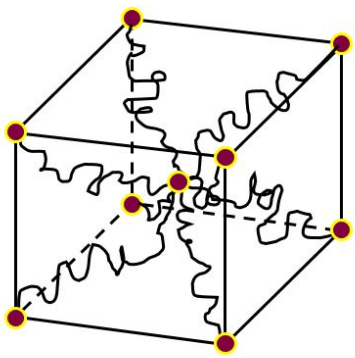

Figure 1.2: Arruda-Boyce model RVE

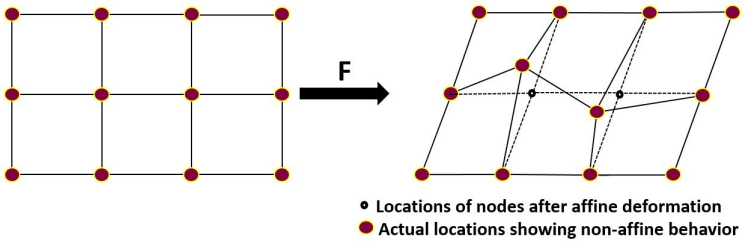


Figure 1.3: Example of non-affine deformation

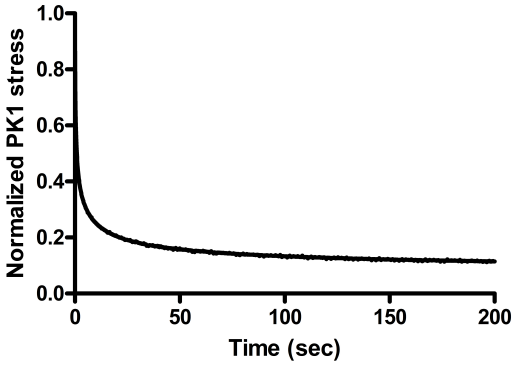


Figure 1.4: Viscoelastic relaxation behavior observed in a collagen gel (courtesy C. Korenczuk)

# Chapter 2

# Emergent Structure-dependent Relaxation Spectra in Viscoelastic Fiber Networks in Extension

## 2.1 Background

At a very basic level, a linear viscoelastic material can be modeled by combining elements with elastic and viscous mechanical characteristics, e.g., the Maxwell fluid combines a spring and a dashpot in series, and the standard linear solid has a Maxwell element and a dashpot in parallel. In such cases, under the assumption of linearity, it is straightforward to calculate a characteristic time scale over which the stress relaxes under constant strain. In general, however, a viscoelastic material can exhibit multiple relaxation time scales, and these characteristic relaxation times can depend on a variety of factors, such as magnitude of initial stress, temperature, or rate of loading, and thus more complex models are required to predict stress relaxation [Suki et al., 1994, Rogers, 1983, Koeller, 1984].

Most biological soft tissues exhibit some degree of viscoelasticity [Fung, 1981],

and their viscoelastic mechanical properties affect their characteristic functions, especially if the tissue undergoes dynamic loading, e.g., tendons, lung. Because of its analytical and experimental convinience, the stress relaxation test (i.e., monitoring stress following a step stretch) is an attractive tool. Stress relaxation also has the advantage of interrogating multiple time scales in a single experiment. Thus, the viscoelasticity of tissues has been widely studied with stress relaxation tests, including tendons [Johnson et al., 1994, Screen, 2008], ligaments [Provenzano et al., 2001, Woo et al., 1981], arteries [Zatzman et al., 1954, Gow and Taylor, 1968], and skin [Purslow et al., 1998]. To explain these experimental findings, various models have been explored, e.g., models using combinations of the Maxwell, and Voigt materials described above [Puxkandl et al., 2002]; models utilizing a simple exponential decay function [Sasaki et al., 1993, Liao et al., 2006]. By far, however, the most popular models used to explain the viscoelastic behavior of connective tissues have been based on the quasilinear viscoelastic (QLV) model developed by Fung [Fung, 1967, Edwards, 1973, Abramowitch and Woo, 2004, Sarver et al., 2003].

While viscoelastic behavior of tissues at the macroscale has been widely observed and modeled, the origins of this viscoelasticity and how it is affected by the lower hierarchical structures within the tissue are less well studied. The microstructure of many biological materials is composed of an intertwined network of fibers and filaments of, e.g., collagen, embedded in the non-fibrillar portion of the extracellular matrix. Several studies using rheological protocols have experimentally probed the non-linear viscoelastic properties of biopolymer networks, e.g., [Jabbari-Farouji et al., 2008, Broedersz et al., 2010b, Shin et al., 2004]. These studies have observed and modeled several interesting behaviors such as strain-stiffening [Münster et al., 2013, Žagar et al., 2015], crosslink-dependent stiffening [Broedersz et al., 2010a], and strain-dependent relaxation rates [Nam et al., 2016]. The majority of this existing body of work has focused on shear deformations, especially, small-strain sinusoidal oscillations

of gels in shear. The non-linear viscoleastic response under extension – which, for connective tissues is often a more relevant mode of deformation – has received less attention.

Furthermore, the heterogeneity within networks, i.e., the presence of fibers with different mechanical properties, and its effect on the viscoelastic behavior of the network has been less studied. The mechanical functionality of the network derives directly from the composition, organization, and mechanics of its microstructure. Obviously, a network composed of viscoelastic fibers will exhibit viscoelastic stress relaxation, and the characteristic time scales over which the network relaxes will be determined in large part by the rate of relaxation of the constituent fibers. We hypothesized, however, that the structure of the network can also influence the relaxation time spectrum, and it is this aspect of network relaxation which we explored in the current work. For instance, if the fibers in the network relax at different rates, the resulting changes in internal loads over time could lead to non-affine reorganization of the network fibers, which in turn could affect the overall stress relaxation behavior of the network.

## 2.2 Methods

We begin this section with a theoretical analysis of stress relaxation of a network, and then describe an approach to modeling the non-affine mechanics of a network and its stress relaxation behavior.

The convention used in the rest of this work, except when stated otherwise, is as follows: superscript indices denote node or fiber number, and subscript indices indicate direction, e.g., $f_i^n$ is the force acting on node $n$ along direction $i$, $i = 1, 2,$ or 3. The summation convention applies both to subscript and to superscript indices. This indexing convention will give rise to some terms which can be interpreted as higher

order tensors. We note that it is possible to reduce the dimensions of the tensors in subsequent equations by using indices calculated by combining the corresponding superscripts and subscripts, e.g., the matrix of nodal positions in 3-D $x_i^b$ can also be reordered as a vector $x_{3b+i-1}$, and similarly the fourth order tensor $G_{ik}^{bn}$ can be reorganized as a matrix $G_{3b+i-1\ 3n+k-1}$. While reducing the dimensions of the higher order tensors would be helpful if we want to apply tools of linear algebra to analyze equations containing such quantities, in this work, we will only investigate special cases with node motions restricted to only one axis, which will automatically restrict the maximum dimension of the tensors involved to 2. Thus, all derivations will be done using the top and bottom index notation described above which, we believe, is more concise and easier to follow. When an equation is shown in matrix notation, we use bold lower case font to denote vectors, bold uppercase font for matrices, and script letters for higher order tensors.

Additionally, Cauchy stresses are denoted by $S_{ij}$, or $\mathbf{S}$, and $\sigma$ is used to refer to the force in a network fiber. We consider only networks of highly flexible fibers, i.e., the contour length of the fibers is much greater than its persistence length. Thus, no strain energy is stored in bending the fibers, and only axial deformations generate a resisting force within the fiber.

### 2.2.1 Theoretical analysis of network relaxation

#### Calculation of average network stress

Consider a representative volume element (RVE) containing a network with $N$ nodes, i.e., points where fibers intersect either with each other, or with the RVE boundary. Let $N = N_b + N_i$, where $N_b$ and $N_i$ are boundary and internal nodes, repectively. Under an imposed deformation, the average Cauchy stress in the network $\langle S_{ij} \rangle$ can be calculated from the forces on the boundary nodes using a volume averaging method

described in [Chandran and Barocas, 2005] and briefly shown below.

$$\begin{aligned}
\langle S_{ij} \rangle &= \frac{1}{V} \int S_{ij} dV \\
\langle S_{ij} \rangle &= \frac{1}{V} \int S_{ik} \delta_{jk} dV \\
\langle S_{ij} \rangle &= \frac{1}{V} \int S_{ik} x_{j,k} dV \\
\langle S_{ij} \rangle &= \frac{1}{V} \int (x_j S_{ik})_{,k} dV - \frac{1}{V} \int x_j S_{ik,k} dV
\end{aligned}$$

where $V$ is the volume of the box enclosing the deformed network. Applying the divergence theorem to the first term and using the fact that the second term is zero by the requirement of local equilibrium, $S_{ik,k} = 0$, we write

$$\langle S_{ij} \rangle = \frac{1}{V} \oint n_k x_j S_{ik} ds.$$

The traction on the boundary $n_k S_{ik}$, however, is entirely provided by the fiber forces acting on boundary nodes. Thus, assuming that the fiber diameter is very small compared to the RVE dimension, we obtain

$$\langle S_{ij} \rangle = \frac{1}{V} \oint x_j f_i ds = \frac{1}{V} f_i^b x_j^b \tag{2.1}$$

where $x_j^b$ is the coordinate along the $j$ direction, $f_i^b$ is the force in the $i$ direction, acting on the boundary node $b$, and summation occurs over all boundary nodes, i.e., $1 \leq b \leq N_b$. In matrix form, Equation 4.4 may be written as

$$\langle \mathbf{S} \rangle = \frac{1}{V} \mathbf{X}_B^T \mathbf{F}_B = \frac{1}{V} \begin{bmatrix} x_1^1 & x_2^1 & x_3^1 \\ x_1^2 & x_2^2 & x_1^2 \\ \vdots & \vdots & \vdots \\ x_1^{N_b} & x_2^{N_b} & x_3^{N_b} \end{bmatrix}^T \begin{bmatrix} f_1^1 & f_2^1 & f_3^1 \\ f_1^2 & f_2^2 & f_3^2 \\ \vdots & \vdots & \vdots \\ f_1^{N_b} & f_2^{N_b} & f_3^{N_b} \end{bmatrix}. \tag{2.2}$$

where $\mathbf{X}_B$ is the matrix of boundary node positions, and $\mathbf{F}_B$ is the matrix of boundary node forces, with rows indicating node number, and columns denoting direction.

### Network relaxation

For the following section, it is assumed that the network is stretched and held such that the nodes lying on the network boundary do not move, but that the internal nodes are free to reorganize as the network relaxes. Differentiating Equation 4.4 with respect to time and recognizing that the volume of the network domain does not change during relaxation

$$\frac{\mathrm{d}\langle S_{ij}\rangle}{\mathrm{d}t} = \frac{1}{V}\left(\frac{\mathrm{d}x_j^b}{\mathrm{d}t}f_i^b + x_j^b\frac{\mathrm{d}f_i^b}{\mathrm{d}t}\right) \text{ , and } \frac{\mathrm{d}x_j^b}{\mathrm{d}t} = 0$$

$$\therefore \frac{\mathrm{d}\langle S_{ij}\rangle}{\mathrm{d}t} = \frac{1}{V}x_j^b\frac{\mathrm{d}f_i^b}{\mathrm{d}t} \tag{2.3}$$

Since the network boundaries are held fixed in a stress relaxation experiment, the force on boundary nodes $f_i^b$ depends only on the positions of the internal nodes, i.e., $f_i^b = f_i^b(t, x_j^n)$, where $1 \leq n \leq N_i$, and $i, j = 1, 2, 3$. Thus, the derivative on the RHS of Equation 2.3 can be written as

$$\frac{\mathrm{d}f_i^b}{\mathrm{d}t} = \left.\frac{\partial f_i^b}{\partial t}\right|_x + \left.\frac{\partial f_i^b}{\partial x_k^n}\right|_t \frac{\mathrm{d}x_k^n}{\mathrm{d}t} \tag{2.4}$$

Now consider a differential change in the force on an internal node $m$ of the network

$$\mathrm{d}f_p^m = \left.\frac{\partial f_p^m}{\partial x_k^n}\right|_t \mathrm{d}x_k^n + \left.\frac{\partial f_p^m}{\partial t}\right|_x \mathrm{d}t \tag{2.5}$$

The requirement of equilibrium of the internal nodes requires that $\mathrm{d}f_p^m = 0$.

$$\therefore \frac{\mathrm{d}x_k^n}{\mathrm{d}t} = -\left(\frac{\partial f_p^m}{\partial x_k^n}\right)^{-1}\frac{\partial f_p^m}{\partial t} \tag{2.6}$$

From Equations 2.6 and 2.4,

$$\frac{\mathrm{d}f_i^b}{\mathrm{d}t} = \left.\frac{\partial f_i^b}{\partial t}\right|_x - \left(\frac{\partial f_i^b}{\partial x_k^n}\right)\left(\frac{\partial f_p^m}{\partial x_k^n}\right)^{-1}\left.\frac{\partial f_p^m}{\partial t}\right|_x \tag{2.7}$$

Let $G_{ik}^{bn} = \left.\dfrac{\partial f_i^b}{\partial x_k^n}\right|_t$ be the Jacobian matrix relating internal node motion to boundary forces, and $J_{pk}^{mn} = \left.\dfrac{\partial f_p^m}{\partial x_k^n}\right|_t$ be the Jacobian matrix for the internal nodal forces. Then Equation 2.7 becomes

$$\frac{\mathrm{d}f_i^b}{\mathrm{d}t} = \left.\frac{\partial f_i^b}{\partial t}\right|_x - G_{ik}^{bn}\left(J_{pk}^{mn}\right)^{-1}\left.\frac{\partial f_p^m}{\partial t}\right|_x, \tag{2.8}$$

and Equation 2.3,

$$\frac{\mathrm{d}\langle S_{ij}\rangle}{\mathrm{d}t} = \underbrace{\frac{1}{V}x_j^b\left.\frac{\partial f_i^b}{\partial t}\right|_x}_{\text{Material}} - \underbrace{\frac{1}{V}x_j^b G_{ik}^{bn}\left(J_{pk}^{mn}\right)^{-1}\left.\frac{\partial f_p^m}{\partial t}\right|_x}_{\text{Kinematic}}. \tag{2.9}$$

The first term on the RHS of Equation 2.9 arises due to the relaxation of the fibers connected to the boundary nodes, and it can be viewed as the *material* contribution to the network relaxation as its rate of change depends solely on the material, i.e., the constitutive equation, of the fibers. The second term arises from the reorganization of the internal nodes occurring within the network as its fibers relax, and thus, represents the *kinematic* part of the relaxation which depends on the structure of the network. The product $\mathcal{G}\mathcal{J}^{-1}$ works as a transformation matrix relating the changes in internal nodal forces to the resultant changes in boundary forces.

The force balance at every network node at each time step introduces additional algebraic constraints that relate nodal forces to forces in the network fibers. Thus, we can write $f_i^b = C_i^{br}\sigma^r$, and $f_p^m = C_p^{mr}\sigma^r$ for boundary and internal nodes, respectively,

where $\sigma^r$ is the force in fiber $r$. Equation 2.9 then becomes

$$\frac{\mathrm{d}\langle S_{ij}\rangle}{\mathrm{d}t} = \frac{1}{V} x_j^b \left( \frac{\partial \left( C_r^{br} \sigma^r \right)}{\partial t}\bigg|_x - G_{ik}^{bn} \left( J_{pk}^{mn} \right)^{-1} \frac{\partial \left( C_p^{mr} \sigma^r \right)}{\partial t}\bigg|_x \right), \tag{2.10}$$

or, in matrix notation

$$\frac{\mathrm{d}\langle \mathbf{S} \rangle}{\mathrm{d}t} = \frac{1}{V} \left( \mathbf{X}_B \right)^T \left( \frac{\partial \mathcal{C}_\mathbf{B} \boldsymbol{\sigma}}{\partial t}\bigg|_x - \mathcal{G}\mathcal{J}^{-1} \frac{\partial \mathcal{C}_\mathbf{I} \boldsymbol{\sigma}}{\partial t}\bigg|_x \right). \tag{2.11}$$

where $\boldsymbol{\sigma}$ is the vector of fiber forces, and $\mathcal{C}_\mathbf{B}$, and $\mathcal{C}_\mathbf{I}$ are tensors relating fiber forces to forces on boundary and internal nodes, respectively.

### 2.2.2 Network modeling

Stress relaxation of networks was simulated by representing networks as trusses composed of viscoelastic cylindrical members (fibers) connected by means of pin-joints (nodes) allowing free rotation.

#### Single fiber mechanics

Individual fibers within a network were modeled as one-dimensional viscoelastic elements following the Maxwell constitutive law (Figure 2.1(a))

$$\frac{\dot{\sigma}}{E} + \frac{\sigma}{\eta} = \dot{\lambda}, \tag{2.12}$$

where $\sigma$ is the force generated in the fiber, $E$ is the stiffness of the linear spring element, $\eta$ is the viscosity of the dashpot element, $\lambda$ is the fiber stretch, and a dot over the symbol indicates a derivative with respect to time. When a fiber is stretched and held,

$$\dot{\sigma} = -\frac{E}{\eta}\sigma = -\frac{1}{\tau}\sigma, \tag{2.13}$$

where the ratio $\tau = \frac{\eta}{E}$ is the characteristic time over which the force in the fiber decays and approaches a steady state value of zero.

### Network mechanics

Networks formed by connecting Maxwell fibers at nodes were stretched uniaxially by imposing a displacement on all nodes lying on one face of the network while keeping the opposite face fixed in space. The surfaces facing in the other two coordinate directions were displaced such that the total volume of the box containing the network remained constant. Network nodes were identified as either boundary nodes, which included all nodes lying on a network face and constrained to move with the network face, or internal nodes, which were free to move and equilibrate. Fiber stretching due to the motion of the network boundary generated forces on all network nodes, boundary as well as internal. At every time step, however, the equilibrium solution of the network force problem had no net force on any internal node. The nodal positions corresponding to this equilibrium solution were calculated using Newton's method by computing the Jacobian matrix J such that $J_{ij} = \frac{\partial f_i}{\partial x_j}$, where $f$ is total force on a node, and $x$ is its position. We used backward-Euler integration for the time dependent terms in the fiber constitutive equations. Newton iteration was applied at every time step until the net force on all internal nodes was less than a specified tolerance. The volume-averaged Cauchy stress in the network was then calculated using Equation 4.4. All computations were carried out through scripts written in MATLAB [MATLAB, 2013].

### Network stress relaxation

Network relaxation was simulated by stretching the network uniaxially in the X direction in the first time step, and subsequently holding the network in the deformed configuration to obtain the evolution of network stress with time. At every time step,

an instantaneous relaxation time was calculated as

$$\tau_{inst} = -\langle S_{11} \rangle \left( \frac{\mathrm{d} \langle S_{11} \rangle}{\mathrm{d}t} \right)^{-1}. \tag{2.14}$$

Additionally, a relaxation spectrum was computed for the network by fitting the stress-time curve to a Prony series (or a Generalized Maxwell model, Figure 2.1(b)) using a discrete spectral fitting algorithm developed by Babaei et al. [Babaei et al., 2015]. Briefly, using a non-negative least squares regression method, the algorithm computed values for $E_n$ corresponding to an interval of time constants $\tau_n = \frac{E_n}{\eta_n}$ selected *a priori*, and spaced equidistantly on a logarithmic scale. For our network relaxation data, the chosen interval of the time constants was discretized into 1000 parts, i.e., the data was fit to a Prony series with 1000 Maxwell branches; the range of the time constant interval was selected such that its lower bound was at least a decade lower than the characteristic relaxation time of the fastest fiber in the network, and similarly, the upper bound was a decade larger than the slowest fiber relaxation time in the network.

### 2.2.3 Case studies

First, we applied the theoretical and modeling approaches described above to a simplified end-to-end chain of fibers. We used the simplified case to compare the theoretical prediction and the model, and to better understand the kinematic contribution to network relaxation. We then simulated stress relaxation of 3-D Delaunay networks, and used the 3-D networks to study the effect of network composition on its effective relaxation behavior.

### A three-fiber four-node 1-D arrangement (3F-4N)

We used the simple arrangement of fibers shown in Figure 2.2 to confirm a match between the relaxation behavior predicted by Equation 2.10 and that obtained from the network model. Restricting the nodal motions to 1-D removes any non-linearities arising from fiber rotation, i.e., $\mathcal{C}_{\mathbf{B}}$, and $\mathcal{C}_{\mathbf{I}}$ are constant over time as the network reorganizes, which makes it easy to calculate a predicted time constant from Equation 2.10.

### 3-D networks

We next used the network model to obtain relaxation spectra for 3-D networks comprising of fibers with two different characteristic relaxation times, and we compared our results to the spectrum obtained experimentally for reconstituted collagen gels by Pryse et al. [Pryse et al., 2003]. Briefly, Pryse et al. strained collagen gel specimens to a strain of 2% in under 20 ms using a specially designed loading apparatus. The stretched gels were then held isometrically while force was recorded for 30 minutes at a sampling frequency of 5 Hz. The experimental data were subsequently fit to a Prony series with three Maxwell branches, which Pryse et al. identified as the optimal number of branches they needed to obtain a good fit to their data. We also compared our simulated viscoelastic spectra to that reported by Babaei et al. [Babaei et al., 2015] for the same collagen gel data. Babaei et al. used their discrete spectral fitting algorithm, described briefly above, to reanalyze the data of Pryse et al.

**Network generation** We generated networks using a Delaunay [Delaunay, 1934] tessellation wherein connections were formed between randomly generated points such that the circumsphere of any tetrahedron formed by a set of four connected nodes did not contain any other network node (Figure 2.3(a)). Networks were generated using the MATLAB function *delaunay* [MATLAB, 2013]. Delaunay networks have

been used in previous studies modeling fibrous tissues [Aghvami et al., 2016].

Networks generated were isotropic and were trimmed to fit within a unit cube in the computational domain. The physical space represented by this unit volume of computation domain was calculated from the equation [Chandran and Barocas, 2005]

$$X = \sqrt{\frac{\pi r^2 l_{total}}{\phi}} \tag{2.15}$$

where $X$ is the conversion factor relating the physical and computational domains, $r$ is the fiber radius, $l_{total}$ is the total fiber length in the network in the computational domain, and $\phi$ is the fiber volume fraction. All fibers in the network had the same radius of $r = 100$ nm [Lai et al., 2012], and the number of nodes and fibers was selected such that the unit cube containing the network represented a physical domain of side $X \approx 10\mu$m. Prior to simulating stress relaxation, the network was also confirmed to be sufficiently resolved, i.e., there was no change in the elastic network stress-stretch response with a further increase in the number of nodes and fibers.

**Network relaxation spectra and comparison with reconstituted collagen** The fibers in the network were divided into two types: fast relaxers and slow relaxers (Figure 2.3(a)). The characteristic relaxation time of the fast relaxers was less than that of the slow ones, i.e., $\tau_{fast} < \tau_{slow}$. Values for the characteristic times were selected to match the fastest and slowest relaxation times identified by Pryse et al. for reconstituted collagen gels with $\tau_{fast} = 4.73$ seconds, and $\tau_{slow} = 775.35$ seconds.

Next, we simulated stress relaxation of the network for different compositions of the two types of fibers. Starting with a network composed of all fast relaxing fibers, we increased the composition of the slow relaxers by changing 2% of the fibers at a time. Fibers to be changed to slow relaxers in each step were selected at random. This process of simulating stress relaxation of the network at different compositions was repeated for 5 networks. The relaxation protocol simulated was similar to that

used by Pryse et al., where the network was stretched by 2% in 20 ms and held.

The stress-time curves obtained from the simulated relaxation of each of the different compositions of the networks were compared to the relaxation data of Pryse et al. to find the composition that best matched the experimental data and the simulated curves. Since we used Maxwell fibers in our model, the network stress always dropped to zero over time, in contrast to the experimental data, for which the gels exhibited a non-zero steady state stress. Thus, to compare the experimental and simulated stress-time curves, we subtracted the steady state stress from the data of Pryse et al., and normalized both datasets to the peak stress, i.e., the stress at 2% stretch. Mean squared error (MSE) was used as the measure of goodness of fit between the experimental data and simulated curves.

**Fiber percolation** As the composition of the slow relaxers was gradually increased, we also probed the network for percolating slowly-relaxing paths, i.e., continuous paths of only slow fibers connecting the two loaded faces of the network (Figure 2.3(b)). Fiber percolation was evaluated by calculating the shortest path between all pairs of nodes lying on the two opposite faces using a Floyd-Warshall algorithm [Floyd, 1962]. Paths of only slow fibers were identified by appropriately modifying the adjacency matrix $A$ of the network such that for every pair of nodes in the network

$$A^{i,j} = \begin{cases} 1 & \text{if node i is connected to node j by a slow fiber} \\ 0 & \text{otherwise} \end{cases}$$

## 2.3 Results and Discussion

### 2.3.1 3F-4N network relaxation

#### Theoretical prediction of relaxation behavior

For the node and fiber numbering as shown in Figure 2.2, nodes 1 and 4 are boundary nodes, while nodes 2 and 3 are interior. A linear arrangement such as this provides two benefits, Firstly, since the nodes are restricted to move along a line, the dimensions of the quantities involved in Equation 2.10 reduce. For instance, $f_i^b = f_1^b = \mathbf{f_B} = [f_1^1 \ f_1^4]$, and

$$G_{ij}^{bn} = G_{11}^{bn} = \frac{\partial f_i^b}{\partial x_j^n}, \text{ or } \mathbf{G} = \begin{bmatrix} \frac{\partial f_1^1}{\partial x_1^2} & \frac{\partial f_1^1}{\partial x_1^3} \\ \frac{\partial f_1^4}{\partial x_1^2} & \frac{\partial f_1^4}{\partial x_1^3} \end{bmatrix}.$$

Similarly,

$$J_{ij}^{mn} = J_{11}^{mn} = \frac{\partial f_i^m}{\partial x_j^n}, \text{ or } \mathbf{J} = \begin{bmatrix} \frac{\partial f_1^2}{\partial x_1^2} & \frac{\partial f_1^2}{\partial x_1^3} \\ \frac{\partial f_1^4}{\partial x_1^3} & \frac{\partial f_1^3}{\partial x_1^3} \end{bmatrix}.$$

Another benefit of the linear arrangement is that the forces in all the fibers are equal since there can be no net force on the internal nodes at equilibrium. Also, the magnitude of the boundary node forces are equal to the fiber forces, and they point in opposite directions, i.e., $|f_1^1| = |f_1^4| = \sigma$, and $f_1^1 = -f_1^4$. From Equation 4.4 then,

$$\langle S_{11} \rangle = \frac{1}{V} \sigma \left( x_1^1 - x_1^4 \right).$$

The volume of the network box for this linear arrangement is, however, simply the end-to-end length of the arrangement, i.e., $V = (x_1^1 - x_1^4)$. Thus,

$$\langle S_{11} \rangle = \sigma. \tag{2.16}$$

For the 3F-4N arrangement from Figure 2.2,

$$\mathbf{G} = \begin{bmatrix} E_1 & 0 \\ 0 & E_3 \end{bmatrix}, \text{and } \mathbf{J} = \begin{bmatrix} -(E_1+E_2) & E_2 \\ E_2 & -(E_2+E_3) \end{bmatrix}.$$

and the constraint matrices relating nodal forces to fiber forces are

$$\mathbf{C_B} = \begin{bmatrix} 1 & 0 & 0 \\ 0 & 0 & -1 \end{bmatrix}, \text{and } \mathbf{C_I} = \begin{bmatrix} -1 & 1 & 0 \\ 0 & -1 & 1 \end{bmatrix}.$$

Substituting in Equation 2.11, we get

$$\frac{\mathrm{d}\langle \mathbf{S} \rangle}{\mathrm{d}t} = \frac{1}{V}\mathbf{X}_B^T \left( \begin{bmatrix} 1 & 0 & 0 \\ 0 & 0 & -1 \end{bmatrix} - \begin{bmatrix} E_1 & 0 \\ 0 & E_3 \end{bmatrix} \begin{bmatrix} -(E_1+E_2) & E_2 \\ E_2 & -(E_2+E_3) \end{bmatrix}^{-1} \begin{bmatrix} -1 & 1 & 0 \\ 0 & -1 & 1 \end{bmatrix} \right) \left. \frac{\partial \boldsymbol{\sigma}}{\partial t} \right|_x \quad (2.17)$$

where $\boldsymbol{\sigma} = [\sigma^1, \sigma^2, \sigma^3]^T = \sigma[1,1,1]^T$, and from Equation 2.13, for Maxwell fibers,

$$\left. \frac{\partial \boldsymbol{\sigma}}{\partial t} \right|_x = \mathbf{T}^{-1}\boldsymbol{\sigma} = -\sigma \begin{bmatrix} \tau_1 & 0 & 0 \\ 0 & \tau_2 & 0 \\ 0 & 0 & \tau_3 \end{bmatrix}^{-1} \begin{bmatrix} 1 \\ 1 \\ 1 \end{bmatrix}$$

Following some algebraic manipulation, and using Equation 2.16, Equation 2.17 becomes,

$$\frac{\mathrm{d}\langle S_{11} \rangle}{\mathrm{d}t} = \frac{1}{V}\mathbf{X}_B^T \left( \frac{E_1E_2E_3}{E_1E_2 + E_2E_3 + E_1E_3} \begin{bmatrix} \frac{1}{E_1\tau_1} & \frac{1}{E_2\tau_2} & \frac{1}{E_3\tau_3} \\ \frac{-1}{E_1\tau_1} & \frac{-1}{E_2\tau_2} & \frac{-1}{E_3\tau_3} \end{bmatrix} \begin{bmatrix} 1 \\ 1 \\ 1 \end{bmatrix} \langle S_{11} \rangle \right) \quad (2.18)$$

From Equation 2.18, it is clear that the stress in the system of fibers relaxes with a constant effective relaxation time of

$$\tau_{inst} = \left(\frac{1}{E_1} + \frac{1}{E_2} + \frac{1}{E_3}\right)\left(\frac{1}{\frac{1}{E_1\tau_1} + \frac{1}{E_2\tau_2} + \frac{1}{E_3\tau_3}}\right) \tag{2.19}$$

which can be viewed as a scaled harmonic mean of the relaxation times of the individual fibers, weighted by their respective stiffness moduli. The effective relaxation time is not necessarily equal to the relaxation time of any individual fiber $\tau_1$, $\tau_2$, or $\tau_3$. If the fibers are identical, then the network relaxes at the same rate as the fibers. The above result can also be generalized to any number of fibers arranged end-to-end. For such an arrangement with $N_f$ fibers, the relaxation time of the system will be given by

$$\tau_{inst} = \sum_{i=1}^{N_f} \frac{1}{E_i}\left(\frac{1}{\sum_{i=1}^{N_f} \frac{1}{E_i\tau_i}}\right).$$

**Simulation of relaxation behavior**

Stress relaxation of the 3F-4N arrangement with various spatial combinations of fast and slow relaxation times was simulated to obtain the instantaneous relaxation time, and stress-time curves like the ones shown in Figure 2.4(a) and (b) for the case where the relaxation time of the middle fiber ($\tau_2 = 1$ s) was longer than that of the two outer ones ($\tau_1 = \tau_3 = 0.1$ s). The value of the effective relaxation time predicted by Equation 2.19 always matched that calculated from the simulations. Note that the effective relaxation time of the system is constant and does not change over time as the nodes are constrained to move on a line, and $\mathcal{C}_B$, and $\mathcal{C}_I$ are constant.

### 2.3.2 3-D Delaunay network relaxation

#### Effect of network composition on relaxation

**Instantaneous relaxation time** Figure 2.5(a) shows plots of the evolution of the instantaneous relaxation times of a network for different compositions. The two dashed lines show the effective relaxation time of the network when all fibers have the same relaxation time, i.e., $\tau_{fiber} = \tau_{slow} = 775.35$, or $\tau_{fiber} = \tau_{fast} = 4.73$ seconds. As expected, if all the fibers relax at the same rate, the forces on internal nodes are always balanced, reducing the kinematic contribution to zero. The solid lines in Figure 2.5(a) show the instantaneous relaxation time for the same network at different intermediate compositions of slow and fast relaxers – ratios of 70-30, 50-50, and 30-70% slow and fast relaxers, respectively – with the arrow indicating the direction of increasing fast relaxer composition. In these cases, the instantaneous relaxation times for the 3-D network vary over time as the constraint tensors $\mathcal{C}_{\mathbf{B}}$ and $\mathcal{C}_{\mathbf{I}}$ evolve with the equilibration of forces on internal nodes. The instantaneous relaxation time of the network immediately following the stretch lies between $\tau_{fast}$ and $\tau_{slow}$, but at long times, the contribution of the fast relaxing fibers to the overall network behavior drops significantly, and the instantaneous behavior of the network is dominated by the slow relaxers. Figure 2.5(b) shows the normalized stress-time curve for the network at the three compositions mentioned above, again, with the arrow pointing in the direction of increasing composition of rapidly-relaxing fibers.

The variation of the instantaneous relaxation time right after the stretch, and as the system approaches steady-state, with change in network composition is shown in Figure 2.6. As the percentage of slowly-relaxing fibers in the networks increases, the initial effective relaxation time (dots) increases slowly. The near-steady-state relaxation time (triangles), however, increases rapidly and approaches that of the slow relaxers in the network. Since the fast relaxers decay out more quickly over time,

the instantaneous relaxation time is always greater near steady-state than during the initial relaxation. The effect of fiber percolation can also be seen in Figure 2.6. The dashed vertical line on the left shows the network composition for which slow fiber percolation was first detected, while the dashed vertical line on the right indicates the network composition at which the fast relaxing fibers stop percolating. Before the slow relaxers percolate, the steady-state network relaxation time does not reach the slow rate. Once a percolating path of slow relaxers has formed, however, the steady-state relaxation behavior of the network is governed by the slow relaxers. Žagar et al. [Žagar et al., 2015] have shown a similar effect of fiber percolation on the non-linear strain-stiffening trend observed in biopolymer networks.

**Relaxation spectra** Evolution of the relaxation spectrum with changing network composition can be viewed in the series of snapshots shown in Figure 2.7. At the two extreme cases, when the network is made up of only one type of fiber, the spectrum shows a solitary peak. As the network composition changes, however, we see evolution of the spectral landscape with multiple peaks arising, shifting, and disappearing. For instance, for the case of the network composed of an equal number of slow and fast relaxers (Figure 2.7(c)), the spectrum shows four distinct peaks. The two extreme peaks at 4.9 s, and 722.5 s are close to the relaxation times of the two fiber types. The intermediate peaks at 10.6 s, and 64.2 s, different from the characteristic times of the two fiber types, arise due to the contribution of the kinematic term.

### The relaxation spectrum of reconstituted collagen gels

Since all five network architectures tested showed similar relaxation trends, for the next part, we picked one network at random. The relaxation response of that network when it was composed of 43.7% slow relaxers was identified as being the best fit to the experimental stress relaxation data based on the mean squared error (Figure

2.8(a)). The relaxation spectrum of the network with this composition is shown in Figure 2.8(b) along with the three time constants calculated by Pryse et al. for collagen gels. The intermediate structure-dependent time constants in the simulated spectrum were on the same order of magnitude as the middle time constant identified by Pryse et al.

The simulated relaxation spectrum is also consistent with the findings of Babaei et al. (Figure 2.9). Falling roughly within the interval of time constants defined by our fast and slow relaxers, they identified four peaks at 2.6 s, 16.1 s, 72.7 s, and 1520 s. They also found two additional time constants that were less than the characteristic time we used for our fast relaxers, and thus were not seen in our simulations.

We did not aim to describe accurately the viscoelastic relaxation of reconstituted collagen gels with our model. Neither was it our goal to explore the source of viscoelasticity in individual fibers via an analysis of overall network behavior, e.g., as done by Gardel et al. [Gardel et al., 2004b] to study single F-actin filament mechanics. Rather, our goal was to investigate how structure-based effects of interactions between multiple viscoelastic elements manifest in the relaxation spectrum of a network. Similar to the theory developed by Storm et al. [Storm et al., 2005] exploring the in-built strain-stiffening effect of crosslinked networks, we show that a system of interconnected viscoelastic fibers can exhibit certain relaxation time scales that are inherently related to their network structure. The similarity between the experimental and simulated spectra seen above suggests that the viscoelastic response of collagen is at least in part influenced by its network structure, and that some of the time constants identified by Babaei et al. possibly arise as a result of the reorganization of fibers within the network.

The non-affine reorganization of internal nodes is by no means the sole mechanism behind the broad relaxation spectrum of biopolymer gels. Certainly, other factors also contribute to the overall relaxation behavior, e.g., Broedersz et al. [Broedersz

et al., 2010a] showed the presence of multiple relaxation times arising out of crosslink binding and unbinding within the gel. The model presented here assumed that the only source of viscoelasticity was the deformation of fibers and not, e.g., fiber motion through the embedding material, fiber sliding through physical crosslinks, or bond breaking and remodeling. Furthermore, there could be a range of individual fiber relaxation times within a gel, and the distinction between those characteristic times likely is not as clear-cut as assumed in our model. While we consider this a suitable first approximation, further research will need to address the effects of these factors on the relaxation behavior of networks.

# Nomenclature

| | |
|---|---|
| superscript index | node/fiber number |
| subscript index | direction |
| $N_b$ | number of nodes on network boundary |
| $N_i$ | number of internal nodes |
| $N_f$ | number of fibers in the network |
| $f_i^b$ | force on node $b$ along direction $i$ |
| $x_i^b$ | position of node $b$ along direction $i$ |
| $V$ | volume of network domain |
| $S_{ij}$ | Cauchy stress |
| $G_{ij}^{bn}$ | Jacobian matrix relating motion of internal node $n$ to force on boundary node $b$ |
| $J_{ij}^{mn}$ | Jacobain matrix relating motion of internal node $n$ to force on internal node $m$ |
| $\sigma^f$ | force generated in network fiber $f$ |
| $C_i^{bf}$ | component of force in fiber $f$ along direction $i$ acting on node $b$ |
| $E$ | stiffness of linear elastic element |
| $\eta$ | viscosity of dashpot element |
| $\tau$ | characteristic relaxation time |

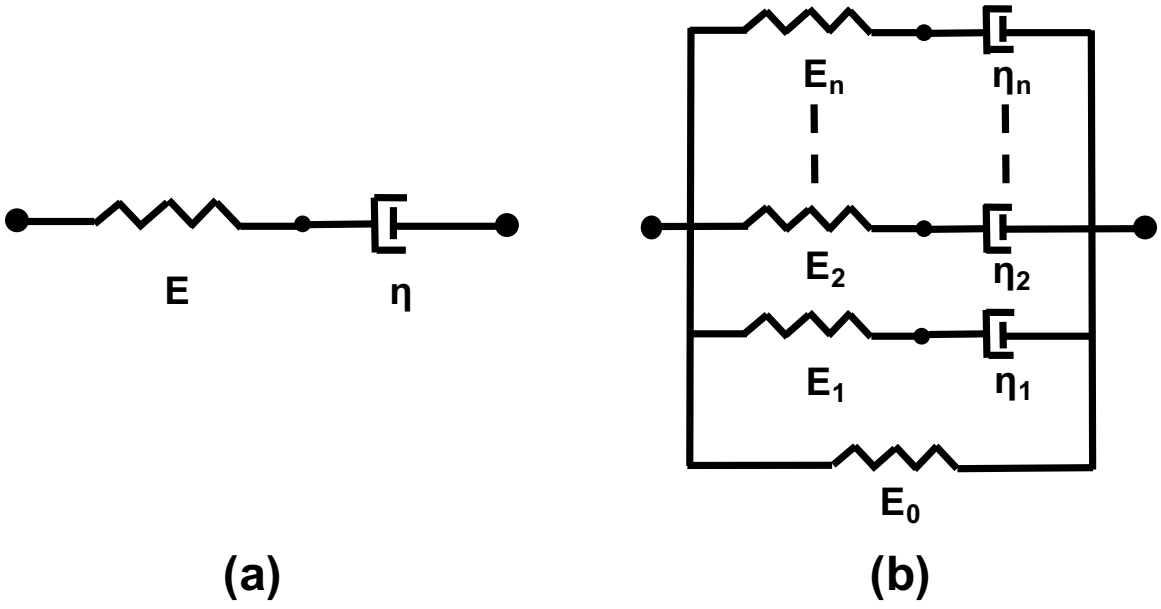


Figure 2.1: (a) A spring and dashpot model of the Maxwell fluid, (b) A Prony series with multiple branches of Maxwell elements in parallel with an elastic spring element.

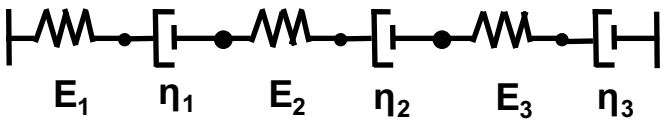


Figure 2.2: Simplified arrangement of three Maxwell fibers connected end-to-end.

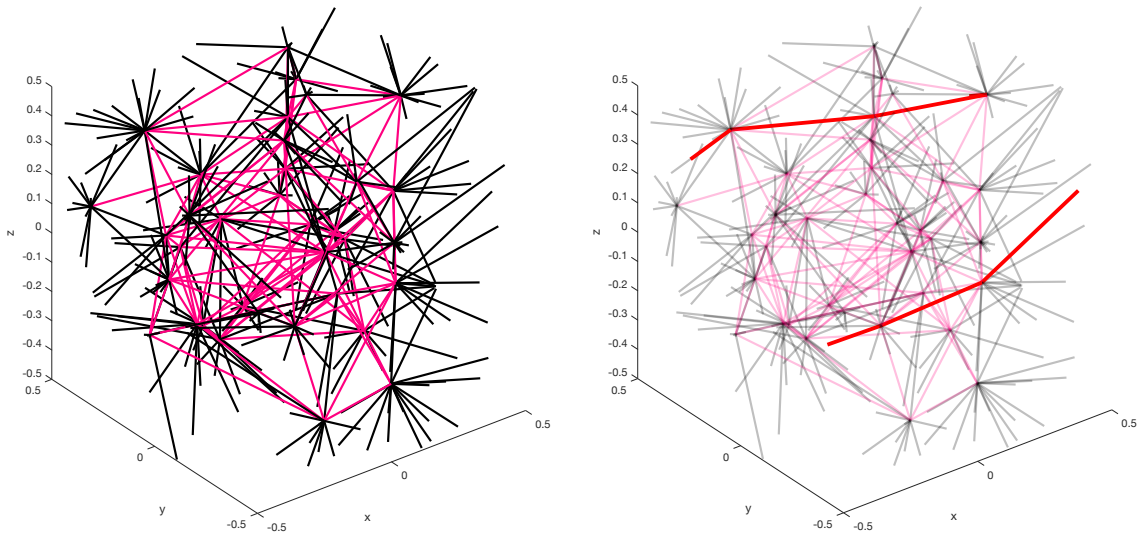


Figure 2.3: (a) A Delaunay network composed of fibers with two distinct relaxation times, $\tau_{slow}$ (pink), and $\tau_{fast}$ (black), (b) Similar network, but with two percolating connections of slow relaxers (shown in red).

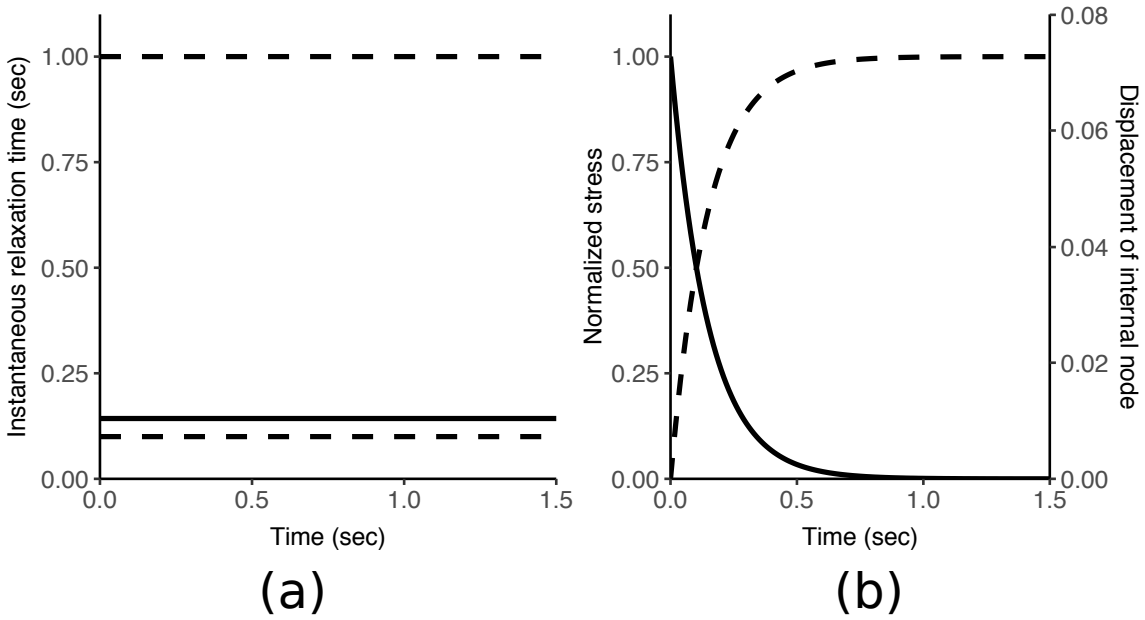


Figure 2.4: (a) Instantaneous relaxation time versus time for the simulated end-to-end arrangement of three Maxwell fibers of equal stiffness (i.e., $E_1 = E_2 = E_3$). The characteristic relaxation times of the two outer fibers was 0.1 s (lower dashed line), and that of the middle fiber was 1 s (upper dashed line). The effective relaxation time of the arrangement was 0.143 s (solid line) – different from that of any individual fiber. (b) The normalized stress in the fibers as a function of time (solid line - left Y axis), and the displacement (in the computational domain) of an internal node as the fiber stresses relax over time (dashed line - right Y axis).

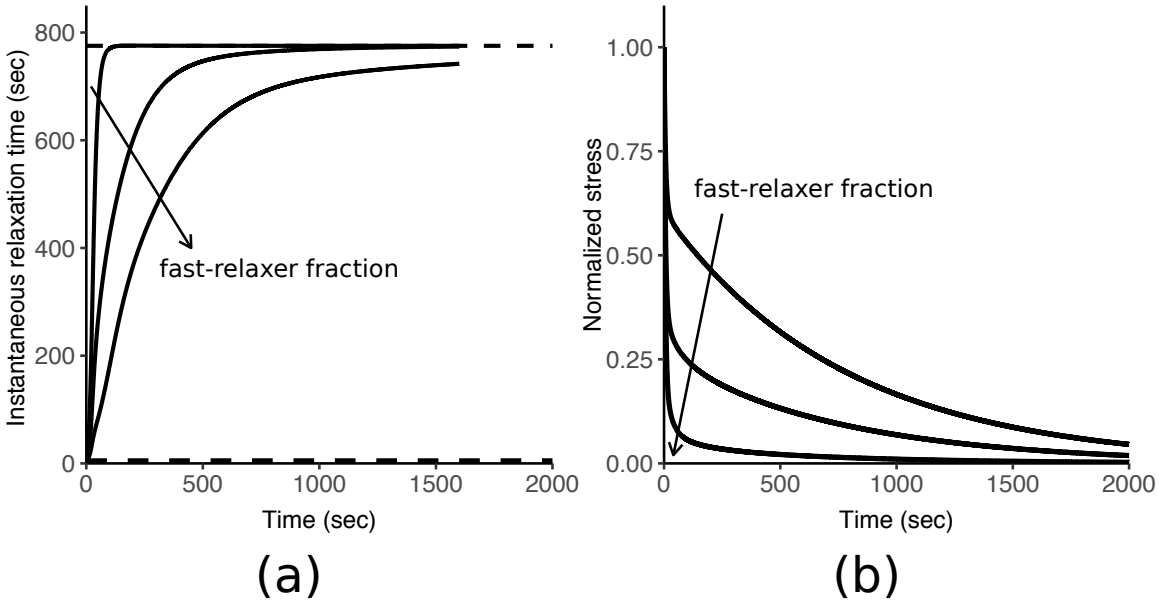


Figure 2.5: (a) Instantaneous relaxation times for a network with different compositions of slow and fast relaxers. The instantaneous relaxation time for a network comprising of 70-30, 50-50, and 30-70% slow and fast relaxers, respectively, (solid lines) varies over time within the interval bounded by the instantaneous relaxation times for the network with all fast relaxers (lower dashed line), and all slow relaxers (upper dashed line). The arrow indicates the direction of increasing percentage of fast relaxing fibers within the network. (b) Stress in the network over time for the three intermediate compositions shown in (a).

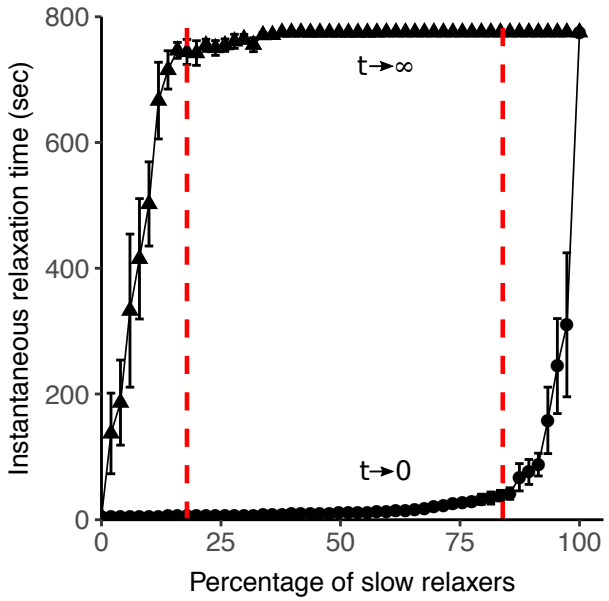


Figure 2.6: Change in the instantaneous relaxation time of the network immediately following the stretch (dots), and near steady-state (triangles) for different compositions of the networks (n = 5, error bars represent standard error of the mean). Note how the initial relaxation time increases gradually as the percentage of slow relaxers in the network rises. The steady-state time, however, rapidly approaches that of the slow relaxers. The left vertical dashed line indicates the average network composition at which slow relaxers percolate, while the right vertical line marks the average composition at which fast relaxers stop percolating within the network.

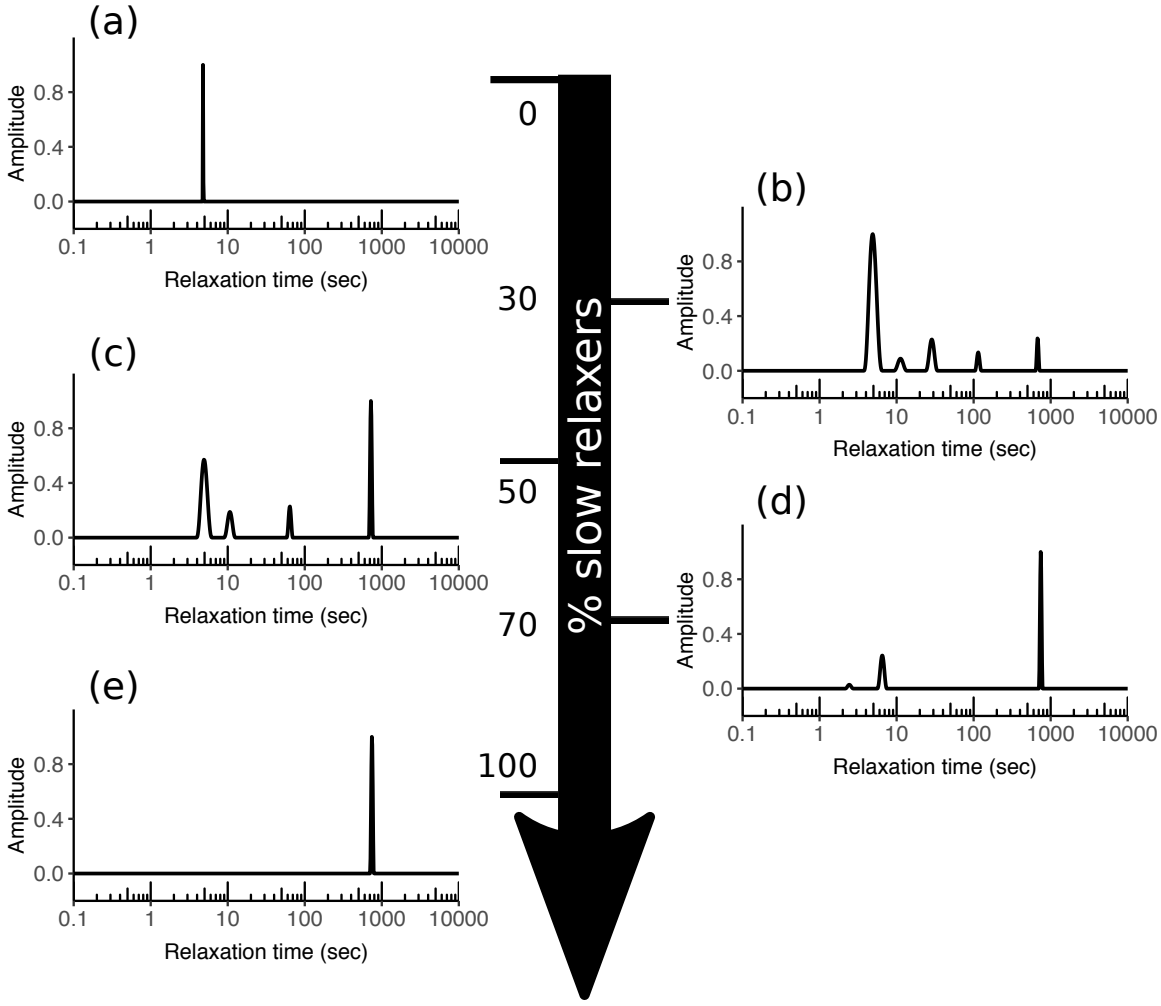


Figure 2.7: Relaxation spectra for a network as its composition changes from all fast relaxers (a) to all slow relaxers (e). The intermediate compositions (b,c, and d) shown are 30-70, 50-50, and 70-30 % slow and fast relaxers, respectively.

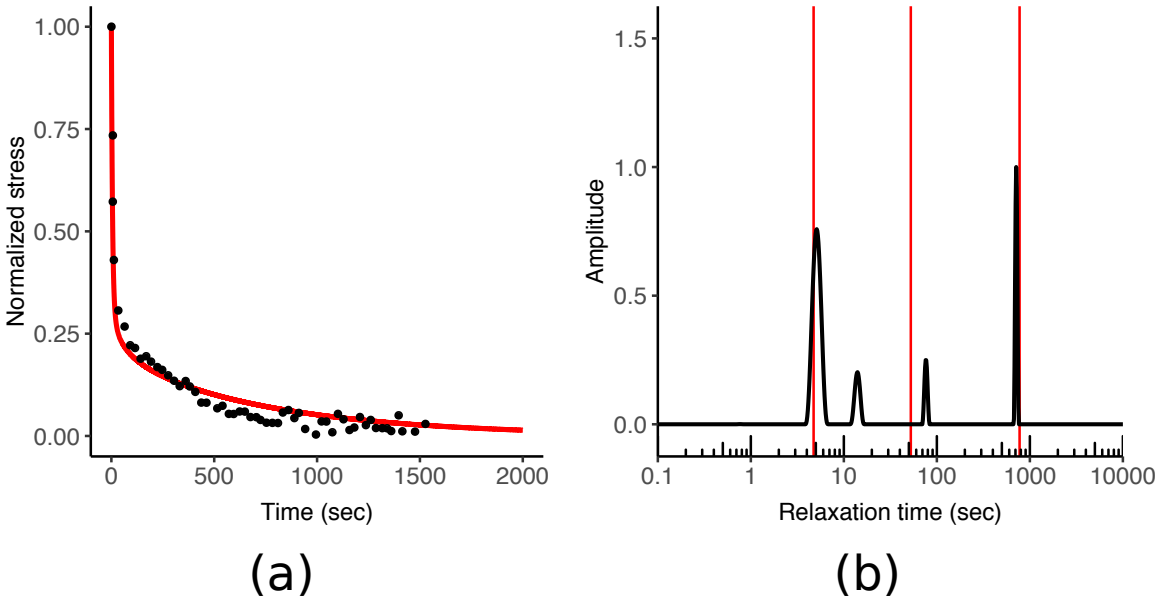


Figure 2.8: Comparison of the simulated relaxation spectrum to that of reconstituted collagen gels. (a) A network composed of 43.7 % slow relaxers best matched the experimental data of Pryse et al. [Pryse et al., 2003](MSE = 0.0019). (b) Relaxation spectrum of the simulated network showing peaks at 5.1 s, 14 s, 75.8 s, and 712.6 s. Red lines mark the relaxation times computed by Pryse et al.

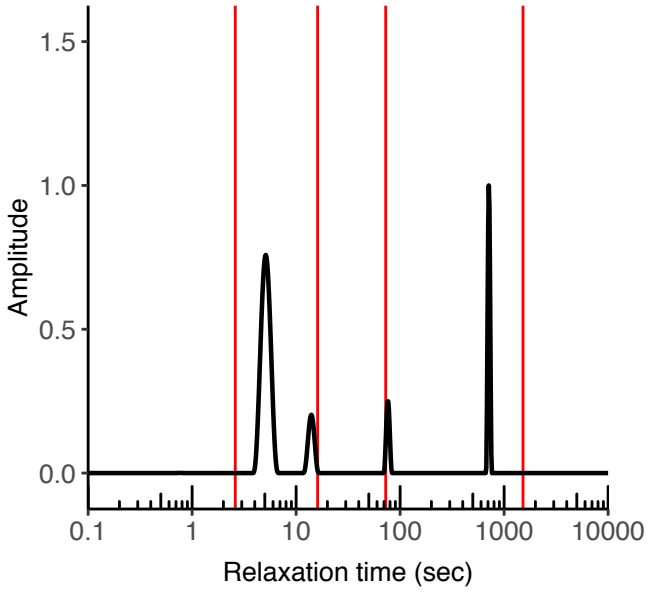


Figure 2.9: Comparison of the simulated relaxation spectrum to that computed by Babaei et al. [Babaei et al., 2015] for the collagen gel relaxation data of Pryse et al. [Pryse et al., 2003]. Red lines mark the relaxation times computed by Babaei et al. near the interval bound by the slow and fast characteristic relaxation times of the fibers used in the simulation.

# Chapter 3

# Multiscale Model of Fatigue of Collagen Gels

The content of this chapter was published as a research article in *Biomechanics and Modeling in Mechanobiology* by Dhume, Shih, and Barocas [Dhume et al., 2018].

## 3.1 Background

Structures composed of fiber networks are extremely prevalent in our world. A number of consumer products, such as paper and open-cell foams, are composed of networks of polymeric elements with diameters on the order of micrometers. Networks composed of interconnected filaments or fibers are also a common occurrence in biology. These networks can form hierarchical structures ranging in size from a few micrometers, e.g., the actin filament network of the cytoskeleton [Mitchison and Cramer, 1996], to larger-scale structures on the order of millimeters, e.g., connective tissues such as the facet capsular ligament [Ban et al., 2017], or the fibrin network in a clot [Weisel and Nagaswami, 1992]. Biopolymeric materials, such as collagen gels, are hydrated fibrous networks [Flory, 1953]. Electrospun materials, such as the scaffolds used in tissue engineering to mimic the mechanical properties of the native tissue, are

networks composed of nano/microscale fibers [Barnes et al., 2007].

The literature on the mechanics of networks is vast, with a tremendous amount of work being done in particular on flexible macromolecular networks such as rubber. A major objective of such macromolecular materials science has been to derive constitutive equations governing the macroscale mechanics of the material [Flory and Rehner, 1943, Wang and Guth, 1952, Arruda and Boyce, 1993]. Analogous techniques have also been developed and used extensively in the study of other heterogeneous materials like metallic foams [Ashby et al., 2000]. Due to their importance in various industries, several studies have focused on characterizing the pre-failure mechanics [Deshpande and Fleck, 2000], fatigue failure [McCullough et al., 1999], and creep behavior of foams [Andrews et al., 1999].

Recent advances in multiscale modeling have further motivated this research, guiding it in the direction of relating macroscale material behavior to parameters of the underlying microscale network [Sarvestani and Picu, 2004, Ban et al., 2016, Abel et al., 2013]. For more information on the present understanding of mechanics of random networks, the reader is referred to the review by Picu [Picu, 2011]. The increasing use of synthetic materials with a fibrous microstructure in the manufacture of commercial products has also necessitated a better understanding and modeling of network failure and fatigue behavior, e.g., failure of electrospun scaffolds [Koh et al., 2013].

More recently, network modeling has been used by the biological community to describe the behavior of various soft tissues and tissue analogs, e.g., [Stylianopoulos and Barocas, 2007, Suki et al., 2005, Abhilash et al., 2014, Broedersz and MacKintosh, 2014, Zhang et al., 2013]. Network models have also been expanded to model catastrophic failure of tissues, e.g., [Suki et al., 2012, Witzenburg et al., 2016]. In spite of the advances made, fatigue failure of biological networks is still not well understood. Over the lifespan of a living being, tissues undergo many cycles of varying

loads, e.g., tendons in the body experience fluctuating tensile stress during daily activities, the tissues of the lung expand and contract with breathing, and the aorta expands with every heartbeat to accommodate the flow of blood. While damage can be repaired as biological tissues remodel over time, fatigue can still become increasingly relevant in certain tissues with age as the collagen turnover rate slows down [Freeman, 1999]. The tendency to fatigue can lead to injuries and a reduction in quality of life. For example, fatigue damage resulting from overuse can lead to tendinopathies [Andarawis-Puri and Flatow, 2011], fatigue failure is one of the major modes of failure of bioprosthetic heart valves [Martin and Sun, 2014], and some forms of osteoarthrosis have been attributed to the fatigue of the collagen fiber network in articular cartilage [Weightman et al., 1978].

Obviously, the fatigue behavior of a fibrous network must depend on the properties of the individual fibers that constitute it. Given, however, that a network material's pre-failure stress-strain behavior and tensile strength in a stretch-to-failure experiment depend on both the fiber properties and the network architecture [Shasavari and Picu, 2012, Picu, 2011], one must ask whether the fatigue process is similarly affected. That is, *if two networks are constructed of the same fibers but with different fiber connectivity, will the macroscopic fatigue behavior of the two networks differ, and if so, how?* We examined that question in the context of different simulated networks subjected to cyclic uniaxial loading until failure,complemented by experiments on reconstituted collagen gels.

## 3.2 Modeling Approach

### 3.2.1 Network generation

Three-dimensional fiber networks were represented as trusses composed of non-linear elastic cylindrical members (fibers) connected by means of pin-joints (nodes) allowing

free rotation. Initially, the networks were generated using a Voronoi [Voronoi, 1908] tessellation. Voronoi networks have been shown to provide a close approximation to collagen gel mechanics[Nachtrab et al., 2011] and have been used in previous studies modeling the mechanics of collagenous connective tissues [Zhang et al., 2013]. Voronoi networks have also been used to model cellular solids e.g., sponges, foams [Roberts and Garboczi, 2001, Roberts and Garboczi, 2002].

To construct Voronoi networks, three-dimensional space was divided among the initial seed points, forming polyhedral regions, such that every point inside a polyhedron was located closest to the seed point corresponding to that region and located within it. The edges of the Voronoi polyhedra calculated from the seed points represented fibers, and their vertices represented network nodes. Three-dimensional Voronoi cells were generated using the MATLAB function *voronoin* [MATLAB, 2013].

Fiber networks generated using the above algorithm were isotropic and were trimmed to fit within a unit cube in the computational domain. The physical space represented by the computational domain was related to the dimensions of the fibers and their desired volume fraction within the network by the relation

$$X = \sqrt{\frac{\pi r^2 \Sigma l}{\phi}} \tag{3.1}$$

where $X$ is the conversion factor relating the physical and computational domains, $r$ is the fiber radius, $\Sigma l$ is the total fiber length in the network within the computational domain, and $\phi$ is the fiber volume fraction. Every network had fibers of the same radius but a different length. In this work, we took $r = 100nm$ [Lai et al., 2012] and $\phi = 0.05$. The total fiber length $\Sigma l$ was typically around $150 - 200$, so the unit cube represented a physical domain of side $X \approx 10\mu m$.

### 3.2.2 Single fiber mechanics and failure

Network fibers were modeled as one-dimensional non-linear springs with the constitutive equation

$$f = \frac{EA}{B}(e^{B(\frac{\lambda^2-1}{2})} - 1) \tag{3.2}$$

where $f$ is the force generated within the fiber, $A$ is its cross-sectional area, $E$ denotes fiber stiffness, $B$ controls its non-linearity, and $\lambda$ is the fiber stretch. At infinitesimal stretch, Equation 3.2 reduces to a linear material with Young's modulus E. The constitutive equation was adapted from a previous structural model [Billiar and Sacks, 2000] and has been used in multiscale modeling of the collagen microstructure in soft tissues [Lai et al., 2012, Sander et al., 2009a]. While the non-linearity introduced by Equation 3.2 is not essential in understanding the fatigue behavior of networks, it is a more accurate model of collagenous tissue as it accounts for the lack of compression stiffness of the fibers. Similar non-linearity can also be added in the model in other ways, e.g., by assuming a linear elastic response for the fiber and introducing fiber waviness [De Vita and Slaughter, 2007], or by using bilinear fiber stiffness [Chandran and Barocas, 2006a].

Failure was introduced into the network by removing individual fibers, which was achieved in the model by reducing the small-strain modulus of a failed fiber ($E$ in Equation 3.2) by several orders of magnitude (Table 3.1). Grossly reducing the magnitude of a failed fiber ensured that it did not contribute to the mechanical response of the network, while maintaining stability of the numerical approach used to model the network. Fiber failure occurred either due to a fiber stretching beyond a critical stretch or due to fatigue. As the network was stretched by an external cyclic loading, the stress experienced by individual fibers within the network changed from cycle to cycle since the stress within a network is distributed over many fibers, and this distribution changed as fibers failed and the network structure reorganized. A stress-

life (SN) curve determined the fatigue behavior of the fibers by relating the number of cycles of repeated loading required to fail a fiber to the amplitude of the oscillating load applied to it. To account for the varying stress amplitudes experienced by a fiber, a damage fraction was calculated for each fiber, which measured the fraction of its life consumed by exposure to cycles at different stresses. Fatigue failure occurred when the value of this cumulative damage fraction exceeded 1 (Miner's rule [Miner, 1945]). A fiber's properties remained unchanged during the fatigue process until failure occurred. Additionally, it was assumed that the loading and unloading phases of the applied cyclic load on the network occurred instantaneously, so fiber fatigue failure was evaluated only at the peak of each loading cycle.

### 3.2.3 Network mechanics and failure

Repeated loading to the same averaged network stress was applied to simulate the fatigue process. Since the properties of the network changed as fibers failed, the amount of displacement required to achieve the imposed stress changed during the course of the simulation. Thus, an iterative approach was used to apply the same stress at each cycle (Figure 3.1).

Uniaxial deformation of the network was simulated by imposing a displacement on all nodes lying on one face of the network while keeping the opposite face fixed in space. The surfaces facing in the other two principal directions were assumed to be stress-free. Network nodes were identified as either boundary nodes, which included all nodes lying on a network face and constrained to move with the network face, or internal nodes, which were free to move and equilibrate. Stretching of fibers due to the motion of the network boundary generated forces on all network nodes, boundary as well as internal. For a given network boundary displacement, however, the equilibrium solution of the boundary value problem had no net force on any internal node. The nodal positions corresponding to this equilibrium solution were

calculated using Newton's method by computing the Jacobian matrix J such that

$$J_{ij} = \frac{\partial f_i}{\partial x_j} \tag{3.3}$$

where $f$ is total force on a node, $x$ is its position, and $i$ and $j$ are the unconstrained degrees of freedom of the network, i.e., every node had 3 degrees of freedom corresponding to translations in the 3 principal directions. Using the Jacobian, a displacement step was calculated for the internal nodes of the network

$$\Delta x = -J^{-1}R \tag{3.4}$$

where $\Delta x$ is the displacement step, and $R$ is the vector of residual forces on the internal nodes. This calculation was performed iteratively until the net force on all internal nodes was less than a specified tolerance. The volume-averaged Cauchy stress in the network was obtained from the forces acting on nodes lying on the network boundary[Chandran and Barocas, 2006a]:

$$\sigma_{ij}^{net} = \frac{1}{V} \sum_{bnd\ \ nodes} x_j^b f_i^b \tag{3.5}$$

where $\sigma^{net}$ is the volume-averaged Cauchy stress on the network, $x^b$ is the nodal position of a boundary node, $f^b$ is the force acting on the node, and $V$ is the volume of the network. The network deformation/equilibration cycle described above was performed iteratively using a bisection search to calculate a suitable network stretch such that the boundary forces matched the applied boundary loading. The initial stretches bounding the bisection search were selected such that the interval between the boundary force values generated by the network at these two stretches contained the external applied load. All computations were carried out through scripts written in MATLAB [MATLAB, 2013].

Failure of the network was defined as no change in the volume-averaged stress for any further increase in network stretch. By this definition, a network was determined to have reached failure once the following condition was met

$$\frac{d\sigma^{net}}{d\lambda^{net}} < \epsilon \tag{3.6}$$

where $\sigma^{net}$ and $\lambda^{net}$ are the stress and stretch of the overall network respectively, measured in the direction of deformation, and $0 < \epsilon \ll 1$. The slope $\frac{d\sigma^{net}}{d\lambda^{net}}$ was computed numerically by making a small displacement increment with no additional fatigue and recalculating the network stress. Ten Voronoi networks were subjected to a cyclic load-to-failure test to simulate fatigue and obtain an SN curve.

## 3.3 Collagen gel fatigue – experiments and model

### 3.3.1 Gel preparation and testing

Collagen gels were synthesized as described previously [Lake and Barocas, 2012]. Briefly, a 2 mg/mL collagen solution was prepared by combining the following (by volume fraction): 14.2% 1 M 4-(2-hydroxyethyl)-1-piperazineethanesulfonic acid (HEPES, ThermoFisher), 2.6% 1 M sodium hydroxide (NaOH, Sigma-Aldrich), 10% 10x Modified Eagle's Medium (MEM, ThermoFisher), 6% fetal bovine serum (FBS, GE Healthcare), 0.1% penicillin-streptom-ycin, 0.1% fungizone, 1% L-glutamine (Invitrogen), and 66% 3 mg/mL rat-tail collagen I (ThermoFisher). All ingredients were mixed on ice in a centrifuge tube and then cast into acrylic dog-bone molds sealed at the bottom with vacuum grease to prevent leaking. The collagen solution was incubated in the molds for 3 hours at 37 °C to facilitate polymerization. Polymerized gels were removed from the molds and immersed in a 1x phosphate buffered saline (PBS) bath prior to and during testing.

Uniaxial mechanical tests were performed on gels using a universal test machine with a 5N force transducer (TestResources, Shakopee, MN). First, five gels were tested in a displacement-controlled, uniaxial stretch-to-failure test to determine an average yield force for the gels, which was used to determine the load amplitudes in the subsequent fatigue tests. For stretch-to-failure tests, gels were stretched at a rate of 1 mm/min, and data were collected at 2 Hz. Next, load-controlled, uniaxial tension-tension fatigue tests were performed on collagen gels with the loading amplitudes varying cyclically between a lower limit of 10% and upper limit of 20-90% of the average yield force. For the fatigue tests, gels were stretched at a rate of 30 mm/min with a data sampling rate of 2 Hz; tests continued either until the sample failed from fatigue or until the duration of the test exceeded 30 minutes. The number of cycles at failure was recorded to obtain an SN curve.

### 3.3.2 Gel simulation

The fatigue experiments described in Section 3.3.1 were simulated using the network model wherein Voronoi networks were used to represent collagen gels. The parameters for the fiber constitutive equation (Equation 3.2) in the network model were selected based on previous research modeling the mechanics of collagen fiber networks[Witzenburg et al., 2016] (Table 3.1). The fatigue behavior of a single fiber was defined by the SN curve of a human extensor digitorum longus (EDL) tendon, obtained from the literature [Schechtman and Bader, 1997]:

$$S_{norm} = 101.25 - 14.83 \times log(N) \tag{3.7}$$

where $S_{norm}$ is the normalized load amplitude expressed as a percentage of the UTS and $N$ is the number of cycles to failure. The high degree of collagen fiber alignment in the tendon made its fatigue behavior an acceptable approximation – and the closest

| Parameter | Meaning | Value |
|---|---|---|
| $r$ | Fiber cross-section radius | 100 nm |
| $E$ | Fiber stiffness | 10 MPa |
| $B$ | Fiber non-linearity | 2.5 |
| $\lambda_{critical}$ | Failure stretch | 1.42 |
| $E_{failure}$ | Stiffness value of failed fibers | $10^{-7}$ Pa |

Table 3.1: Values for the parameters of the constitutive equation (Equation 3.2) and the failure stretch of a fiber.

one we could find – to that of a single collagen fiber.

The simulation of gel fatigue proceeded in a manner analogous to the procedure employed in testing the collagen gels. First, the simulated networks were stretched to failure to obtain an ultimate tensile strength (UTS) which was used to calculate the load amplitudes used in subsequent fatigue simulations. The cyclic loading applied to the simulated networks ensured that the networks always remained under tension. The upper load limit was equal to the external applied stress while the lower limit was 10% of the UTS.

## 3.4 Network architecture and fatigue

Having confirmed that (1) the network SN curve differs from that of an individual fiber, and (2) our network fatigue model showed a similar SN trend as that obtained from the collagen gel experiments, we investigated the effect of network geometry on its fatigue behavior. We compared the simulated SN curves obtained for three different network types with the same fiber properties.

### 3.4.1 Network generation and structure

In addition to the Voronoi networks generated previously, we also used networks created using the following two algorithms:

- **Delaunay [Delaunay, 1934]**: The initial randomly selected seed points formed the final nodes of the network. Connections were formed between those points such that the circumsphere of any tetrahedron formed by a set of four connected nodes did not contain any other network node. Networks were generated using the MATLAB function *delaunay* [MATLAB, 2013]. Delaunay networks have been used in previous studies modeling fibrous tissues [Aghvami et al., 2016].

- **Erdős-Rényi [Erdős and Rényi, 1959]**: For networks created using the Erdős-Rényi (ER) algorithm, seed points represented network nodes, and connections were formed randomly between pairs of nodes such that shorter connections were favored over longer ones. The probability distribution used to connect nodes varied inversely with the Euclidean distance between the pair of nodes and was given by

$$p(i,j)|_{i\neq j} = 1 - \frac{dist(i,j)}{max\ dist} \tag{3.8}$$

  where $p(i,j)$ is the probability of forming a connection between network nodes $i$ and $j$, $dist(i,j)$ is the Euclidean distance between nodes $i$ and $j$, and $max\ dist$ is the maximum Euclidean distance between two nodes calculated for the initial set of seed points. The average value of $max\ dist$ was 1.4 units in the computational domain. ER networks were chosen to explore the space of possible networks more thoroughly.

Networks generated using the above algorithms were also isotropic, and had the same network dimensions as the Voronoi networks detailed in Section 3.2.1. Networks were chosen to be isotropic as we wanted to eliminate any direction-dependent effects arising due to fiber anisotropy within the networks. Table 3.2 shows the average values of some measures of network topology obtained for each of the three network types – Delaunay, Voronoi, and ER.

| Network type | Total fiber length | Mean fiber length | Mean nodal degree | Number of nodes | Number of fibers | Physical dimension of network, $\mu m$ (equation 3.1) |
|---|---|---|---|---|---|---|
| Delaunay | 127.90 | 0.23 | 15 | 397 | 560 | 8.90 |
| Voronoi | 68.40 | 0.11 | 4 | 430 | 612 | 6.50 |
| Erdős-Rényi | 366.38 | 0.60 | 74 | 590 | 660 | 15.10 |

Table 3.2: Average network parameter values for the three different network types ($n = 10$ for each network type.)

Delaunay and Voronoi networks were generated from the same number of initial seed points, but the Voronoi networks, on average, had more nodes. The ER networks required a larger number of seed points to form a completely connected network, i.e., a network without any isolated clusters, conforming to the physical network size requirement, which resulted in the ER networks having a higher number of nodes. The internal nodes in the Delaunay and ER networks were highly connected while all the internal nodes in the Voronoi networks had a connectivity of 4 (Figure 3.2).

On average, the Voronoi networks were composed of a greater number of shorter fibers (Figure 3.2). The Delaunay networks showed a nearly uniform fiber distribution (linear CDF in Figure 3.2) of fibers with length 0 to 0.45 units and then a tail to about 0.6 units. The Voronoi networks, in contrast, showed a steady decrease in probability with length (concave down CDF) and had only one fiber above length 0.4 units. The ER networks showed considerably longer fibers, including some of length greater than 1.0 units. The mean fiber length was observed to be considerably longer in the ER networks compared to the Delaunay and Voronoi geometries. The longer fibers spanning the ER networks resulted in a greater number of boundary nodes than internal ones when the network was trimmed to fit within the computational unit cube.

### 3.4.2 Fatigue simulation

Fatigue failure of the different networks was simulated to obtain an SN curve for each of the three network types. The parameters of the constitutive equation (Equation 3.2) governing the pre-failure behavior of an individual fiber remained unchanged from those noted in Table 3.1. Since the primary focus of this portion of the study was to compare the fatigue behaviors of different network geometries composed of the same fiber, any reasonable choice of fiber fatigue properties would have sufficed. The fiber SN curve used thus far (Equation 3.7) to model collagen gels required a large number of cycles to fatigue, especially at lower loads. Thus, to reduce simulation time, fibers were assigned an SN curve that was also an exponential, plus an offset, with parameters selected such that the fiber failed within a computationally acceptable number of cycles (Equation 3.9). The offset introduced a threshold value of stress, selected to be the stress generated in a fiber at a stretch of 1%, below which the fiber life was infinite.

$$S = (1.27 \times 10^6) \times e^{-\frac{N}{2}} + 1 \times 10^4 \tag{3.9}$$

Cyclic loading was simulated on 10 networks of each type and the amplitude of the oscillating load on the networks was varied to produce network fatigue between 1 to 30 cycles.

## 3.5 Results and Discussion

We begin this section by discussing the behavior of a representative network under cyclic loading, followed by a comparison of the fatigue behavior of collagen gels simulated using our model and that obtained experimentally. Finally, we examine the differences seen in the mechanics and fatigue of the different network types – Voronoi, Delaunay, and ER. Prior to simulating fatigue failure, however, the networks were confirmed to be sufficiently resolved, i.e., there was no change in the network stress-

strain response with a further increase in the number of nodes and fibers. As seen in Figure 3.3, there was almost no change in the stress-stretch curve with change in number of fibers.

### 3.5.1 Network response to cyclic loading

In the initial cycles with all fibers intact, the networks showed a non-linear stress-stretch response with overlapping loading and unloading phases, i.e., no hysteresis (path *oao* in Figure 3.4A). With the onset of fiber fatigue failure, however, the network became more compliant and stretched more at the peak load. The peak stretch then remained stable until additional fiber failure events led to further increases in network compliance (Figure 3.4A, locations ($b$-$d$)). The jumps seen in the stress-stretch curve at peak loads suggested a loss of elasticity of the material due to accumulation of fiber failure in the network similar to the stress-softening effects included in macroscale constitutive models for describing damage in soft tissues, e.g., [Pena, 2011, Martin and Sun, 2013].

The number of failed fibers within the network accumulated over time until the network lost integrity. This gradual accumulation of damage within the network through progressive failure of fibers is similar to that observed by Linka et al. [Linka et al., 2018] in their study of soft tissue fatigue using a multiscale constitutive model. Figure 3.4B shows the evolution of network strain with time. While the applied stress remained the same over all the loading cycles, with the onset of fiber failure, a larger network strain was required for the network to support the applied load.

Because of the purely elastic fibers used in the model, the networks did not show any permanent deformation, or hysterises, prior to failure like that observed in fatigue tests on, e.g., bioprosthetic heart valves [Sun et al., 2004], and included in more recent constitutive models of tissue fatigue [Pena, 2011, Martin and Sun, 2013, Martin and Sun, 2014]. Compared to these currently existing macroscale constitutive

models, however, our model captured the non-affine nature of deformations within the network. At any given stretch, only a small number of fibers carried a majority of the load (Figure 3.4C); the load shifted as fibers failed and the remaining fibers reorganized.

### 3.5.2 Collagen gel fatigue

Figure 3.5A shows the average load-stretch curve for the collagen gel stretch to failure experiments. The large dot in Figure 3.5A shows the average failure stretch (19 $\pm$ 1.7 % ) and ultimate tensile load (UTS, 0.06 $\pm$ 0.023 N) for all of the experiments (n = 6; mean $\pm$ 95% CI). Figure 3.5B shows the progressive increase in gel strain with time. Fatigue experiments on collagen gels were limited to a duration of 30 minutes ($\approx$ 2000 cycles). Gels tested at peak loads greater than or equal to 40% of the UTS exhibited failure, as shown in Figure 3.5C. Also shown is the SN curve obtained from the fiber network model using fiber properties based on those of a tendon as reported by Schechtman et al.[Schechtman and Bader, 1997]. The model curve, with no fitting parameters, showed good agreement with the collagen gel data at the higher stresses. The deviation of the model from the experiments at lower stresses, however, suggests that the fatigue behavior of an individual collagen fiber is not well approximated by the fatigue properties of a tendon. These results also indicate that fiber rearrangement within a collagen fiber network increases fatigue life for a given normalized stress.

### 3.5.3 Effects of network architecture

#### Pre-fatigue behavior

Networks of all three types showed a non-linear stress-stretch response with no hysteresis in the initial cycles. The distribution of load within all three network types was

uneven, with only a small fraction of the fibers bearing a majority of the load. This skewed distribution is visualized in Figure 3.6 by plotting the cumulative probability distribution of fiber stresses. For example, at a low applied stress of 300 Pa, a majority of the fibers (≈50%) remained stress-free for all three network types. At a higher stress of 1500 Pa, however, the fraction of unloaded fibers in the Voronoi network dropped considerably (≈14%). The percentage of stress-free fibers in the other two network types did not vary as much with the external network load. The variation of the fraction of stress-free fibers with external load seen in the Voronoi networks was indicative of a prominent 'toe-region'. A stability analysis of the truss-like networks provides a possible explanation for this variation. For large networks, the Maxwell criterion [Maxwell, 1864] requires that the mean nodal degree be greater than 6 for a three-dimensional truss to be stable. The Voronoi network, failing to satisfy this condition, possesses a larger number of nodal degrees of freedom, thus increasing the extent of fiber reorganization possible at lower loads and allowing a wider variation in the number of fibers aligning in the direction of stretch and supporting the applied force on the network.

The Kolmogorov-Smirnoff (K-S) test for cumulative distribution functions further corroborates that the differences seen in the network behavior arise due to a fundamental difference in the architectures of the three network types. The high values of the K-S statistic (Table 3.3) demonstrate that the cumulative probability distributions of fiber stresses within each network in Figure 3.6 are not drawn from the same underlying distribution ($p < 0.05$ for all comparisons).

### Whole-network-scale failure and fatigue

Prior to fatigue testing, a stretch-to-failure test was simulated on each network to obtain the UTS for the three network types (Figure 3.7). The failure stresses for the Voronoi and Delaunay networks did not differ significantly, however, the ER networks

| | Delaunay | Voronoi | Erdős-Rényi |
|---|---|---|---|
| Delaunay | - | 0.41 | 0.12 |
| Voronoi | 0.41 | - | 0.32 |
| Erdős-Rényi | 0.12 | 0.32 | - |

Table 3.3: Kolmogorov-Smirnoff statistic values comparing the cumulative probability distribution of fiber stresses for each network type prior to the onset of fiber fatigue failure. Rows and columns denote different network types, and the values indicate the K-S statistic for a comparison between the network type indicated by the row with that shown in the column. A lower value of the K-S statistic implies higher similarities in the distributions being compared.

consistently showed a lower UTS.

Semi-log plots of the mean SN data for all three network types are shown in Figure 3.8, with the stress offset by the network fatigue limit and normalized to the network UTS, i.e.,

$$S = \frac{\sigma^{net} - \sigma^{\infty}}{\sigma^{uts} - \sigma^{\infty}} \tag{3.10}$$

where $\sigma^{net}$ is the stress applied to the network face, $\sigma^{\infty}$ is the fatigue limit, i.e., the network stress below which the network possesses infinite life, and $\sigma^{uts}$ is the mean UTS for the network. Under this transformation, the SN curve for the fiber, i.e., Equation 3.9 would be a straight line on the semi-log plot, and any deviation from linearity in the SN curves of the networks would then indicate an effect arising due to the network structure-induced non-linearity. The semi-log SN plots fit well to a line in the high stress-low cycle regime with slight deviation from linearity in the low stress-high cycle limit.

Exponential curve fits to the mean values of the SN data were used to make a comparison between networks and fiber behavior (Figure 3.9). On account of the low fiber volume fractions, fibers experienced a magnitude of stress that was substantially larger than the volume-averaged stress obtained for the network. To make a meaningful comparison between fiber and network fatigue properties, the fiber SN curve was scaled by a factor of $\frac{\phi}{3}$. This scaling factor would make the fiber and network

SN curves identical for a regular cubic lattice of fibers.

For all three network types tested, at low to moderate loads, the network structure was mechanically more endurant than the single fiber (Figure 3.9). As observed in Figure 3.4C, only a few fibers supported most of the applied load and thus only a fraction of fibers accumulated significant fatigue damage with each loading cycle that the network underwent. As those few loaded fibers eventually fatigued to failure, load was transferred to fresh fibers that could still endure multiple loading cycles, and so on. This geometric shielding effect occurring within the network allowed it to endure the repeated loading longer compared to an individual fiber.

At higher magnitudes of loading, however, in addition to fatigue, fibers also began to fail because of being overstretched. The network stretch generated to support the higher applied loads was sufficient to extend some fibers beyond their critical stretch value, especially in the highly connected Delaunay and ER networks, which resulted in fiber, and subsequently, network failure leading the fiber SN curve to cross over the network curves in the high-stress low-cycle region of Figure 3.9.

Among the different network geometries, the ER networks consistently performed worst on the fatigue tests. The longer average fiber length and high connectivity in the ER networks resulted in many fibers traversing between two opposite faces of the network in just a few connections. Thus, at a given network load, the fibers experienced larger stretches, and consequently larger stresses, compared to those in the other two network types, reducing the overall life of the ER networks.

Over most of the range of loading simulated, the Delaunay networks outlasted the Voronoi. The short fiber lengths and well-connected nature of the Delaunay networks led to the uneven distribution of fiber stresses seen in Figure 3.6A with a large number of stress-free fibers. This distribution meant that the Delaunay networks had more *backup* fibers, i.e., fibers unstretched in the initial failure-free loading cycles, but which experienced gradually increased loading as network failure progressed over time and

the network reorganized.

### 3.5.4 Limitations of the model and future research directions

The model described in this paper simulates fatigue failure of truss-like fiber networks undergoing cyclic loading. This study assumed that fatigue and failure occur only within the fibers themselves, and not in the connections between fibers. Although we consider this assumption to be reasonable for our choice of flexible fiber networks, and a good first step in studying network fatigue behavior, we recognize that in many systems, e.g., in metallic foams [McCullough et al., 1999], fatigue and failure can also occur at fiber connections, requiring a different theoretical framework.

Additionally, the model analyzed network fatigue minus any growth, remodeling, and chemical effects that are present in biological tissues, e.g., mechanical overloading of collagen fibrils places them in a stable, denatured state [Veres et al., 2014], potentially delaying failure. Denaturation of collagen can also lead to changes in the rest length of fibers, and affect the local stiffness of the tissue and its capacity to remodel [Dittmore et al., 2016]. Thus, the increase in fatigue life of a network compared to an individual fiber could be magnified in a tissue that can repair itself. Further research of long-term damage of fibrous tissues will need to address such mechanobiological effects of growth and remodeling of the network components.

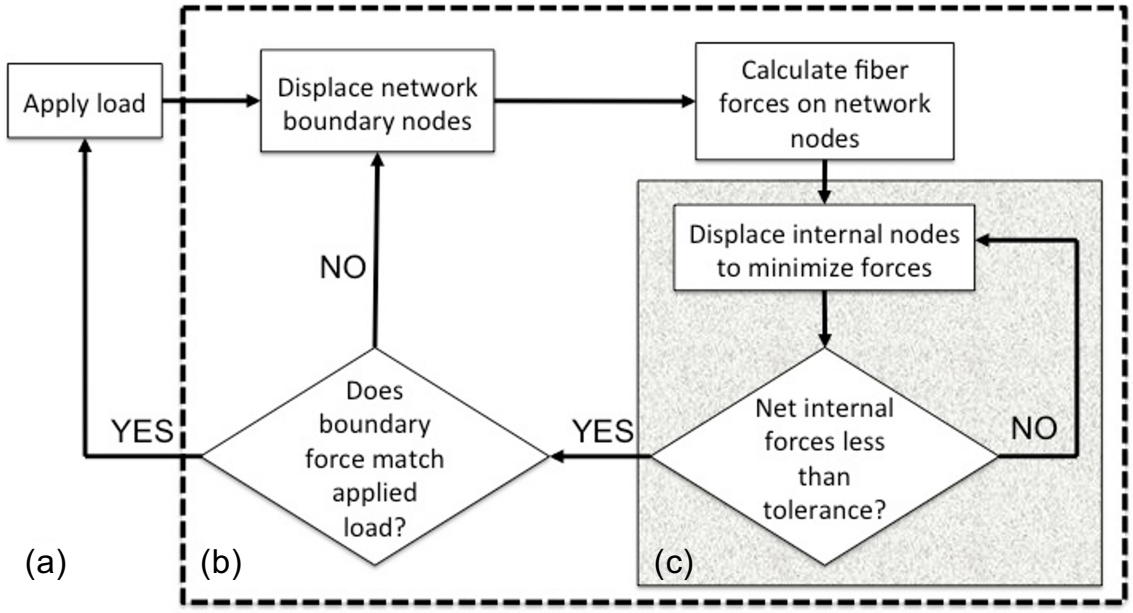


Figure 3.1: Basic outline of the force-controlled deformation model of a fiber network showing three loops. The outermost loop (a) specifies the desired loading cycle. The intermediate loop (b) adjusts the boundary displacements of the network so as to match the specified load. The innermost loop (c) calculates the equilibrium internal nodal positions for a boundary displacement specified by the intermediate loop. Upon convergence, the inner loop passes a stress value to the intermediate loop for comparison to the target stress

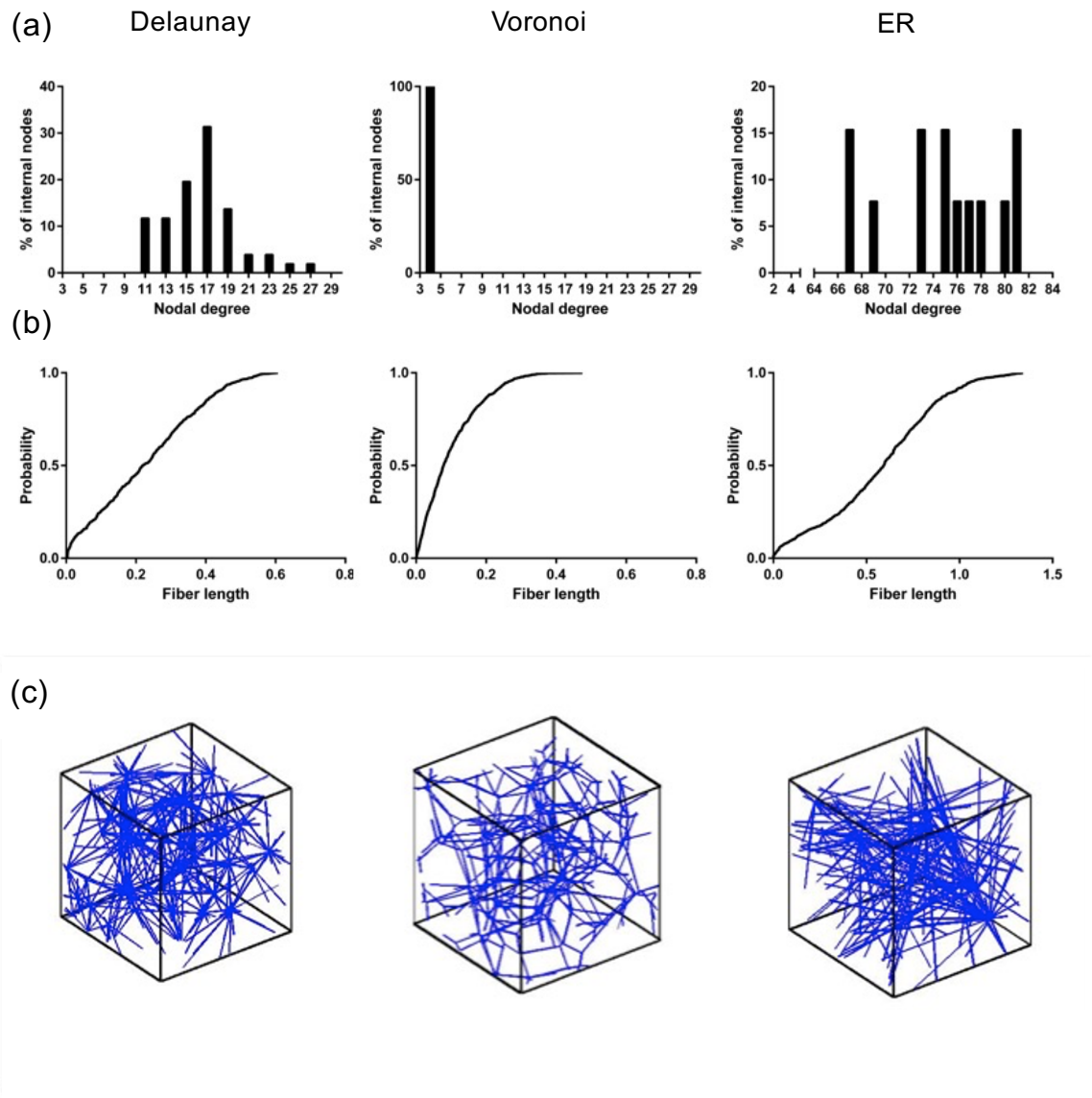


Figure 3.2: Histograms of nodal connectivity (a), cumulative probability distribution of fiber lengths in the computational domain (b), and representative images (c) of the three different network structures used – Delaunay, Voronoi, Erdős-Rényi

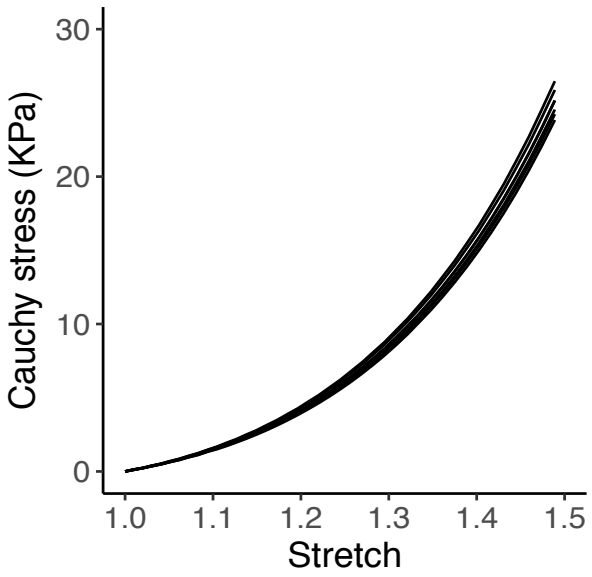


Figure 3.3: Stress-stretch plots for a network with 300, 400, 800, 1200, and 1600 nodes without fiber failure. The curves do not show any significant differences and overlap each other

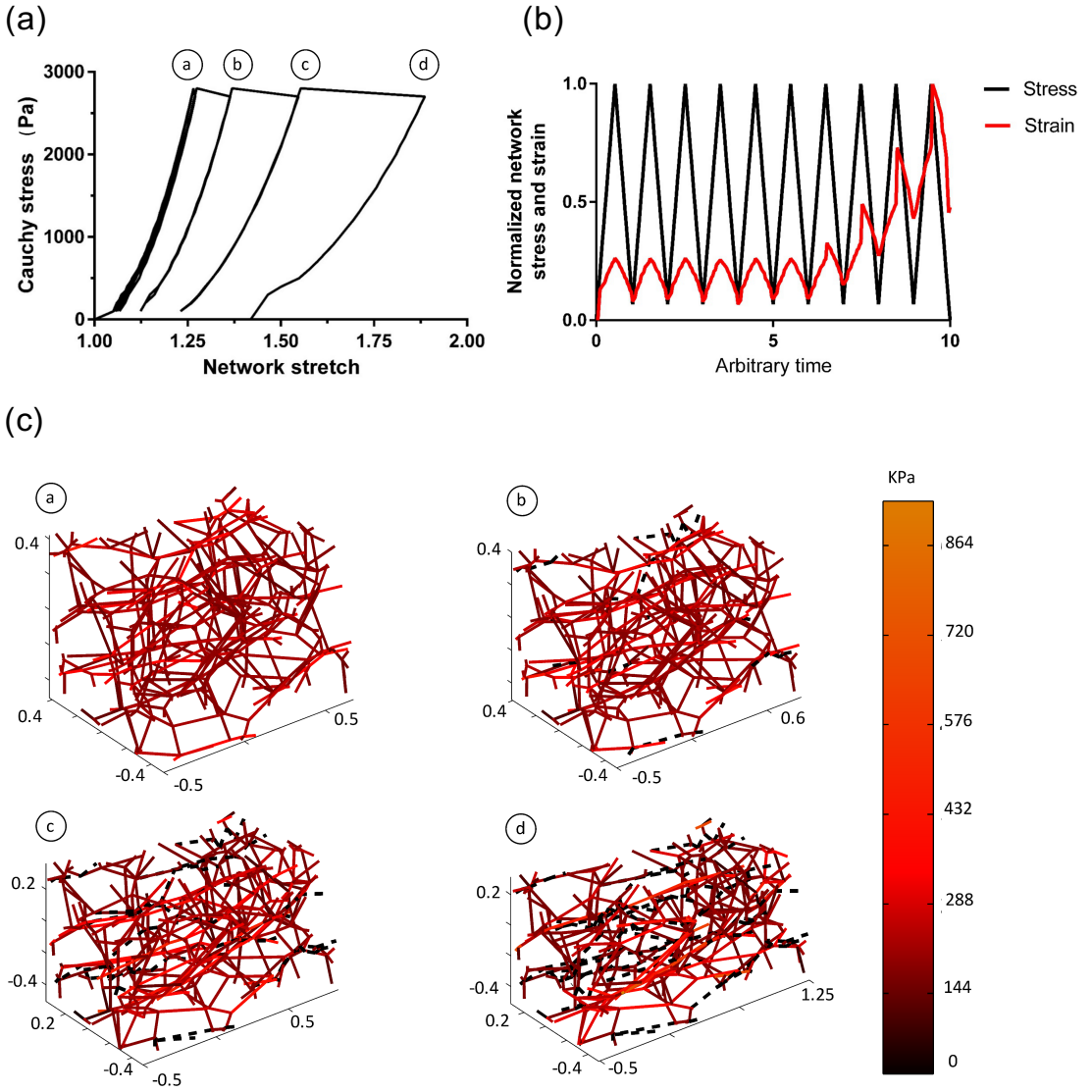


Figure 3.4: (a) A representative set of stress-stretch curves for a Voronoi network failing under fiber fatigue, (b) Evolution of network stress and strain with time, (c) Instantaneous snapshots of the network at the locations (a-d) indicated on the stress-stretch curve. The color bar shows the stress generated within each fiber and black dashed lines indicate failed fibers

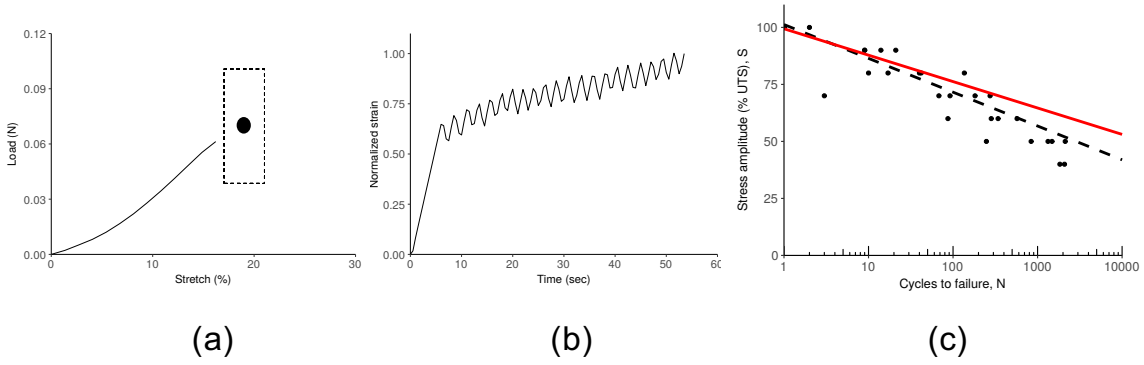


Figure 3.5: (a) Average load-stretch curve obtained for collagen gels. The dot indicates the mean failure load and stretch (n=6), with the box around the dot indicating the 95 % confidence interval. (b) The evolution of strain over time for a representative gel undergoing fatigue testing. Strain values were normalized to the strain at failure for that gel. (c) Fatigue behavior of collagen gels. Collagen gels (dots) showed a fatigue life similar to that reported previously for tendon ([Schechtman and Bader, 1997], dashed line). A Voronoi network model (solid red line) assuming tendon properties for each fiber, showed a longer fatigue life than the tendon, suggesting that the network structure increased fatigue life at a given normalized stress.

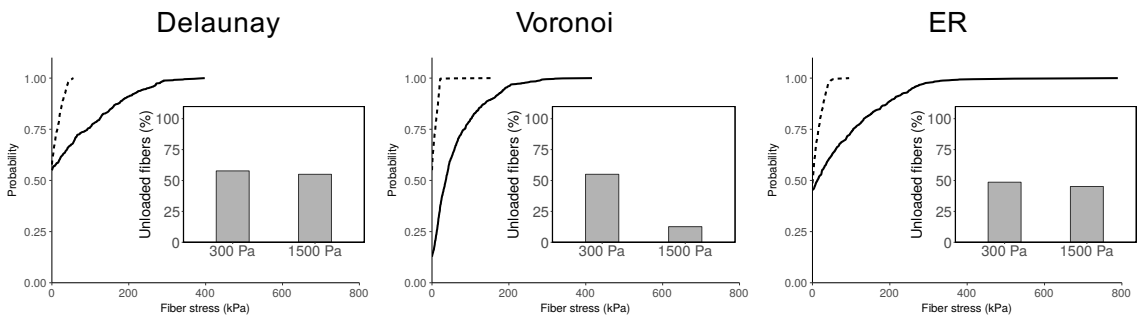


Figure 3.6: Cumulative probability distribution of fiber stresses in the different network types at a network load of 300 Pa (dashed) and 1500 Pa (solid). Inset bar graphs show the percentage of total fibers that remain stress free for the two applied network loads

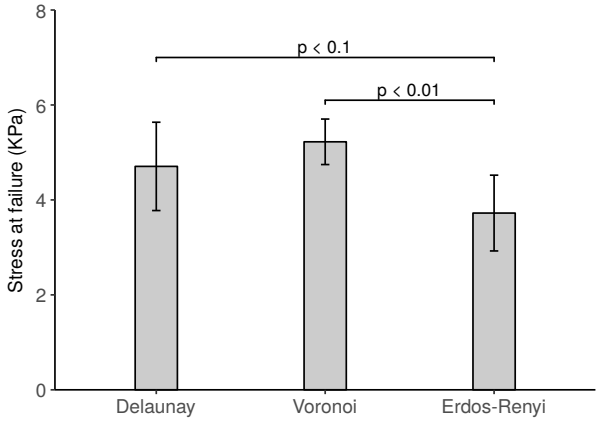


Figure 3.7: Failure stresses obtained for each network type in a stretch-to-failure simulation showing the mean ± 95 % confidence intervals (n=10)

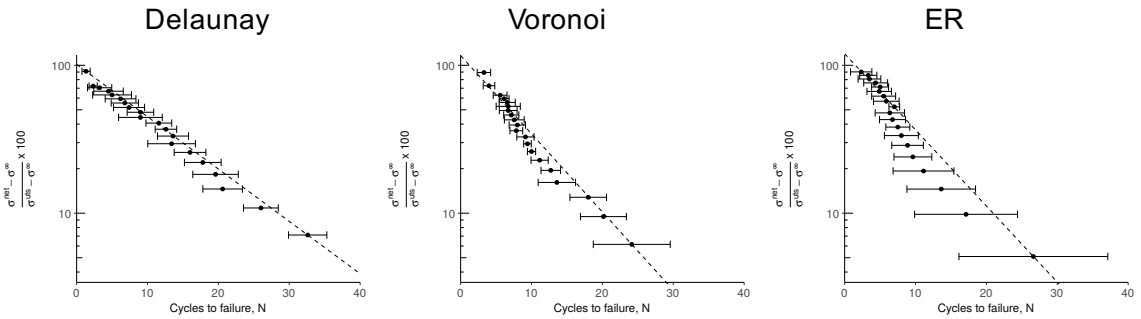


Figure 3.8: Stress-life (SN) plots obtained from simulations of the three different network structures ($n = 10$ for each network type) shown on a semi-log plot. Error bars indicate 95% confidence intervals. The stress indicated on the vertical axes is normalized to the ultimate tensile strength of the respective network type. The dashed lines are drawn passing through the first and last data points in each plot to show the deviation from linearity of the SN data, if any.

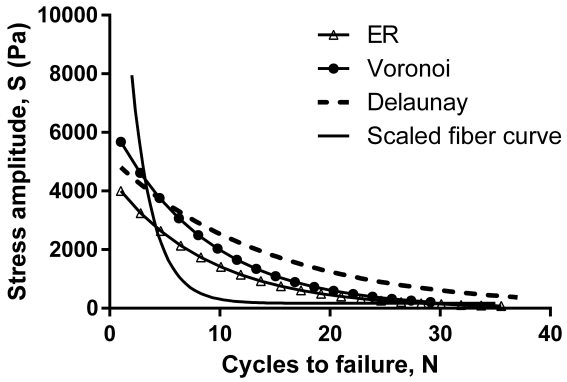


Figure 3.9: Comparison of the network and fiber SN plots. Network SN data for each network type was fit to an exponential curve

# Chapter 4

# Multiscale Model of Contractile Response of Cells Fixed on Substrates

## 4.1 Background

The contractility of the cell cytoskeleton plays a crucial role in many phenomena including cell migration [Beningo et al., 2001, Ingber, 2003], wound healing [Wood et al., 2002], and morphogenesis [Beloussov et al., 2000, Kiehart et al., 2000]. Additionally, cell contraction-driven reorganization of fibrous extracellular matrix (ECM) is important in long-range communication between cells [Harris et al., 1981, Vader et al., 2009, Abhilash et al., 2014], and has significant impact on tissue behavior over a range of length scales [Ladoux, 2009, Guo et al., 2012]. The cytoskeleton consists of a network of interconnected structural biopolymers, mainly actin, microtubules, and intermedeate filaments [Amos and Amos, 1991]. These interlinked networks play a major role in carrying and distributing both (1) the forces generated actively by actin-myosin interactions in the cell, and (2) external loads acting on the cell. Thus,

understanding and modeling the mechanics of the cytoskeletal network has fundamental implications in understanding how living cells respond to mechanical stresses.

Generally, structure-based models of the cell cytoskeleton have taken one of two different approaches: open-cell foams, and stress-supported structures. For detailed information on each of these modeling techniques, the intersted reader is directed to review article by Hatami-Marbini and Mofrad [Hatami-Marbini and Mofrad, 2015]. Briefly, open-cell foam models have used networks of interconnected struts, wherein the stretching or bending of the struts provide mechanical stiffness. Stress-supported structures have used prestressed structural members to maintain mechanical stability, with the prestress arising from the structure's external attachments, or from internal elements, e.g., tensegrity models [Ingber, 2003]. While both strategies have led to successful descriptions of the passive mechanical characteristics of the cytoskeleton, chemically-mediated events, such as actin-myosin kinetics, have proven a great challenge. Later models have added effects of molecular scale phenomena like thermal motions [MacKintosh et al., 1995, Boey et al., 1998], and the dynamic remodeling [Fabry et al., 2001, Isabey et al., 2016, Rajagopal et al., 2018] to accurately capture the behavior of the cytoskeleton.

On the other hand, several continuum models have also been developed to describe cell mechanics. Prominent among these models are models representing the cell as a liquid contained in a cortical shell [Evans and Yeung, 1989, Dong et al., 1991], models treating the whole cell as a solid continuum [Mijailovich et al., 2002, Peeters et al., 2005, Isabey et al., 2016], and biphasic models [Shieh and Athanasiou, 2003, Barreto et al., 2013, Sakamoto et al., 2016]. Continuum models have also included coupled thermodynamic and mechanical constitutive equations to predict the development and alignment of actin stress-fibers [Pathak et al., 2008], substrate stiffness-dependent cytoskeletal forces [Deshpande et al., 2006], and effects of cyclic loading [Wei et al., 2008].

While continuum models are easier to use and capture accurately the mechanical behavior at the whole-cell level, such models provide little insight into molecular level mechanisms in the cytoskeleton. Continuum models also assume all deformations occuring within the load-bearing cytoskeletal structure to be affine. Fiber networks, however, deform in a non-affine manner, which introduces inherent nonlinearities in their mechanical response. Thus, the objective of this work was to incorporate the phenomenological constitutive model of cytoskeletal contraction developed by Deshpande et al. [Deshpande et al., 2006], and modified by Pathak et al. [Pathak et al., 2008], in a multiscale framework utilizing a discrete fiber network microstructure. We use the multiscale model to simulate contracting cells adhered to substrates, and compare the predictions of stress-fiber formation with those calculated by Pathak et al. We also look at the effect of changing the network microstructure on the steady-state configuration of the contracting cell.

## 4.2 Methods

### 4.2.1 Multiscale model

Our multiscale model (Figure 4.1) consisted of a finite element (FE) mesh of the cell ($\sim \mu$m), with representative volume elements (RVEs) comprising of discrete fiber networks ($\sim$ nm), in parallel with a compressible neo-Hookean material, located at the Gauss points of each FE (with eight Gauss points assigned to each FE). The fibers represented actin networks within the cell, while the neo-Hookean material accounted for the non-fibrillar matrix surrounding the fibers. Macroscale cell stresses were determined primarily by the deformation of the microscale RVE networks, with an additional contribution arising from the neo-Hookean material. The cell nucleus was not modeled.

The commercial FE software ABAQUS [ABAQUS, 2009] was used to generate FE

meshes, and to visualize results, while all other computations were performed using an in-house FE code written in C.

### Microscale mechanics

RVE networks were modeled as trusses of cylindrical nonlinear elastic members (fibers) connected at pin joints (nodes) allowing free rotation.

**Single-fiber mechanics** Each fiber in the RVE networks was assigned a passive constitutive behavior of the form

$$\sigma_p = \frac{E}{B}\left(e^{B\frac{\lambda^2-1}{2}} - 1\right) \tag{4.1}$$

where $\sigma_p$ is the passive stress generated within the fiber at a stretch $\lambda$, $E$ is its stiffness, and $B$ controls fiber nonlinearity. At infinitesimal stretch, Equation 4.1 reduces to a linear material with Young's modulus $E$. The constitutive equation was adapted from a previous structural model [Billiar and Sacks, 2000].

Additionally, fiber contractility was introduced in the model by using the Hill-like [Hill, 1938] model described by Pathak et al. [Pathak et al., 2008], translated from Pathak's continuum contraction model to our discrete networks. Fiber contractility within the cell is initiated by a signaling cascade triggered by an external biochemical or mechanical perturbation. This external signal was modeled as an exponentially decaying signal given by $C = exp\left(\frac{-t}{\theta}\right)$, where $C$ is the strength of the signal at time $t$, and $\theta$ controls its rate of decay. The external signal affected the activation level $\eta$ of each fiber in the network, which depended on the active contractile stress within the fiber $\sigma_a$, and was governed by a linear kinetic law having the form

$$\dot{\eta} = (1-\eta)\frac{Ck_f}{\theta} - \left(1 - \frac{\sigma_a}{\sigma_0}\right)\frac{\eta k_b}{\theta} \tag{4.2}$$

where $k_f$ and $k_b$ are constants governing the rates of the forward and backward kinetics, respectively, $\sigma_0$ is the maximum isometric tension possible in a fiber, and the overdot indicates a time derivative (Figure 4.2(a)). Physically, $\eta$ represents the ratio of the polymerized actin and phosphorylated myosin concentrations within a stress-fiber bundle to the maximum concentrations permitted by biochemistry. Thus, higher actin-myosin concentrations would result in higher $\eta$ values and thus higher contractile forces in the network. The stress dependence in Equation 4.2 accounted for the depolymerization of actin fibers while ensuring stability of fibers under isometric tension, i.e., $\sigma_a = \sigma_0$.

Finally, the active tension generated in a fiber was related to its rate of stretch $\dot{\lambda}$ as

$$\frac{\sigma_a}{\sigma_0} = \begin{cases} 0 & \dot{\lambda} < \dfrac{-\eta}{k_v} \\ 1 + \dfrac{k_v}{\eta}\dot{\lambda} & \dfrac{-\eta}{k_v} \leq \dot{\lambda} \leq 0. \\ 1 & \dot{\lambda} > 0 \end{cases} \tag{4.3}$$

where $k_v$ is a constant representing the sensitivity of the fiber to the activation signal (Figure 4.2(b)). The active contraction stress in a fiber in Equation 4.3 arises due to the spontaneous cycling of myosin motors on actin filaments. Contractile tension in the fiber is greatest when it is held in an isometric condition, similar to the Hill-Huxley model [Huxley, 1957], and the tension in the fiber falls as the fiber is allowed to shrink due to the reduced likelihood of the myosin heads engaging actin fibers. If the fiber experiences extension, then the tension generated within it is equal to the maximum isometric tension $\sigma_0$.

**Network mechanics** Motion of the RVE network boundaries caused the fibers within the network to deform and apply forces on all network nodes. At every time step, however, the equilibrium solution of the network force problem had no net force on any internal node, i.e., nodes not lying on the boundary of the network domain.

The nodal positions corresponding to this equilibrium solution were calculated using Newton's method by computing the Jacobian matrix $J$ such that $J_{ij} = \dfrac{\partial f_i}{\partial x_j}$, where $f$ is total force on a node, and $x$ is its position. We used backward-Euler integration for the time dependent terms in the fiber constitutive equations. Newton iteration was applied at every time step until the net force on all internal nodes was less than a specified relative tolerance ($10^{-8}$). The volume-averaged Cauchy stress in the deformed network was then calculated as [Chandran and Barocas, 2006b]

$$\left\langle \sigma_{ij}^{network} \right\rangle = \frac{1}{V} \oint x_j f_i ds = \frac{1}{V} \sum_b f_i^b x_j^b \tag{4.4}$$

where $\langle \cdot \rangle$ denotes volume-average, $x_j^b$ is the coordinate along the $j$ direction, $f_i^b$ is the force in the $i$ direction, acting on the boundary node $b$, and summation occurs over all boundary nodes.

### Microscale network structure

**Network generation** We used networks with three different architectures (Figure 4.3) to investigate the effect of microstructure on the contraction of the cell:

- **Delaunay [Delaunay, 1934] tessellation**: Connections were formed between randomly generated seed points such that the circumsphere of any tetrahedron formed by a set of four connected nodes did not contain any other network node. Networks were generated using the MATLAB function *delaunay* [MATLAB, 2013]. Delaunay networks have been used previously in modeling fibrous tissues [Aghvami et al., 2016]. They are highly connected, with an average nodal degree of 12.

- **Voronoi [Voronoi, 1908] tessellation**: Three-dimensional space was divided among the initial randomly generated seed points, forming polyhedral regions, such that every point inside a polyhedron was located closest to the seed point

corresponding to that region and located within it. The edges of the Voronoi polyhedra calculated from the seed points represented fibers, and their vertices represented network nodes. Three-dimensional Voronoi cells were generated using the MATLAB function *voronoin* [MATLAB, 2013]. Voronoi networks have been shown to provide a close approximation to collagen gel mechanics [Nachtrab et al., 2011], and have been used in previous studies modeling the mechanics of collagenous connective tissues [Zhang et al., 2013]. Voronoi networks are considerably looser than Delaunay networks, with nodal degree of 4 for each interior node.

- **Arruda-Boyce-like network [Arruda and Boyce, 1993]**: This network consisted of eight nodes located at each corner of a cube, connected to a node in the center of the cube. Arruda-Boyce networks have previously been used to describe the elasticity of isotropic polymers such as rubber [Arruda and Boyce, 1993], as well as the mechanics of tissues, e.g., tendons [Kuhl et al., 2005]. For identical fibers as used here, deformations in the Arruda-Boyce model are affine with the macroscopic scale.

**Network fiber alignment** Fiber alignment within a network was measured using a length-weighted 3-D orientation tensor [Sander et al., 2009a] defined as

$$\mathbf{\Omega}_{net} = \frac{\sum l_i}{l_{total}} \begin{bmatrix} \cos^2\alpha_i & \cos\alpha_i\cos\beta_i & \cos\alpha_i\cos\gamma_i \\ \cos\alpha_i\cos\beta_i & \cos^2\beta_i & \cos\beta_i\cos\gamma_i \\ \cos\alpha_i\cos\gamma_i & \cos\beta_i\cos\gamma_i & \cos^2\gamma_i \end{bmatrix}, \tag{4.5}$$

where $\alpha_i$, $\beta_i$, and $\gamma_i$ are the angles between the $i^{\text{th}}$ fiber and the X, Y, and Z axes, respectively, $l_i$ is the length of the fiber, $l_{total}$ is the total length of fibers in the network, and summation occurs over all fibers. The diagonal entries of $\mathbf{\Omega}_{net}$ vary from 0, for no alignment, to 1, indicating all fibers aligned in a single direction. For isotropic

networks, all diagonal entries equal 0.3. The eigenvector of $\mathbf{\Omega}_{net}$ corresponding to the maximum eigenvalue indicated the preferred direction of alignment of fibers, and the difference between the maximum and middle eigenvalues was used as a measure of the strength of alignment.

### Length scale coupling

The method by which macroscale and microscale were coupled has been described previously [Chandran and Barocas, 2006b]. Briefly, macroscale deformations were mapped to deformations of the boundaries of RVEs located at Gauss points using tri-linear basis functions. Next, a force balance was performed on the RVE network as described above, and volume-averaged microscale stresses were computed using Equation 4.4. The microscale network stresses were then appropriately scaled and passed back to the macroscale as stresses at the corresponding Gauss points within each FE. The scaling factor relating the macroscale and the microscale was determined by the volume fraction of fibers in the RVE networks and the dimensions of the fibers.

$$X = \sqrt{\frac{\pi r^2 l_{total}}{\phi}} \tag{4.6}$$

where $X$ is the physical dimension of the RVE network, $r$ is the radius of the fibers, $l_{total}$ is the total length of fibers in the network in computational units, and $\phi$ is the desired fiber volume fraction. The macroscale deformation that balanced stresses within the continuum was then determined iteratively. This method of coupling length scales has been used previously to simulate the passive mechanical behavior of a range of soft tissues [Sander et al., 2009b, Witzenburg et al., 2016, Zhang et al., 2018].

### 4.2.2 Cells on concave ligand patterns on rigid surfaces

Using the multiscale model described above, we first simulated cells fixed on concave-pattern substrates following the experiments of Théry et al. [Théry et al., 2006] and the computations of Pathak et al. [Pathak et al., 2008]. We compared our results with those obtained by the 2-D continuum model of Pathak.

Théry et al. [Théry et al., 2006] analyzed the structure of cells adhered onto V, T, Y, and U shaped ligand patterns printed on an otherwise non-adherent surfaces (Figure 4.4). Among other data, Théry et al. recorded the actin stress-fiber distribution in cells fixed on concave patterns, and they measured the radius of curvature of the non-adhered edge of the cell at steady-state. The radius of curvature $r$ of the free edge was calculated using

$$r = \frac{(l^2/4) + h^2}{2h}, \tag{4.7}$$

where $l$ is the length of the line segment connecting the ends of the non-adhered edge, and $h$ is the perpendicular distance from that line segment to the midpoint of the free edge in the deformed cell. The ends of the free edge were defined as the points where the non-adhered edge first makes contact with the ligand patch. In our model, this corresponded to the first points on both ends of the non-adhered edge that were fixed.

Material parameters used in the multiscale model are shown in Table 4.1. All parameters governing the active contraction of fibers, except $\sigma_0$, were selected to match those used by Pathak et al. The maximum contration force possible in a fiber $\sigma_0$ was used as a single fitting parameter. The passive stiffness and non-linearity parameters for fibers were selected from a previous multiscale model of the passive mechanical behavior of a cell embedded in extra cellular matrix [Lai et al., 2013].

First, using a Delaunay microstructure, we calibrated our model to match the

| | Parameter | Value |
|---|---|---|
| Passive fiber parameters [Lai et al., 2013, Knappeis and Carlsen, 1962] (Eq. 4.1) | $E$ | 10 GPa |
| | $B$ | 2.5 |
| | fiber radius | 3.25 nm |
| Active fiber parameters [Pathak et al., 2008] (Eqs. 4.2, 4.3) | $\theta$ | 720 sec |
| | $k_f$ | 10 |
| | $k_b$ | 1 |
| | $\sigma_0$ | 3 GPa |
| | $k_v$ | $2.14\times10^4$ sec |
| neo-Hookean parameters [Pathak et al., 2008] | Young's modulus | 80 Pa |
| | Poisson's ratio | 0.3 |

Table 4.1: Parameters used in the multiscale model RVE networks.

steady-state radius of curvature of the free edge of the V shape measured by Théry et al. With the appropriately calibrated model, we then simulated cells fixed on the remaining patterns, i.e., T, Y, and U. Next, using the same parameters as above, we reran the V shape simulation with Voronoi and Arruda-Boyce-like networks to investigate whether the contracting network microstructure affected the steady-state of the cell.

FE meshes of the cells were generated to match the planar dimensions reported by Théry et al., assuming a uniform thickness of 1 $\mu$m. Each FE was assigned a network picked randomly from a pool of networks, and all networks in the undeformed configuration were generated to be as close as possible to perfectly isotropic.

## 4.3 Results and Discussion

### 4.3.1 Stress distribution and fiber alignment

Figure 4.5 shows the distribution of the normalized maximum principal stress for each concave pattern as computed by the continuum model of Pathak et al. (Figure 4.5(a)), and as predicted by our multiscale model (Figure 4.5(b)). The stress distributions in the multiscale model (Figure 4.5(b)) are not symmetric since the RVE networks

in the undeformed configuration were almost, but not entirely, isotropic. Assigning a different RVE network to each FE – chosen at random from a pool of networks – also contributed to the spatial inhomogeneity of the material properties.

Fiber orientations predicted by the multiscale code are also consistent with the experimental results of Théry et al., and agree well with the predictions of Pathak et al. The lines in Figure 4.5(b) indicate the direction of fiber alignment, i.e., the direction of the eigenvector corresponding to the maximum eigenvalue, and the length of the lines indicates strength of alignment, calculated as described in the 'Methods' section. This measure of fiber alignment is similar to the circular variance measure used by Pathak et al. to predict stress-fiber directions (lines in Figure 4.5(a)). Network fibers primarily orient along the non-adhered edge as the cell contracts. The orientation of the networks in the interior of the cell where the cell is fixed to the substrate remains almost isotropic. The regions of high and low fiber alignment are indicated on the V shape in Figure 4.5(b) with the labels H and L, respectively.

With proper calibration of the maximum possible isometric tension in a network fiber, the radii of curvature of the non-adhered edges predicted by the multiscale model agree well with the experimental results of Théry et al. (Figure 4.6). The change in the radii for the different substrate patterns – V, T, Y, and U – shows a trend similar to the predictions of the continuum model, however, for each shape, the non-adhered edges in the multiscale model show higher contraction resulting in a smaller radius of curvature. This difference can in part be attributed to different stress calibrations, and it may also have been affected by the three-dimensionality of our model vs. Pathak's 2-D model.

### 4.3.2 Effect of RVE microstructure on steady-state shape

The effect of microscale network architecture can be seen in Table 4.2. For an Arruda-Boyce-like microstructure, the radius of curvature of the free edge of the cell fixed

| Network type | Radius of curvature ($\mu$m) |
|---|---|
| Delaunay | 44.78 |
| Voronoi | 57.49 |
| Arruda-Boyce | >1000 |

Table 4.2: Steady-state radius of curvature of the free edge for a cell fixed on a V-shaped substrate for different choices of RVE network structures.

on a V-shaped substrate is much larger than that obtained using a Delaunay or Voronoi network. The Arruda-Boyce network structure is inherently affine, and when constructed to fit in a cube as we did, it also becomes perfectly isotropic prior to contraction. The cell model using the Arruda-Boyce-like network mainly deformed along the thickness of the cell, flattening the cell as the fibers contracted, resulting in a mainly straight free edge. The Delaunay and Voronoi networks on the other hand show non-affine deformations within the network, with the latter being more non-affine than the former.

The steady-state radius of curvature of the non-adhered edge when using a Voronoi microstructure was slightly greater than that obtained using Delaunay networks with the same set of material parameters. A possible explanation for this difference in curvature lies in the low nodal connectivity of Voronoi networks. As shown by Žagar et al. [Žagar et al., 2015], the resistance to deformation arising in a cross-lined network is governed by two fundamental mechanisms, first, a regime dominated by fiber rotation, followed by a regime wherein axial deformation of the fibers is the primary mode of deformation. Given their low nodal connectivity, there is a greater capacity for fiber rotation and reorganization within the Voronoi networks, resulting in the reduced contraction of the free edge over time.

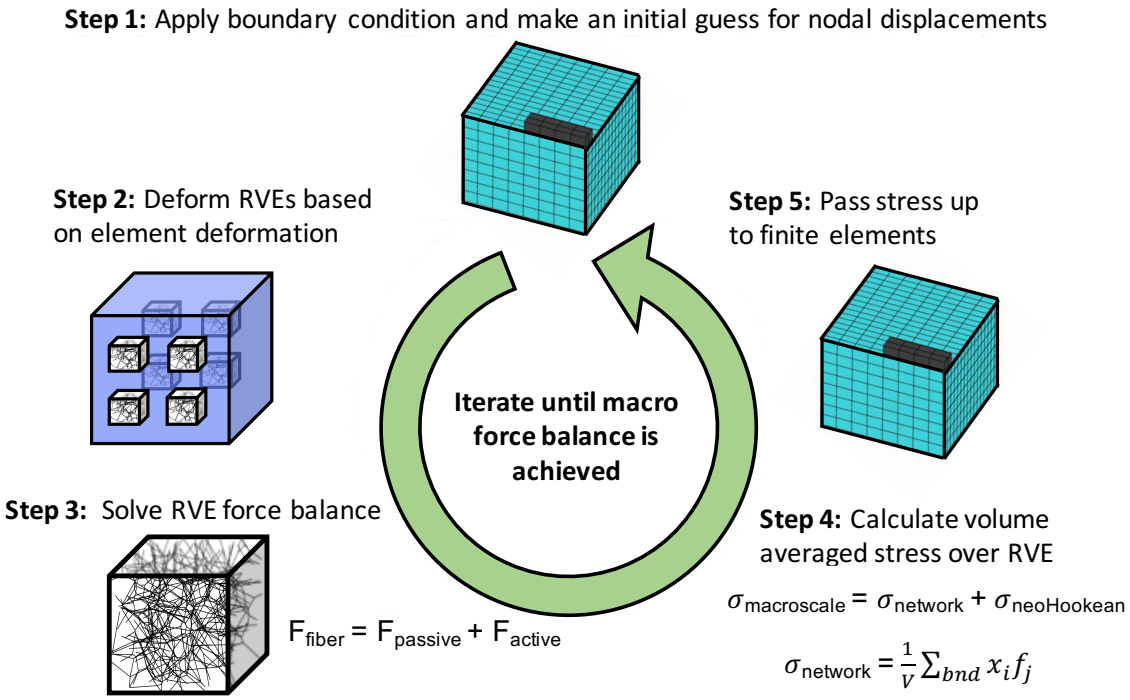


Figure 4.1: Schematic showing the working of the multiscale approach using the deformation of microscale discrete fiber networks to calculate macroscale stresses.

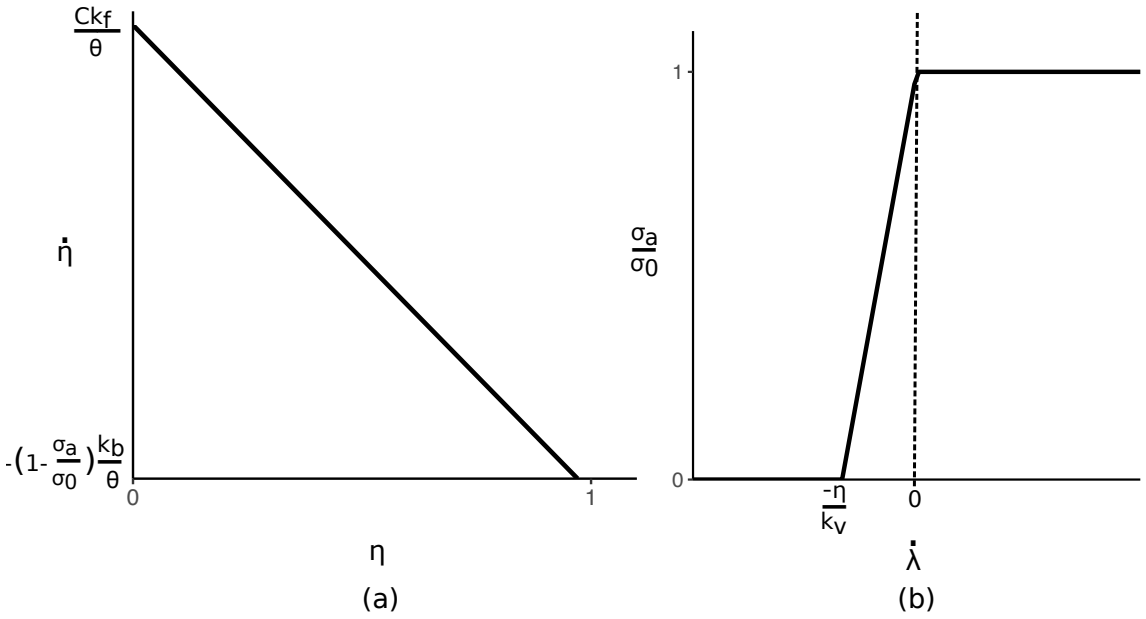


Figure 4.2: (a) Plot showing the dependence of the activation level of a fiber $\eta$ on the external signal $C$, and the contractile stress $\sigma_a$ within the fiber, (b) contractile stress generated within each fiber depended on the rate of stretch of each fiber $\dot{\lambda}$, and the level of activation of the fiber.

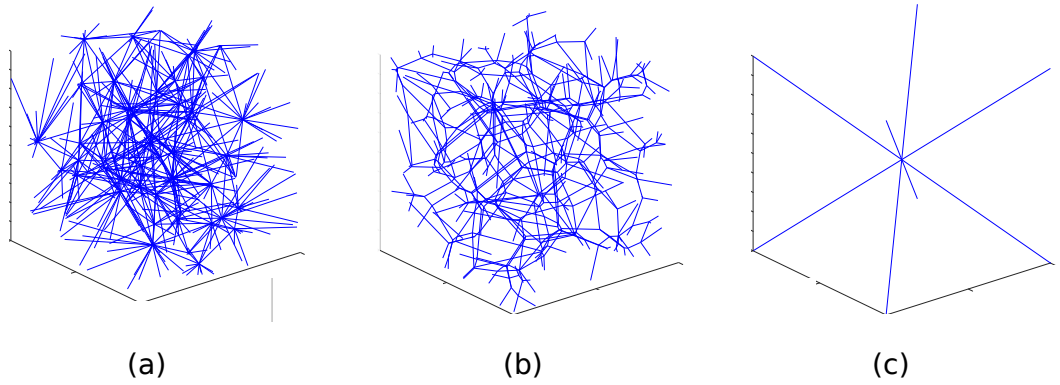


Figure 4.3: Representative images of (a) Delaunay, (b) Voronoi, and (c) Arruda-Boyce network structures.

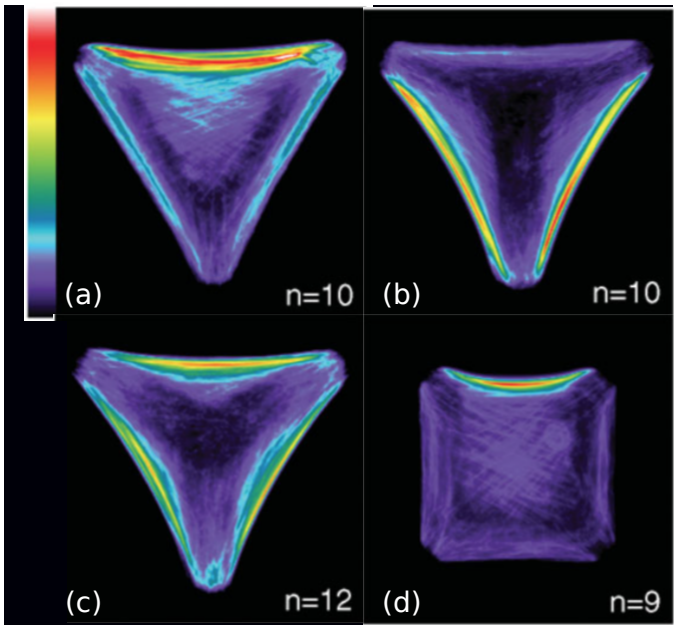


Figure 4.4: Distribution of actin obtained for cells fixed on (a) V, (b) T, (c) Y, and (d) U shaped substrates. Image reproduced with some modification from [Théry et al., 2006]. Copyright ©John Wiley & Sons, Ltd.

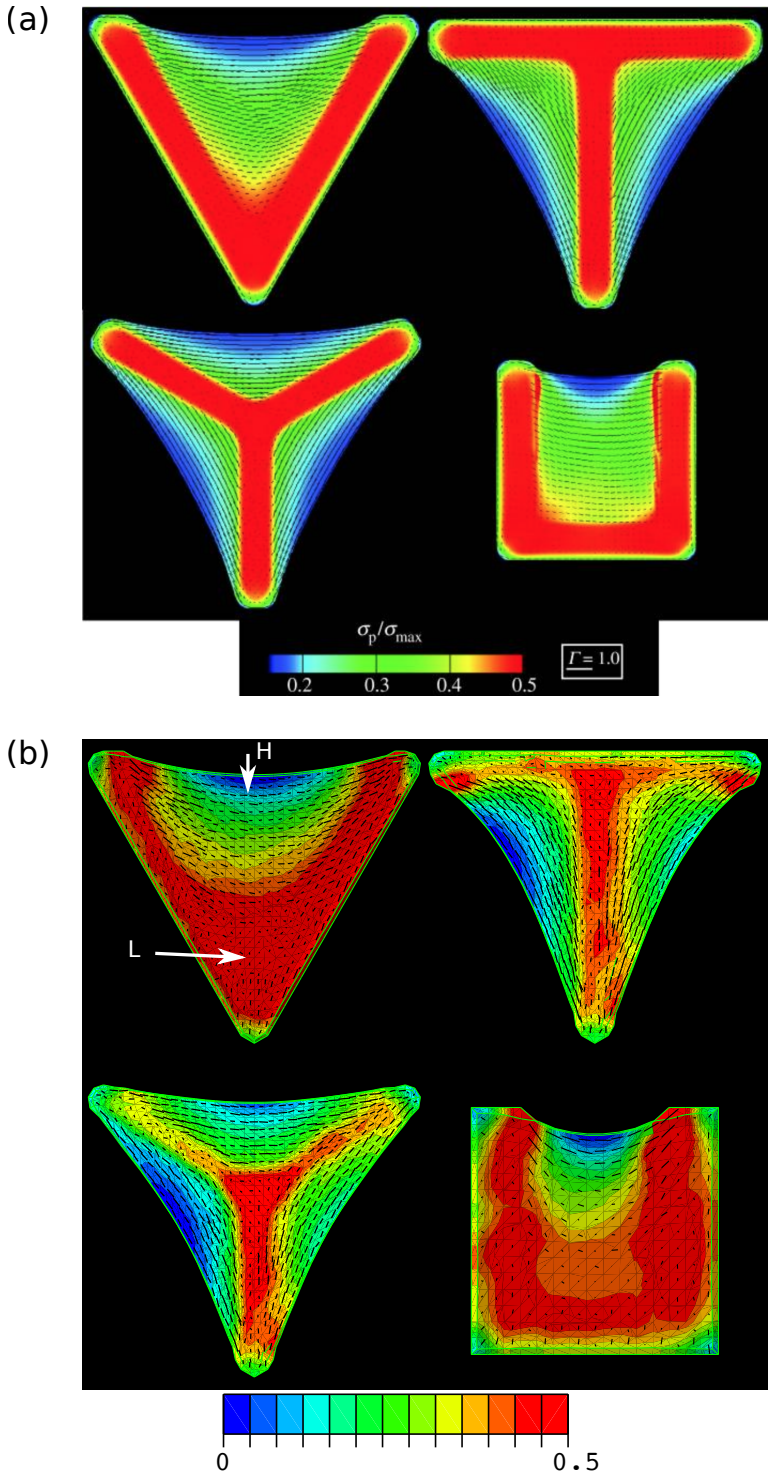


Figure 4.5: Stress distribution within the cell showing the normalized maximum principal stress for (a) the continuum model of Pathak et al. [Pathak et al., 2008], and (b) the multiscale model. The lines in each plot show the direction and strength of alignment of fibers as predicted by the respective models. The H and L labels on the V shape in (b) show the regions of high and low fiber alignment, respectively.

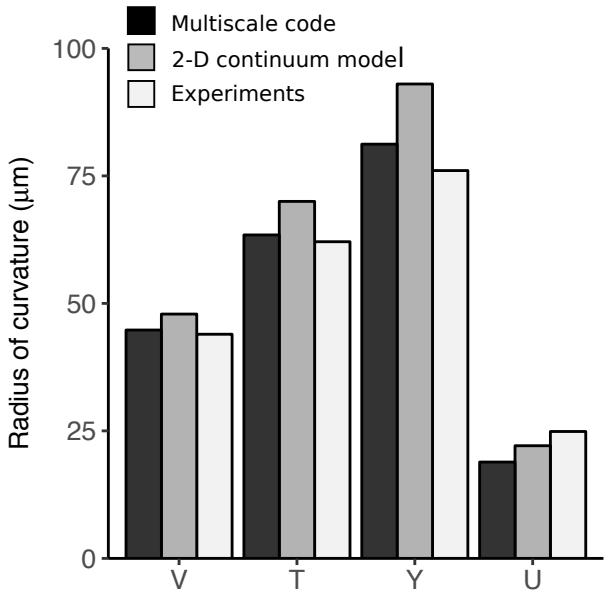


Figure 4.6: Radii of curvature of the non-adhered edges of a cell fixed on concave patterns – V, T, Y, and U – as predicted by the multiscale code, by the continuum model of Pathak et al. [Pathak et al., 2008], and obtained experimentally [Théry et al., 2006]

# Chapter 5

# Failure of the Porcine Ascending Aorta: Multidirectional Experiments and a Unifying Microstructural Model

The content of this chapter was published as a research article in the *Journal of Biomechanical Engineering* by Witzenburg, Dhume, Shah, Korenczuk, Wagner, Alford, and Barocas [Witzenburg et al., 2016]. My contribution was to the modeling aspect of this work, including generating microscale networks to match histological data, setting up the multiscale model, and appropriately calibrating the multiscale model to match experimental data.

## 5.1 Background

The ascending thoracic aorta (Figure 5.1(a)) supports tremendous hemodynamic loading, expanding ($\approx 11\%$ area change [Mao et al., 2008]) during systole and elas-

tically recoiling during diastole to augment the forward flow of blood and coronary perfusion [2]. Although it is only about 5 cm long [Gray et al., 2000, Dotter et al., 1950] (15% of the total length of the thoracic aorta), the ascending aorta is involved in 60% of all thoracic aortic aneurysms [Isselbacher, 2005]. Aneurysm dissection and rupture (resulting in imminent death) are the primary risks associated with ascending thoracic aortic aneurysm (ATAA), occurring when the remodeled tissue is no longer able to withstand the stresses generated by the arterial pressure. Unfortunately, surgical repair of an ATAA also involves considerable risk. Statistically, death from rupture becomes more likely than death during surgery at an ATAA diameter over 5.5 cm, setting the current interventional guidelines [Isselbacher, 2005, Davies et al., 2002, Davies et al., 2006, Elefteriades, 2010]. Aortic dissection and rupture remain difficult to predict, however, occurring in a significant number of patients with smaller aneurysms [Isselbacher, 2005, Davies et al., 2006, Pape et al., 2007] while many patients with ATAA diameters above 5.5 cm do not experience aortic dissection or rupture. New surgical guidelines have been proposed based on aneurysm growth rate [Davies et al., 2002, Elefteriades, 2010] and normalized aneurysm size [Davies et al., 2006, Svensson et al., 2003, Kaiser et al., 2008], but growth rates can be difficult to determine and require sequential imaging studies [Berger and Elefteriades, 2012], and normalizing aneurysm size is still a controversial strategy [Matura et al., 2007, Nijs et al., 2014, Holmes et al., 2013, Etz et al., 2012]. A better understanding of aortic wall mechanics, especially failure mechanics, is imperative.

Because of the complex geometry of the aortic arch (aggravated in the case of aneurysm) and the complex mechanical environment surrounding an intimal tear, the stress field in a dissecting aorta involves many different shear and tensile stresses. It is therefore necessary to study tissue failure under as many loading conditions as possible. Tissue from the ascending aorta has been tested in a variety of configurations (reviewed by Avanzini et al. [Avanzini et al., 2014]), with uniaxial and equibiaxial

stretch tensile tests being the most common. In-plane uniaxial [Vorp et al., 2003, Iliopoulos et al., 2009, Pichamuthu et al., 2013] and biaxial tension tests [Shah et al., 2014, Okamoto et al., 2002, Azadani et al., 2013, Babu et al., 2015] provide information on tensile failure in the plane of the medial lamella ($\sigma_{\theta\theta}$, $\sigma_{zz}$), and the biaxial tests can provide some additional information on in-plane shear ($\sigma_{\theta z}$). Although the dominant stresses in these tests may be the primary stresses during vessel rupture, they are not those driving dissection. Stresses near an advancing dissection include a combination of radial tension ($\sigma_{rr}$) and transmural shear ($\sigma_{r\theta}$, $\sigma_{rz}$) [van Baardwijk and Roach, 1987], which are more difficult to test experimentally. Peel tests on pieces of artery [Sommer et al., 2008, Tong et al., 2011, Tsamis et al., 2014, Kozuń, 2016] or aneurysm [Pasta et al., 2012] provide insight into the failure behavior of the tissue in radial tension ($\sigma_{rr}$), loading perpendicular to the medial lamella, as does direct extension to failure in the radial direction [Sommer et al., 2008]. To examine transmural shear stresses ($\sigma_{r\theta}$, $\sigma_{rz}$), the shear lap test, well established in the field of adhesives [ASTM, 2014] and used by Gregory et al. [Gregory et al., 2011] to study interlamellar mechanics of the annulus fibrosus of the intervertebral disk, is an attractive option. In the present work, our first objective was to obtain a more complete picture of artery failure mechanics by using a combination of in- plane uniaxial and equibiaxial, shear lap, and peel tests to cover all three-dimensional loading modalities (Figs. 5.1(b) and 5.1(c)). To the best of our knowledge, this study was the first to generate data on the interlamellar shear strength of aortic tissue in this manner.

The need for better experiments is complemented by the need for better computational models of tissue failure. Many theoretical models have been utilized to describe ATAAs, but only a few have addressed failure and dissection [Volokh, 2008, Gasser and Holzapfel, 2006, Ferrara and Pandolfi, 2008, Wang et al., 2014]. Volokh [Volokh, 2008] used a softening hyperelastic material model and a two-fiber family strain energy density function within the context of a bilayer arterial model to examine the

failure of arteries during inflation. This model yields valuable results concerning rupture but does not address dissection. An impressive model of dissection mechanics was put forward by Gasser and Holzapfel [Gasser and Holzapfel, 2006], employing a finite-element (FE) model with independent continuous and cohesive zones. The Gasser-Holzapfel model combines a nonlinear continuum mechanical framework with a cohesive zone model to investigate the propagation of arterial dissection, and it agreed well with experimental peel test results [Sommer et al., 2008]. However, the reliance on the *a priori* definition of the location and size of the cohesive zone, the zone in which microcrack initialization and coalescence are confined, limits the model. In addition, the model does not address microscale failure; that is, it does not capture the complex fiberfiber and fibermatrix interactions during dissection and does not account for the lamellar structure of the vessel wall. Similar results to those of Gasser and Holzapfel were found by Ferrara and Pandolfi [Ferrara and Pandolfi, 2008], who investigated the impacts of mesh refinement and cohesive strength on dissection. Alternatively, Wang et al. [Wang et al., 2014] used an energy approach, rather than a cohesive zone, to simulate dissection in two dimensions. In addition to tear propagation, Wangs model was capable of simulating tear arrest, reflecting the clinical observation that dissection often occurs in stages. The energy approach presented, however, requires a priori definition of crack direction, does not allow changes in propagation direction, and does not address microscale failure. Advantages of a multiscale model include its ability to link observed macroscale properties to changes in microscale structure and its allowance of spontaneous failure initiation location and growth.

Recently, we utilized a multiscale model to describe *ex vivo* testing results of porcine ascending aorta in both uniaxial and equibiaxial extension [Shah et al., 2014]. The tissue microstructure was idealized as a single network of uniform-diameter fibers functioning in parallel with a neo-Hookean component that accounted for all nonfib-

rillar contributions. Although that model worked well for in-plane behavior, the lack of an accurate representation of the lamellar structure rendered it inaccurate for out-of-plane data and failed to take advantage of the full capabilities of the multiscale computational framework. It was clearly necessary to modify the simplified microstructural organization of our earlier work and consider the layered structure of the medial lamellae, including in particular the interlamellar connections, in order to capture the tissues biomechanics in all loading conditions more relevant to dissection. Therefore, the second and third objectives of this study were to generate a tissue-specific microstructure based on the layered structure of the aorta and to utilize the new microstructure to build a multiscale model capable of replicating experimental results from all the mechanical tests (uniaxial extension to failure, equibiaxial extension, peel to failure, and shear lap failure) performed.

## 5.2 Methods

### 5.2.1 Experiments

Ascending aortic tissue was obtained from healthy adolescent male swine ( $\approx$6 months; 87.4 $\pm$ 9.6 kg, mean $\pm$ SD) following an unrelated *in vivo* study on right atrial radio frequency ablation and stored in 1% phosphate-buffered saline (PBS) solution at 4° C. Tissue specimens were tested within 48 h of harvest while immersed in 1% PBS at room temperature. Per our previous study [Shah et al., 2014], a ring of tissue was dissected from the ascending aorta and cut open along its superior edge (Figs. 5.2(a) and 5.2(b)). The tissue specimen was cut into small samples, both axially and circumferentially aligned, for mechanical testing. Several samples were obtained from each aorta (a typical dissection and testing plan is shown in Figure 5.2(c)).

Four different loading modalities were utilized to characterize the tissue mechanically: uniaxial, equibiaxial, peel, and lap tests (Figure 5.3). Planar uniaxial and

equibiaxial tests, which characterized the tissue in tension along the medial lamella ($\sigma_{\theta\theta}$, $\sigma_{zz}$, $\sigma_{\theta z}$), were performed and described previously [Shah et al., 2014]. The intima, adipose tissue, and adventitia were removed from samples tested uniaxially and biaxially. While these testing modalities are relevant to the rupture of the vessel, dissection of the ascending aorta occurs when the medial lamellae separates into two layers and thus is highly dependent on the behavior of the tissue across lamellae. Thus, two additional mechanical testing modes were utilized. Peel tests (cf. [Sommer et al., 2008, Tong et al., 2011, Pasta et al., 2012]) were performed to quantify the tissues tensile response perpendicular to the medial lamellae ($\sigma_{rr}$) and subsequent dissection of the media into two layers. Shear lap tests were performed to quantify the tissues response when exposed to shear along the medial lamella ($\sigma_{rz}$, $\sigma_{r\theta}$). The two protocols are described in detail below.

**Peel Tests** : The peel test (Figure 5.3(c)) measures the adhesive force between two layers as they are pulled apart. For each rectangular sample designated for peel testing, a ≈4 mm incision was made parallel to the plane of the aortic wall to initiate delamination. The incision was made such that the delamination plane was approximately centered within the medial layer, thus separating the sample into two flaps of approximately equal thickness. Images of the sample were taken to determine its initial unloaded dimensions. There was a moderate variation in the exact location of the incision with respect to the center of the media due to sample size and cutting technique. If the delamination plane was outside the middle third of the sample thickness, the sample was discarded. Lines were drawn on the side of the sample with Verhoeffs stain in order to track the progress of failure.

The two flaps of the delaminated section of the tissue sample were then mounted in a custom gripping system with sandpaper on either side to prevent slipping and secured to a uniaxial tester. Samples were cut and mounted on a uniaxial testing

machine (MTS, Eden Prairie, MN) such that the vertical direction, as shown in Figure 5.3(c), was either axial or circumferential with respect to the vessel. The two flaps were peeled apart, causing the tissue sample to delaminate, at a constant displacement rate of 3 mm/min, and force was measured with a 5 N load cell. Preliminary tests showed no significant dependence on grip speed in the range of 1-10 mm/min, so a single velocity was used for all the subsequent experiments. Images of the side of the sample were recorded every 5 s throughout testing to capture the progression of failure. Peel tension was computed as force divided by undeformed sample width for both axially and circumferentially oriented samples.

**Shear Lap Failure** : The shear lap test (Figure 5.3(d)) produces large shear stresses in the overlap region. Rectangular samples designated for shear lap testing were specially shaped to test their shear strength. A $\approx$3.5 mm incision was made on each end of the sample centered within the medial layer and separating each end of the sample into two flaps of approximately equal thickness. The flap containing the intimal surface was removed from one end, and the flap containing the adventitial surface was removed from the other, resulting in the shear lap sample shape with an overlap length (black-dotted line in Figure 5.3(d)) of 3.0 mm. Images of the sample were taken to determine its initial unloaded dimensions. Again, there was moderate variation in incision location with respect to the center of the media due to sample size and cutting technique; therefore, if either incision surface was measured to be outside, the middle third of the sample thickness the sample was discarded. Verhoeffs stain was used to texture the side of the sample for optical displacement tracking.

The specially cut sample was then mounted in a custom gripping system with sandpaper on either side to prevent slipping and secured to a uniaxial tester (MTS, Eden Prairie, MN). The height of the grips was adjusted such that the overlap surface was along the horizontal, and an image of the sample was taken to determine its initial

unloaded dimensions. Each sample was extended to failure at a constant displacement rate of 3 mm/min, and force was measured with a 5 N load cell. During testing, digital video of the side of the sample was obtained at 24 fps, 1080p HD resolution, and spatial resolution of $\approx$ 103 pixels/mm. Image analysis and dis- placement tracking were performed per our previous studies [Raghupathy et al., 2011, Witzenburg et al., 2012].

Shear stress was computed as force divided by the undeformed overlap area (sample width multiplied by overlap length). Unlike the peel test, which has been used previously to investigate aortic tissue [Sommer et al., 2008, Pasta et al., 2012], to the best of our knowledge the shear lap test has never been used to investigate aorta or other cardiovascular soft tissues (though Gregory et al. used a similar test to investigate the shear properties of the annulus fibrosus [Gregory et al., 2011]). Therefore, displacement tracking was performed to verify that the shear lap test, as applied to the ascending thoracic aorta, produced large shear strains in the overlap region.

### 5.2.2 Statistical analysis and presentation

Unless otherwise stated, the p-values are based on unpaired two-tailed t-tests, and p-values less than 0.05 were deemed significant. Values are reported as mean $\pm$ 95% confidence interval (CI).

### 5.2.3 Model

The multiscale model employed was an extension of the previously presented model of collagen gel mechanics [Chandran et al., 2008, Hadi et al., 2012] applied recently to porcine aortic failure during in-plane tests [Shah et al., 2014]. It consisted of three scales: the FE domain at the millimeter (mm) scale, representative volume elements (RVEs) at the micrometer ($\mu$m) scale, and fibers with radii at the 100 nanometer (nm) scale. Each finite element contained eight Gauss points, and each

| Equation | Description | Scale |
|---|---|---|
| $\sigma_{ij,j} = \frac{1}{V} \oint \partial V \left(\sigma_{ij}^{L} - \sigma_{ij}\right) u_{k,j} n_k \mathrm{d}S$<br><br>$\sigma$:macroscale averaged Cauchy stress<br>$V$: RVE volume<br>$\sigma^L$: microscale stress<br>$u$: RVE boundary displacement<br>$n$: normal vector to RVE boundary | Macroscale volume-averaged stress balance | Tissue |
| $\sigma_{ij} = \frac{1}{V} \int \sigma_{ij}^{L} \mathrm{d}V = \frac{1}{V} \sum_b f_i x_j$<br><br>$b$: RVE boundary cross links<br>$x$: boundary coordinate<br>$f$: force acting on boundary | Volume-averaged RVE stress | Network |
| $F_f = \frac{EA}{\beta} \left(e^{\beta \frac{\lambda^2 - 1}{2} - 1}\right)$<br><br>$F_f$: fiber force<br>$E$: fiber stiffness<br>$A$: fiber cross-sectional area<br>$\beta$: fiber non-linearity<br>$\lambda$: fiber stretch | Fiber constitutive equation | Fiber |
| $\sigma_{ij}^{M} = \frac{G}{J} \left(B_{ij} - \delta_{ij}\right) + \frac{2G\nu}{J(1-2\nu)} \delta_{ij} ln(J)$<br><br>$\sigma^M$: matrix Cauchy stress<br>$G$: matrix shear modulus<br>$J$: deformation tensor determinant<br>$B$: left Cauchy-Green tensor<br>$\nu$: Poisson's ratio | neo-Hookean matrix constitutive equation | Tissue |

Table 5.1: Governing equations applied within the multiscale model, as well as the length scale at which each equation was applied.

Gauss point was associated with an RVE. Each RVE was comprised of a discrete fiber network in parallel with a nearly incompressible neo-Hookean component (to represent the nonfibrous material). The governing equations are given in Table 5.1. The major advance to the model was the implementation of a new tissue-specific network, specifically designed to capture the different components of the aortic wall.

The aorta is organized into thick concentric medial fibrocellular layers which can be represented by discrete structural and functional units. The lamellar unit, detailed by Clark and Glagov [Clark and Glagov, 1985], consists of an elastic lamina

sandwiched between two sheets of smooth muscle cells. The small-scale network in our computational model was designed to simulate the architecture of this discrete lamellar unit (Figure 5.4), as visualized by histological analysis. Portions of unloaded porcine ascending aorta were cut such that the transmural structure was aligned in the circumferential, i.e., horizontal, direction and fixed in 10% buffered neutral formalin solution overnight, embedded in paraffin, and prepared for histological investigation per standard techniques. Sections were stained consecutively with hematoxylin and eosin (HE) stain (Figure 5.4(a)) to visualize smooth-muscle cell nuclei, Massons trichrome stain (Figure 5.4(b)) to visualize collagen, and Verhoeffs Van Gieson stain (Figure 5.4(c)) to visualize elastin. The final network structure is shown in Figure 5.4(d), and the net- work parameters are given in Table 5.2. The volume fraction for the tissue-specific network was set to 5% per the porcine aorta volume fraction measurements of Snowhill et al. [Snowhill et al., 2004]]. The elastic lamina was represented by a 2-D sheet of elastin and collagen fibers. Collagen fibers within the elastincollagen sheet were generated such that they exhibited strong circumferential orientation, based on the known tissue structure [Clark and Glagov, 1985, Tonar et al., 2015, Snowhill et al., 2004, Timmins et al., 2010, Sokolis et al., 2008]. Histological and compositional studies show more elastin than collagen within each lamina of the ascending aortic wall. Based on the histological observations of Sokolis et al. [Sokolis et al., 2008], the overall ratio of elastin-to-collagen within the 2-D sheet was set to 1.6. Elastin fibers were generated such that orientation was approximately isotropic within the plane. The radial properties of the aorta are less well established [Dobrin, 1978, MacLean et al., 1999] but are extremely important because failure of the interlamellar connections dictates delamination and thus aortic dissection. Within the model network, the interlamellar connections were designed to encompass the combined effect of all structural components (smooth muscle cells, fine collagen fibers, and fine elastin fibers) contributing to radial strength.

| Parameter | Value | References |
|---|---|---|
| Collagen fibers | | |
| Network orientation, $[\Omega_{zz}, \Omega_{\theta\theta}, \Omega_{rr}]$ | [0.1 0.9 0] ± [0.05 0.05 0] Mean ± 95% CI | [Clark and Glagov, 1985], [Tonar et al., 2015], [Snowhill et al., 2004], [Timmins et al., 2010] |
| Fiber stiffness ($E \times A$) | 340 nN | [Lai et al., 2012] |
| Fiber non-linearity ($\beta$) | 2.5 | [Lai et al., 2012] |
| Failure stretch ($\lambda_{critical}$) | 1.42 | [Lai et al., 2012] |
| Elastin fibers | | |
| Network orientation, $[\Omega_{zz}, \Omega_{\theta\theta}, \Omega_{rr}]$ | [0.5 0.5 0] ± [0.05 0.05 0] Mean ± 95% CI | |
| Fiber stiffness ($E \times A$) | 79 nN | [Shah et al., 2014] |
| Fiber non-linearity ($\beta$) | 2.17 | [Shah et al., 2014] |
| Failure stretch ($\lambda_{critical}$) | 2.35 | [Shah et al., 2014] |
| Interlamellar connections | | |
| Network orientation, $[\Omega_{zz}, \Omega_{\theta\theta}, \Omega_{rr}]$ | [0.2 0.6 0.2] ± [0.05 0.05 0.05] Mean ± 95% CI | [Clark and Glagov, 1985], [Tonar et al., 2015], [Snowhill et al., 2004], [Timmins et al., 2010] |
| Fiber stiffness ($E \times A$) | 36.4 nN | [MacLean et al., 1999] |
| Fiber non-linearity ($\beta$) | 0.01 | [MacLean et al., 1999] |
| Failure stretch ($\lambda_{critical}$) | 2 | [MacLean et al., 1999] |
| neo-Hookean matrix | | |
| Poisson's ratio ($\nu$) | 0.49 | |
| Shear modulus ($G$) | 1.7 kPa | [Shah et al., 2014] |
| Proportions | | |
| Network volume fraction ($\phi$) | 0.05 | [Snowhill et al., 2004] [Humphrey, 1995] |
| Elastin to collagen ratio ($R$) | 8:5 | [Tonar et al., 2015] [Sokolis et al., 2008] |
| Ratio of interlamellar connections to elastic lamina fibers ($r$) | 1:1 | [Snowhill et al., 2004] |

Table 5.2: Model parameter values and sources

Smooth-muscle cells within the media exhibit preferential circumferential alignment [Clark and Glagov, 1985, Timmins et al., 2010, Dingemans et al., 2000], so interlamellar connections were aligned with circumferential preference. Since the interlamellar connections encompass the combined effect of all the structural components contributing to radial strength (smooth muscle cells, fine collagen fibers, and fine elastin fibers), it is somewhat unclear how to define the proportion of interlamellar connections-to-elastic lamina fibers. Snowhill et al. [Snowhill et al., 2004] determined the volume ratio of collagen to smooth muscle to be 1:1 in porcine vessels. While clearly the interlamellar connections encompass some collagen, and the elastic lamina contains large amounts of elastin, we utilized this 1:1 ratio.

Initial estimates of the fiber parameters (fiber stiffness, nonlinearity, and failure stretch) for collagen and elastin were based on our previous works [Shah et al., 2014, Lai et al., 2012], and those for the interlamellar connections were specified based on MacLeans experimental stressstrain behavior of the upper thoracic aorta subjected to radial failure [MacLean et al., 1999]. Properties were subsequently adjusted such that a single set of model parameters matched results from the suite of experiments performed herein; the final parameter values are given in Table 5.2.

In addition to the smooth-muscle cells and connective tissue present within the lamellar unit, there is also fluid, primarily extracellular water [Humphrey, 1995], that combines with the smooth-muscle cells cytoplasm to make tissue deformation nearly isochoric. A nonfibrous, neo-Hookean matrix was added to the network to make it nearly incompressible ($\nu = 0.49$). The fiber network and nonfibrous matrix operated as functionally independent until failure, at which point network failure dictated simultaneous matrix failure. Stresses developed by the new tissue-specific network and matrix were treated as additive, as in other constrained mixture modelsciteHumphrey2003, Alford2008, Alford2008a, Gleason2004. The matrix material was considered homogeneous throughout the global sample geometry; each element,

however, was assigned a unique set of fiber networks. New networks were generated for each of the five model simulation replicates for the uniaxial test; the uniaxial simulations showed almost no variability in repeated runs (SD $< 1\%$ of value), so no replicates were performed for the other tests.

Macroscale and microscale stress and strain were coupled as described previously [Chandran et al., 2008, Stylianopoulos and Barocas, 2007]. Briefly, displacements applied to the macroscale model were passed down to the individual RVEs. The tissue-specific network within the RVE responded by stretching and rotating, generating net forces on the RVE boundary. A volume-averaged stress was determined for each Gauss point within the element from the net forces on the network boundary and the nonfibrous resistance to volumetric deformation. The macroscopic displacement field was updated until the global Cauchy stress balance was satisfied. Grip boundaries were enforced using rigid boundary conditions and the remaining sample surfaces were stress-free. All model simulations were run using 256-core parallel processors at the Minnesota Supercomputing Institute, Minneapolis, MN; clock times averaged 10 h per simulation.

Finally, we ran a brief simulation of uniaxial extension in the radial direction to compare with the experimental results of MacLean et al. [MacLean et al., 1999], who performed uniaxial extension to failure of porcine aorta samples in the radial direction as noted earlier. The MacLean study represented an important test for our approach since the experiments were performed on the same tissue (healthy porcine thoracic ascending aorta) but in a mode that we did not use to generate and fit the model (radial extension to failure). Although MacLean did not report the tensile stress at failure, they reported the average tangent modulus at failure as well as the status of different samples at specific values of stretch; these data provided a basis for comparison with the model.

## 5.3 Results

Experiments were performed in four different geometries: uniaxial, biaxial, peel, and lap. In the uniaxial, peel, and lap tests, samples were prepared and pulled in two different directions, with some samples being tested in the axial direction and others in the circumferential direction. The multiscale model was used to describe all of the different experiments; the same set of model parameters was used for all of the experiments, including both prefailure and failure behavior.

### 5.3.1 Uniaxial extension to failure

Uniaxial samples (Figure 5.5(a)) aligned both circumferentially (n = 11) and axially (n = 11) were loaded to failure. In Figure 5.5(b), the first Piola-Kirchhoff (PK1) stress, defined as the grip force divided by the undeformed crosssectional area of the neck of the dogbone, was plotted as a function of grip stretch along with the best-fit tissue-specific model curves for samples aligned circumferentially and axially, respectively. The specified and regressed model parameters of Table 5.2 allowed the model to match the experimental prefailure and failure results to within the 95% confidence intervals for both orientations, matching the roughly threefold difference in failure stress (2510 ± 979 kPa for samples aligned circumferentially as compared to 753 ± 228 kPa for those aligned axially) and similar to stretch to failure (1.99 ± 0.07 for samples aligned circumferentially as compared to 1.91 ± 0.16 for those aligned axially) in the circumferential case vis-á-vis the longitudinal case. The neck region of the simulated uniaxial samples (both circumferential and axial) experienced the largest stresses (as expected) and also a large degree of fiber reorientation, as can be seen in Figure 5.5(b). For the simulated experiments oriented circumferentially, the collagen fibers, which were already preferentially aligned in the circumferential direction, became more strongly aligned and were stretched, leading to the relatively

high stresses observed. In contrast, for the simulated experiments oriented axially, the collagen fibers tended to pull apart by stretching the surrounding elastin, leading to a significantly lower stress and more failure of the elastin fibers. In both simulations, the collagen fibers were most likely to fail due to the extremely large extensibility of the elastin fibers, but the tendency of the collagen fibers to break was much higher in the circumferentially aligned simulated experiments (Figure 5.5(c)). This shift is attributed to the collagen fibers being aligned in the direction of the pull and thus being forced to stretch more during circumferential extension, whereas there is more elastin and interlamellar connection stretch in the axial extension.

### 5.3.2 Equibiaxial extension

The averaged experimental PK1 stress was plotted as a function of grip stretch (n = 9; also used in our previous analysis [Shah et al., 2014]) along with the best-fit tissue-specific model curves in Figure 5.6(a). The equibiaxial extension test was not performed to failure but instead was stopped at a stretch of 1.4 to ensure that the sample did not fail during testing (based on initial experiments to estimate the safe stretch limit). Thus, the peak circumferential (139 $\pm$ 43 kPa) and axial (102 $\pm$ 30 kPa) stresses were not failure stresses. The equibiaxial model results (lines) were in good agreement with the experiments in both directions but slightly overpredicted the degree of anisotropy, i.e., the separation between the two lines. In particular, stresses in the circumferential direction were slightly overpredicted but remained within the 95% confidence interval for the experiment. The arms of the sample showed behavior similar to the uniaxial experiments, as can be seen in the stress plots of Figure 5.6(b), but our primary interest is in the central region that was stretched equibiaxially. As expected for equibiaxial extension, in-plane fiber orientation of the elements in this region showed little change (Figure 5.6(c)); there was, however, a deviation from affinity because the stiffer collagen fibers did not stretch nearly as much as the more

compliant elastin fibers. At the final stretch step, for example, the collagen fibers were extended to an average of 13% stretch, but the elastin fibers had an average of 118% stretch.

### 5.3.3 Peel to failure

Peel samples from both the circumferential (n = 13) and axial (n = 23) orientations were loaded to failure. Peel tension, defined as the grip force divided by the sample width, was used to quantify delamination strength. When plotted as a function of grip displacement, the peel tension rose to an initial peak and then plateaued until total sample failure (Figure 5.7(a)); importantly, the rise in each individual experiment was quite steep, but since the rise occurred at different grip stretches in different experiments (because of variation in sample size and initial notch depth), the average data of Figure 5.7(a) appear to rise smoothly. The simulation results were thus similar to individual experiments, but we did not introduce the sample-to-sample variation necessary to smooth out initial rise.

The initial point and end point of the plateau region were computed by splining the data into 20 sections and determining where the slope of a linear fit of the points in a section was not significantly different from zero. The value of peel tension in the plateau region was averaged in order to determine the peel strength of each sample. The standard deviation of peel tension within the plateau region was evaluated to assess the degree of fluctuation during the peeling process. The average peel tension was significantly higher ($p < 0.01$) for samples aligned axially versus circumferentially ($97.0 \pm 12.7$ versus $68.8 \pm 14.2$ mN/mm, respectively) with an anisotropy ratio of 1.4, similar to the results reported by others [29,30]. The standard deviation of peel tension showed similar anisotropy ($p < 0.001$) for samples aligned axially versus circumferentially ($12.66 \pm 2.22$ versus $5.78 \pm 1.04$ mN/mm, respectively). The anisotropic response was present even when the standard deviation was normalized by

average peel tension ($p < 0.05$, $0.145 \pm 0.037$ versus $0.088 \pm 0.017$, respectively, for a ratio of 1.65). Simulation results showed similar but less pronounced anisotropy (80.35 versus 67.01 mN/mm, ratio = 1.20). For both the circumferentially and axially oriented simulated experiments, the first Piola-Kirchhoff stress was concentrated around the peel front (Figure 5.7(b)), and there was extensive stretching of the interlamellar connections. In sharp contrast to the simulated uniaxial failure experiments (Figure 5.5), the vast majority of failed fibers in the simulated peel failure experiments were interlamellar connections; this result highlights the need for a detailed anisotropic model because different physiologically relevant loading configurations impose very different mechanical demands on the tissues components.

Regional analysis was performed to determine whether sample location, i.e., location along the aortic arch, had an effect on mean average or mean standard deviation of peel tension. First, samples, taken from both the axial and circumferential directions from multiple specimens, were grouped according to their distance from the inner and outer curvature of the aortic arch. No significant difference (all the p-values $> 0.10$, $n > 4$ for all groups) was observed. Then, axially oriented samples taken from a single specimen were grouped by where peel failure was initiated (proximal or distal to the heart, $n = 4$ for both groups). No significant difference was seen in mean average peel tension (paired t-test, p-value = 0.26) or mean standard deviation of peel tension (p-value = 0.84) between the two groups. Pairing was done based on sample location within the specimen.

### 5.3.4 Shear lap failure

As expected, the displacements were primarily in the pull direction, and shear strain was largest in the overlap region (Figs. 5.8(a) and 5.8(b)). In order to investigate the strain behavior of the tissue more fully, a line was drawn at the edge of the overlap surface, and strains tangential and normal to the overlap edge were calculated (n

= 15 and n = 19 for axial and circumferential samples, respectively; some samples were not analyzed due to poor speckling). The maximum strain in each direction was determined (Figs. 5.8(c) and 5.8(d)). For both the axially and circumferentially aligned samples, the shear strain, $E_{nt}$, was large in the overlap region, as desired. For the axially oriented samples, the shear strain was higher than both the normal ($p < 0.1$) and tangential strains ($p < 0.01$). For the circumferentially oriented samples it was significantly higher than the tangential strain ($p < 0.05$) and comparable to the normal strain ($p = 0.26$).

Shear lap samples from both the circumferential (n = 28) and axial (n = 26) orientations were loaded to failure. The nominal (average first Piola-Kirchhoff) shear stress, the force per overlap area (Figure 5.9(a)), exhibited catastrophic failure similar to that seen in the uniaxial tests and unlike the steady failure of a peel test. Circumferentially oriented samples exhibited significantly higher ($p = 0.013$) peak shear stresses than axially aligned samples ($185.4 \pm 28.4$ versus $143.7 \pm 16.0$ kPa, respectively). In both the axial and circumferential directions, the shear lap failure stress was less than 20% of the failure stress necessary for uniaxial failure, indicating that the tissue is far weaker in shear than in uniaxial tension. The grip strain at failure was used to quantify further the compliance of the tissue. Greater grip strain ($p = 0.07$) was necessary to fail samples aligned in the axial direction compared with those in the circumferential direction ($1.63 \pm 0.16$ versus $1.43 \pm 0.17$, respectively). As can be seen in Figure 5.9(a), the multiscale model predicted the shear lap behavior of circumferentially oriented samples well (within the 95% CI). It was less successful at predicting the shear lap behavior of axially oriented samples (below the 95% CI), thus overestimating tissue anisotropy. The overlap region edges of the simulated uniaxial samples (both circumferential and axial) experienced the largest stresses and also the largest degree of fiber reorientation (Figure 5.9(b)). Interlamellar fibers within the lap region were rotated and stretched strongly by the shearing; the collagen and elastin

fibers were stretched more than in the peel test but considerably less than in the uniaxial and biaxial tests. As a result (Figure 5.9(c)), the distribution of failed fibers was split more between the different fiber types than during peel or uniaxial failure. Even though the interlamellar connections, being much weaker than the others, were the most common to fail, there was also significant damage to the collagen and elastin fibers, perhaps due to the tangential component of the strain during the test (Figure 5.8(d)).

### 5.3.5 Summary comparison of model and experiment

Since a stated goal of this work was construct a multiscale model of aortic tissue mechanics that predicts failure in many different physiologically relevant loading modalities, we present a brief summary of the experimental and model failure results. Figure 5.10 shows the failure PK1 stress in uniaxial tests, failure tension in peel tests, and failure shear stress in shear lap tests for both the experiments and simulations for samples aligned in both the circumferential and axial directions. A single model with one set of parameters matches all of the experimental results well. It captures both the anisotropy exhibited in the different tests as well as the magnitude of stress or tension. In particular, the model predicts the considerably lower tissue strength observed in shear lap tests than that seen in uniaxial extension.

### 5.3.6 Uniaxial extension to failure in the radial direction

MacLean et al. [MacLean et al., 1999] reported that the average tangent modulus before failure was 61.4 $\pm$ 43 kPa. For our simulations, we found that the tangent modulus before failure was 58 kPa, in obvious good agreement with MacLeans experimental result. The stretch ratio at failure in the model was 3.1, and MacLean reported that there was noticeable elastin layer separation at a stretch ratio of 2, and that a stretch ratio of 3.5 was past the value at which the wall can maintain stress.

Although the report of MacLean is obviously vague, the model results all appear to be consistent with MacLeans observations. The ability to make a reasonable prediction of an experiment performed using loading modality different from those used in the creation and specification of the model is a necessary feature for broader application in the future.

## 5.4 Discussion

Two important results came from the current work. First, a more complete picture of the failure behavior of aortic tissue was generated, demonstrating and quantifying the pronounced difference between the relatively high tissue strength in the lamellar plane (longitudinal and especially circumferential directions) and the low strength of the interlamellar connections (radial direction, demonstrated by peel and lap tests). Second, a novel multiscale, microstructural model was presented that, with proper adjustment of the model parameters, was able to reproduce the wide range of experimental observations accurately. This section focuses first on the experiments and then on the model, addressing them in the context of previous work by ourselves and others.

The current study used two novel test methods, the peel test and the shear lap test, to measure material failure in radial tension and transmural shear, respectively. The peel test is relatively new but has been used by others [Sommer et al., 2008, Tong et al., 2011, Pasta et al., 2012], and our results are consistent with their findings in terms of peel tension as well as the observation that the anisotropy typically expected of arteries in in-plane tests (higher circumferential versus axial stiffness) is reversed in peeling. Sommer et al. [Sommer et al., 2008] suggested that the anisotropic behavior may be a protective mechanism since dissection in the axial direction is often associated with failure across elastic laminae, whereas dissection in the circumferential

direction typically prop- agates between adjacent laminae. Pal et al. [Pal et al., 2014] suggested based on histology of peeled samples that the anisotropy may be due to stitching of the fibers, with failure in circumferential peeling occurring via a pull-out mechanism, whereas failure in axial peeling occurs via a tearing mechanism. This interesting conceptual description cannot be captured in our current model but clearly merits further investigation.

Although the shear lap test has been used on annulus fibrosus [Gregory et al., 2011], to the best of our knowledge it has not been applied to cardiovascular soft tissues. The loading curve for the shear lap test of ascending aorta showed catastrophic failure similar to that of a uniaxial test rather than the sliding behavior seen by Gregory et al., perhaps attributable to differences in the structure and properties between the annulus fibrosus and the ascending aorta. The failure behavior observed for the shear lap test retained the typical anisotropy expected of arteries, but required a much lower stress than that of uniaxial failure, presumably because the failure did not require as much breaking of collagen and elastin fibers. The shear lap and peel test results directly test the connections between lamellar units, and they are therefore critical in the case of a dissecting ascending aortic aneurysm. As our community moves forward to more patient-based geometries and simulations involving realistic geometries that necessarily lead to complex stress fields, validation of models in multidimensional loading is crucial. For example, it is common [Wisneski et al., 2014, Krishnan et al., 2015, Trabelsi et al., 2015, Martin et al., 2015, Martufi et al., 2014] to report results in terms of principal stresses, which are informative but do not address the fact that a stress acting radially or in shear is more likely to lead to tissue failure than one acting circumferentially. Martin et al. [Martin et al., 2015] used a potentially generalizable energy-based failure threshold, but they based the failure criterion on uniaxial circumferential tests. Although Martins work represents a significant advance and demonstrates the potential of the patient-specific

FE approach, there is clear need for a more accurate failure model, which could be informed by the current work. Another major challenge is that the tissue properties surely change during aneurysm formation, growth, and remodeling. The current work used only healthy porcine tissue, so our results are useful in guiding thought but should not be considered representative of human aneurysm tissue. There is also great need to develop better tools to estimate tissue mechanical properties in vivo, which would allow the construction of patient-specific constitutive models to match the patient-specific geometries currently in use.

Another goal of this study was to generate a tissue-specific microstructural description based on the layered structure of the aorta. Such a description, when incorporated into our multiscale modeling framework, could replicate mechanical behavior of arteries in lamellar tension, radial tension, and transmural shear, thereby linking microscale failure to the macroscale response. The simplified microstructural organization of our previous work [Shah et al., 2014] was replaced with a new lamellar model to capture the microstructure more faithfully. The lamellas structure is an essential component in modeling dissection of ATAA since radial and shear loading involve failure of the interlamellar connections rather than the lamina itself. The microstructure design of Figure 5.4 mimics the lamellar unit, detailed by Clark and Glagov [Clark and Glagov, 1985], and visualized here histologically. The unit is represented by a 2-D sheet of elastin and collagen fibers (which forms an elastic lamina) attached radially by interlamellar connections (which collectively encompass smooth-muscle cells and fine elastin and collagen fibers). Network parameters were selected to reflect the biological roles of each component and were adjusted to match the experimental results. This approach was successful in matching a wide range of tissue mechanical tests, including one – radial extension to failure – that was not used during the fitting process, and it has the potential to be extended to the more disorganized (and thus more complex) architecture of the aneurysm, especially as better imaging and image-based

modeling methods emerge [Koch et al., 2014, Tsamis et al., 2013]. The work of Pal et al. [Pal et al., 2014] represents an excellent example of this approach, developing a theoretical model of peel failure based on known structure. Pals approach could be extended to a more general stress field using a strategy similar to ours. Finally, it is important to note that abnormal loading and damage can change tissue structure. For example, Todorovich-Hunter et al. [Todorovich-Hunter et al., 1988] observed the formation of islands of elastin within the pulmonary arteries of rats in which they induced pulmonary hypertension. Thus, moving forward imaging-based alterations to the network design may be necessary to capture the structure of a damaged or diseased aorta.

There are, of course, further opportunities to construct a more realistic micromechanical model of the healthy and the aneurysmal ascending thoracic aorta. As already noted, the work of Pal et al. [Pal et al., 2014] provides a different and intriguing view of interlamellar failure by tearing versus pull-out effects. Additionally, our current model used collagen orientation tensor with eigenvalues of 0.9 and 1.0, corresponding roughly to collagen aligned within 18° of the circumferential axis ($\sin^2(18°) = 0.1$). That number was based on the observed circumferential alignment of collagen fibers in the vessel wall but is an estimate and could be modified to provide a better match to the experimental data. In fact, the collagen and elastin fiber orientations within the $z\theta$ plane could also be treated as fitting parameters, which would likely improve the model fit, but we chose to use the best estimate from structural data rather than introduce further flexibility to an already highly parameterized model. Finally, the Fung-type model of fiber mechanics (Table 5.1, Equation (3)) could be replaced with a recruitment model, e.g., [Zulliger et al., 2004], which would provide an alternative mechanism to capture the nonlinear behavior associated with fiber waviness [Haskett et al., 2012] and might provide a better fit of the experimental data. All of these modifications are possible and could be implemented as

additional data emerge about the arrangement and properties of the components of the arterial wall.

In summary, a microstructurally based multiscale model of prefailure and failure behaviors was able to match the experimentally measured properties of the healthy porcine ascending aorta in four different loading configurations and two different directions, and it was successful when applied to experiments in the literature that were not used during the fitting and specification project. This model could provide new insight into the failure mechanisms involved in aortic dissection and could be incorporated into patient-specific anatomical models, especially if model parameters associated with specific patients or patient groups can be obtained.

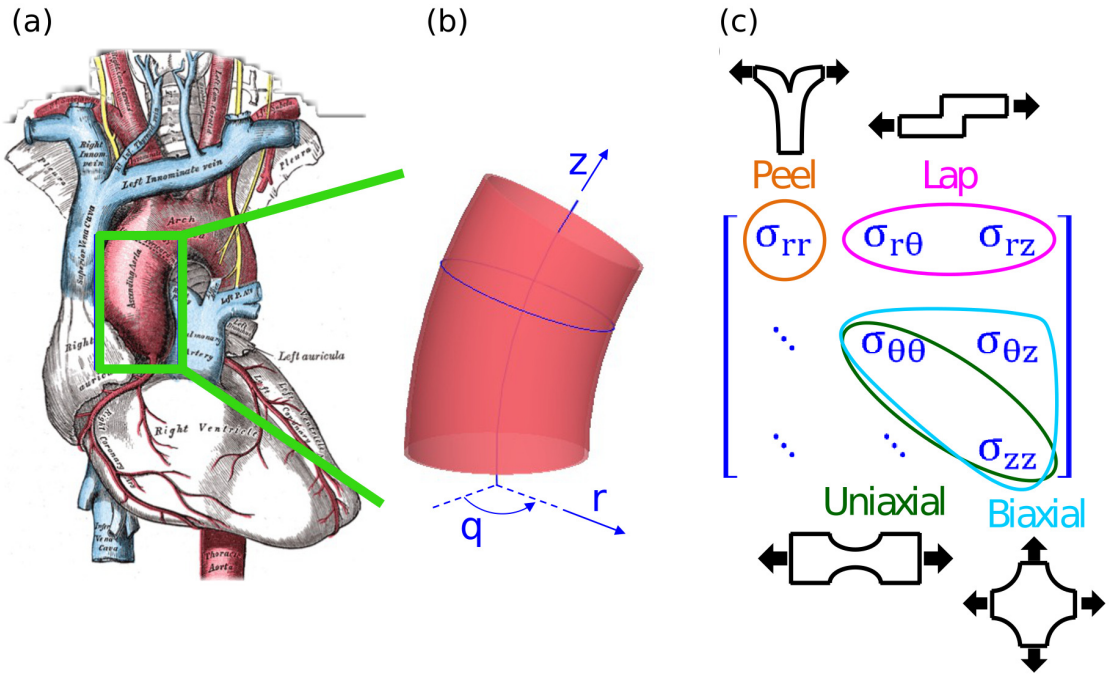


Figure 5.1: The ascending thoracic aorta. (a) Illustration of the heart with the ascending aorta highlighted [Gray et al., 2000], (b) Geometry and coordinate system describing the ascending aorta, and (c) The three-dimensional stress tensor for the aorta, marked to show how different testing modes were used to target specific stress components.

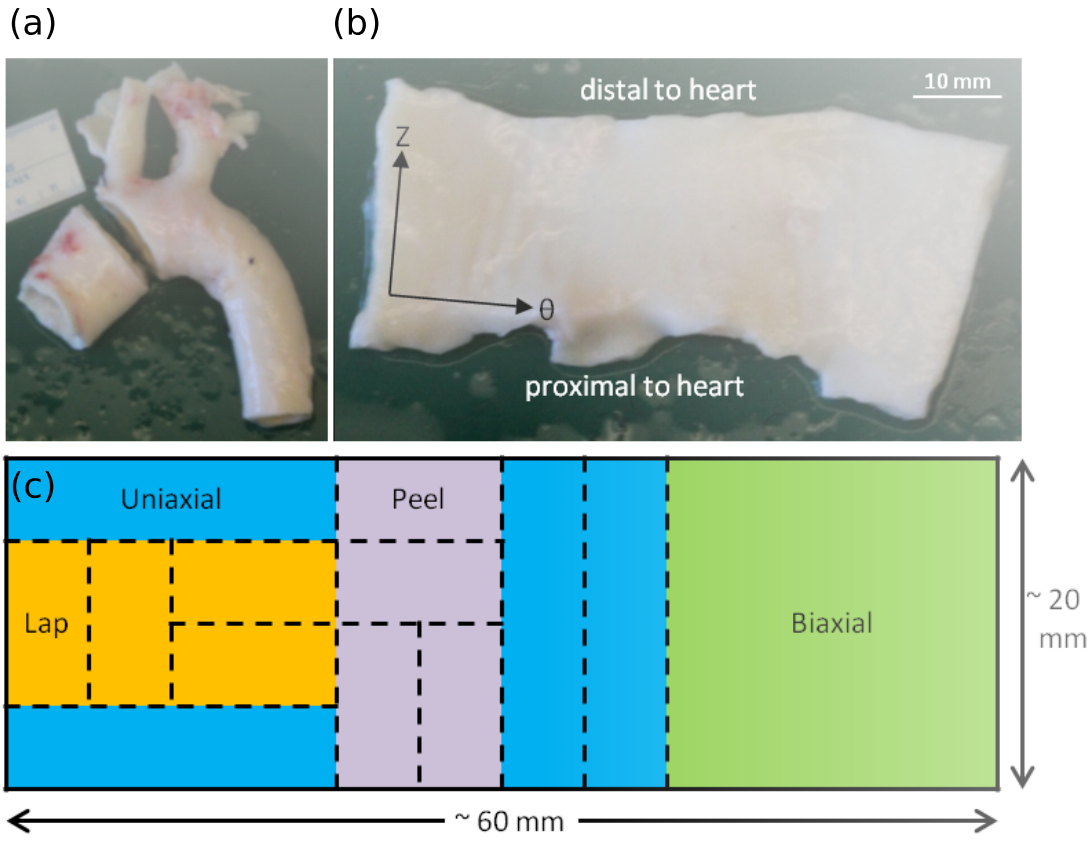


Figure 5.2: Specimen dissection. (a) Porcine aortic arch with ascending aortic ring removed. The white star represents a marker used to keep track of tissue sample orientation. (b) The ring was cut open along its superior edge and laid flat with the intimal surface up and the axial, Z, and circumferential, $\theta$, directions along the vertical and horizontal directions, respectively. Axial and circumferential directions are shown with black arrows. (c) Schematic showing a typical sectioning and testing plan for an ascending aortic specimen.

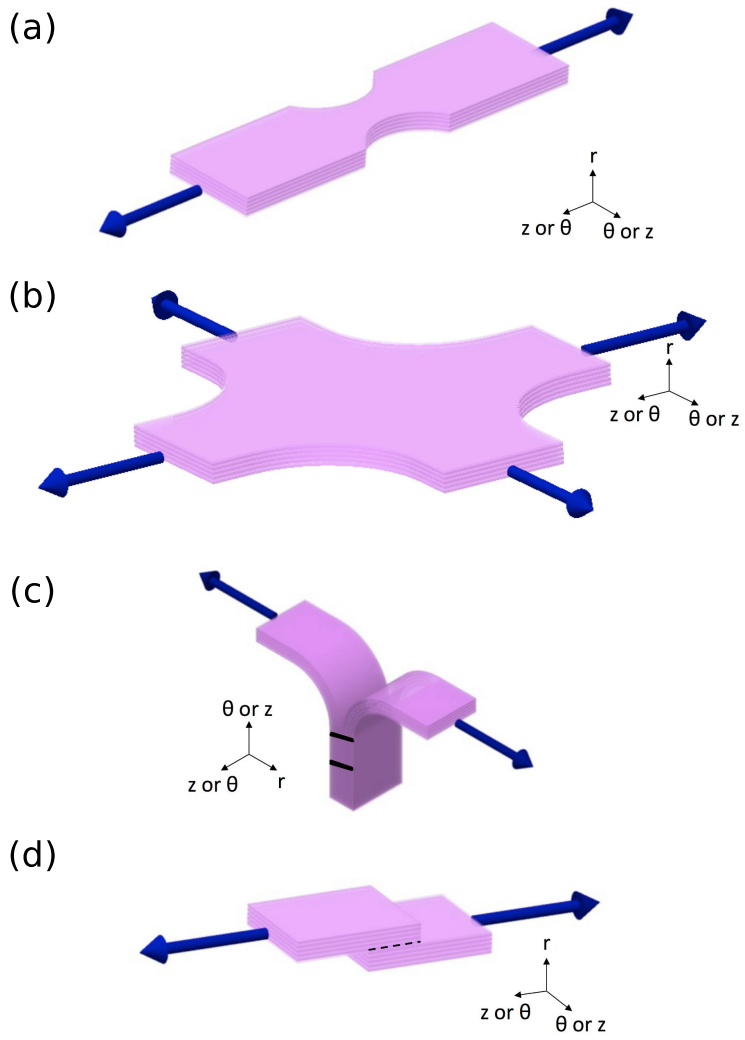


Figure 5.3: Schematics of all mechanical tests. (a) Uniaxial test: samples were cut and mounted such that the direction of pull corresponded with either the axial or circumferential orientation of the vessel. (b) Equibiaxial test: samples were cut and mounted such that the directions of pull corresponded with the axial and circumferential orientations of the vessel. (c) Peel test: samples were cut and mounted such that the vertical direction corresponded with either the axial or circumferential orientation of the vessel. (d) Lap test: samples were cut and mounted such that the direction of pull corresponded with either the axial or circumferential orientation of the vessel; dotted black line indicates overlap length.

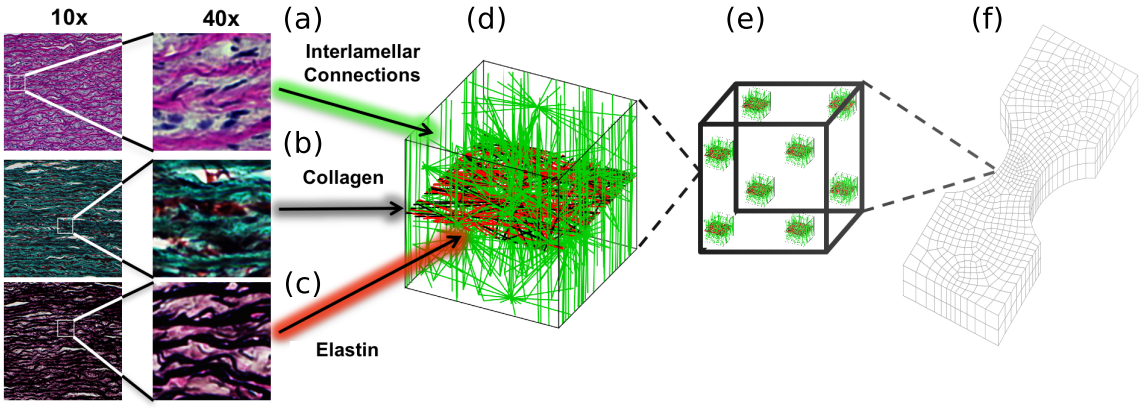


Figure 5.4: Multiscale model based on aortic media structure. (a) Hematoxylin and eosin stain shows smooth muscle cell nuclei (dark purple) and elastic lamina (pink). (b) Massons trichrome stain shows collagen (blue) within the lamina and smooth muscle (red). (c) VerhoeffVan Gieson shows elastin (black/purple). (d) A microstructural model based on the histology contains a layer of elastin (red) reinforced by collagen fibers (black). The collagen fibers are aligned preferentially in the circumferential direction, and the elastin sheet is isotropic. Lamellae are connected by interlamellar connections (green) representing the combined contribution of fibrillin and smooth muscle. The interlamellar connections are aligned primarily in the radial direction but also have some preference for circumferential alignment to match smooth muscle alignment *in vivo*. (e) An RVE with eight gauss points. (f) FE geometry showing a uniaxial shaped sample (equibiaxial, lap, and peel geometries were also used).

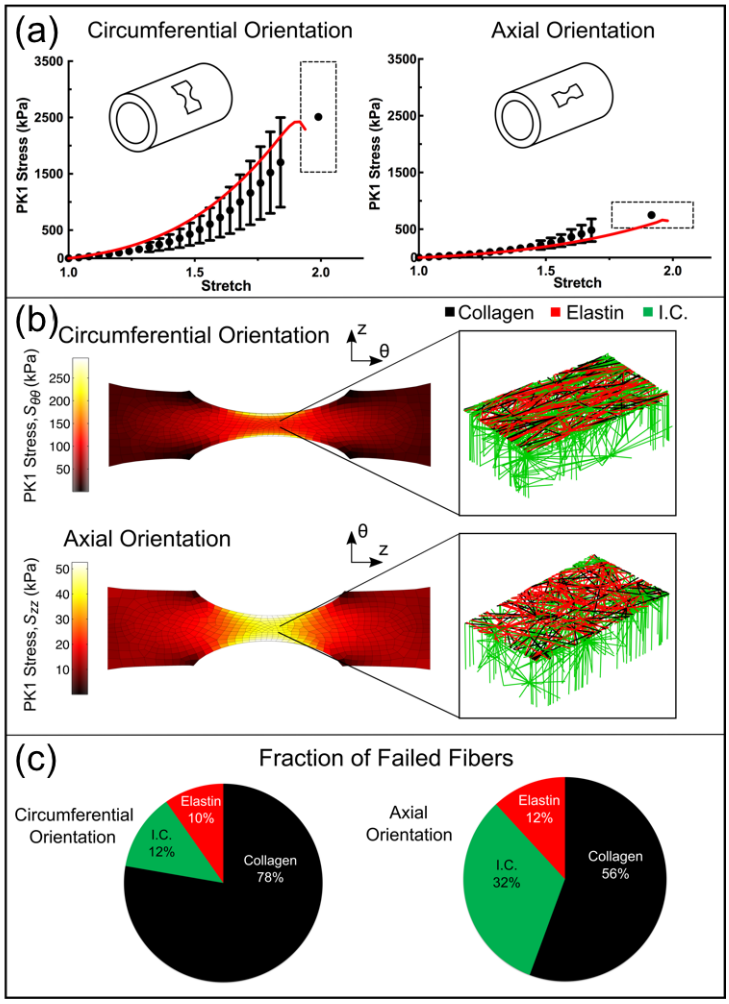


Figure 5.5: Uniaxial extension to failure. (a) First Piola-Kirchhoff (PK1) stress versus grip stretch for circumferentially (n = 11) and axially (n = 11) orientated samples (dots, mean ± 95% CI). Error bars are only shown for stretch levels up to the point at which the first sample failed. The final dot shows the average stretch and stress at tissue failure, and the dashed rectangle indicates the 95% confidence intervals of stretch and stress at failure. The red lines show the model results for PK1 stress as a function of grip stretch. (b) PK1 stress distributions along the axis of applied deformation for both the circumferentially ($S_{\theta\theta}$) and axially ($S_{zz}$) aligned simulations, accompanied by an enlarged view of a network with the upper interlamellar connections removed to make the collagen and elastin visible. (c) Fraction of failed fibers of each type in the simulated experiment. Because the collagen fibers are preferentially aligned in the circumferential direction, more of the failed fibers were collagen for the circumferentially aligned simulation, whereas for the axially aligned simulation more of the failed fibers were interlamellar connections (I.C. = interlamellar connections).

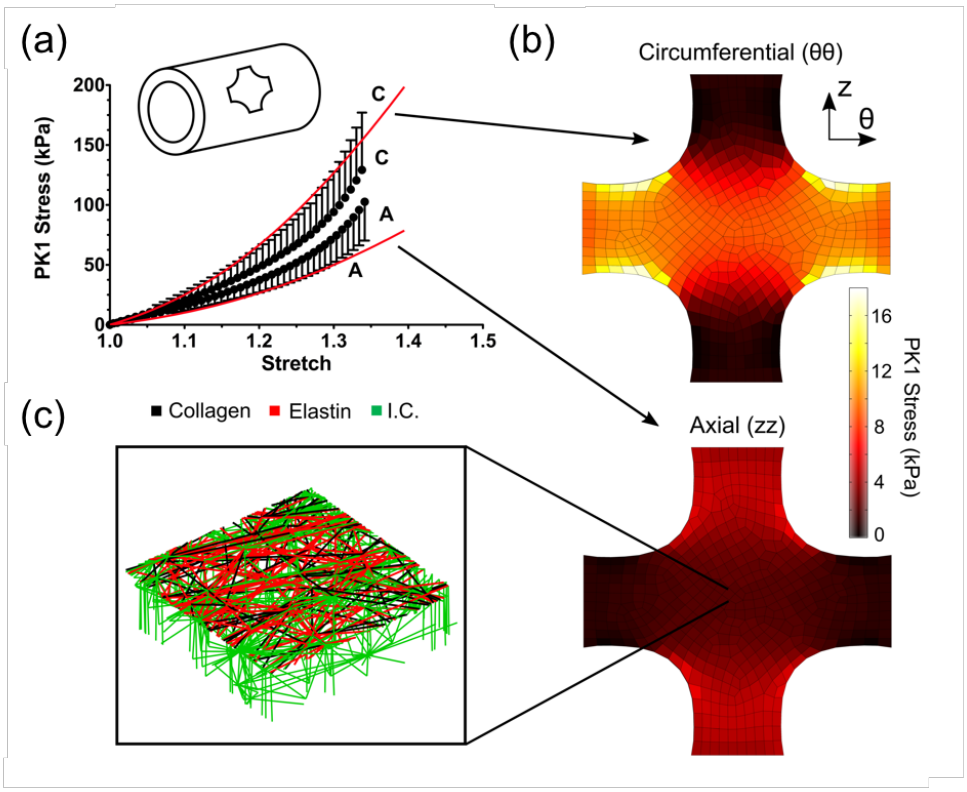


Figure 5.6: Equibiaxial extension. (a) Mean PK1 stress as a function of grip stretch (dots) for equibiaxial extension. The 95% CI was 3035% of the measured value but was omitted from the figure to improve visual clarity. The red lines show the model results for PK1 stress versus grip stretch. (b) Circumferential ($S_{\theta\theta}$) and axial ($S_{zz}$) PK1 stress distributions predicted by the model. (c) Enlarged view of a micronetwork with the upper interlamellar connections removed to make the collagen and elastin visible.

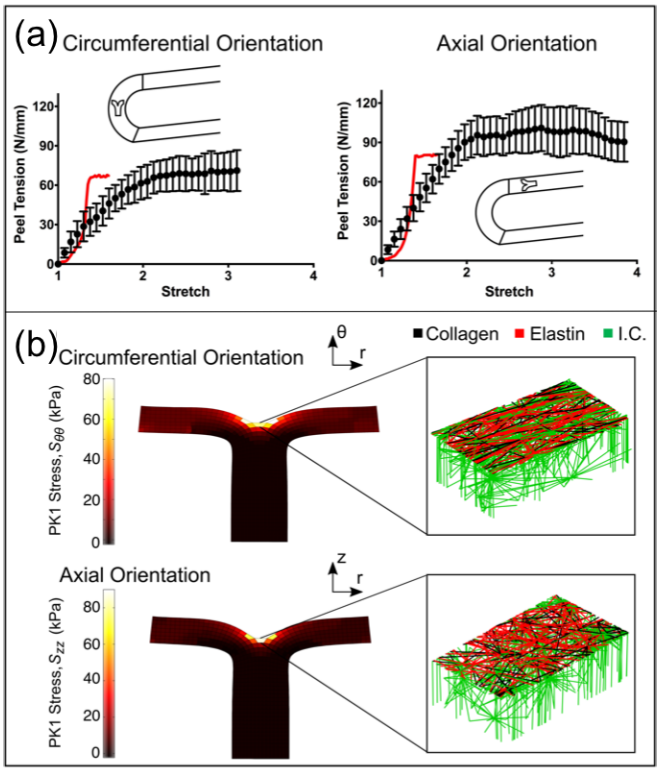


Figure 5.7: Peel to failure. (a) Peel tension versus grip stretch for both circumferentially and axially oriented samples (dots, mean ± 95% CI). The red lines indicate the model results. (b) PK1 stress ($S_{rr}$) distributions along the axis of applied deformation for both the circumferentially and axially aligned simulations, accompanied by an enlarged view of a network with the upper interlamellar connections removed to make the collagen and elastin visible.

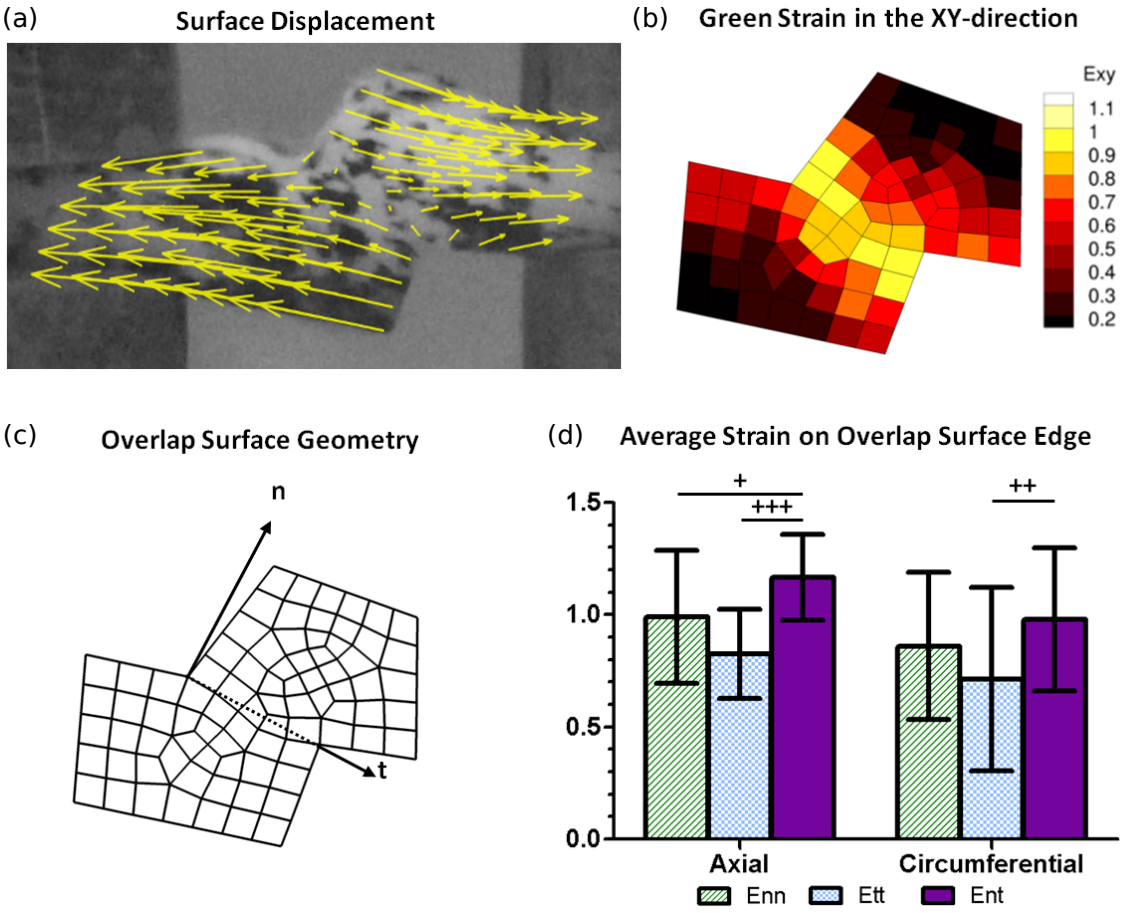


Figure 5.8: Kinematics of the shear lap test. (a) Displacement of a representative shear lap sample, adjusted to zero displacement at the center. (b) Strain of the representative sample in the XY-direction. (c) Dotted line showing overlap surface edge and vectors with normal and tangential directions. (d) Average strain on the overlap surface edge for both axially (n = 15) and circumferentially (n = 19) oriented samples. Error bars indicate 95% confidence intervals. $^{+}p < 0.10$, $^{++}p < 0.05$, and $^{+++}p < 0.01$.

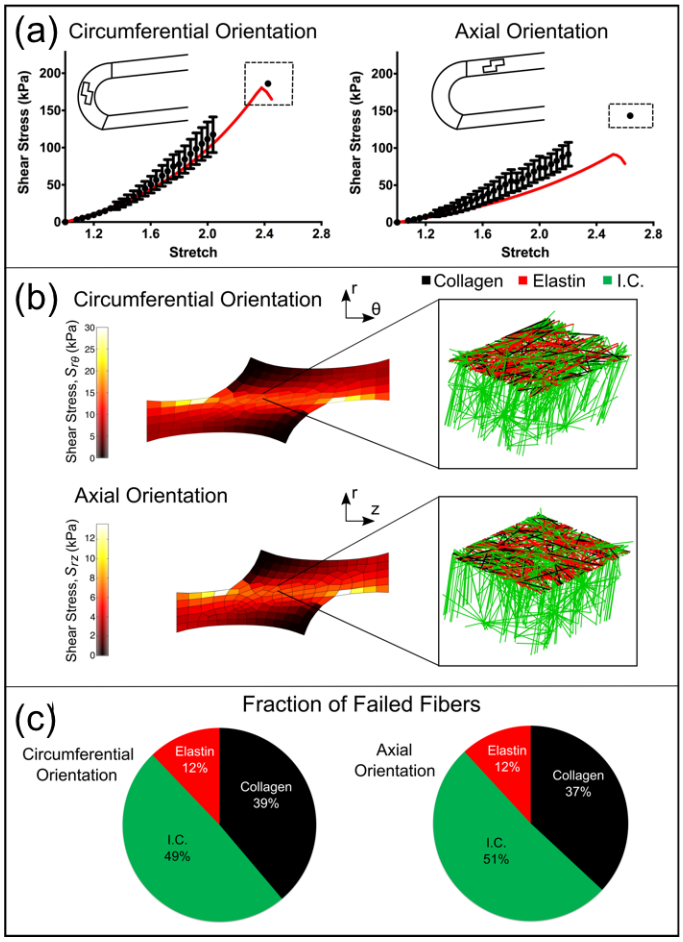


Figure 5.9: Shear lap failure. (a) PK1 stress versus grip stretch for circumferentially (n = 28) and axially (n = 26) orientated samples (dots, mean ± 95% CI). Error bars are only shown for stretch levels up to the point at which the first sample failed. The final dot shows the average stretch and stress at tissue failure and the dashed rectangle indicates the 95% confidence intervals of stretch and stress at failure. The red lines show the model results. (b) Shear stress distributions along the axis of applied deformation for both the circumferentially ($S_{r\theta}$) and axially ($S_{rz}$) aligned simulations, accompanied by an enlarged view of a network with the upper interlamellar connections removed to make the collagen and elastin visible. (c) Fraction of failed fibers of each type in the simulated experiment (I.C. = interlamellar connections).

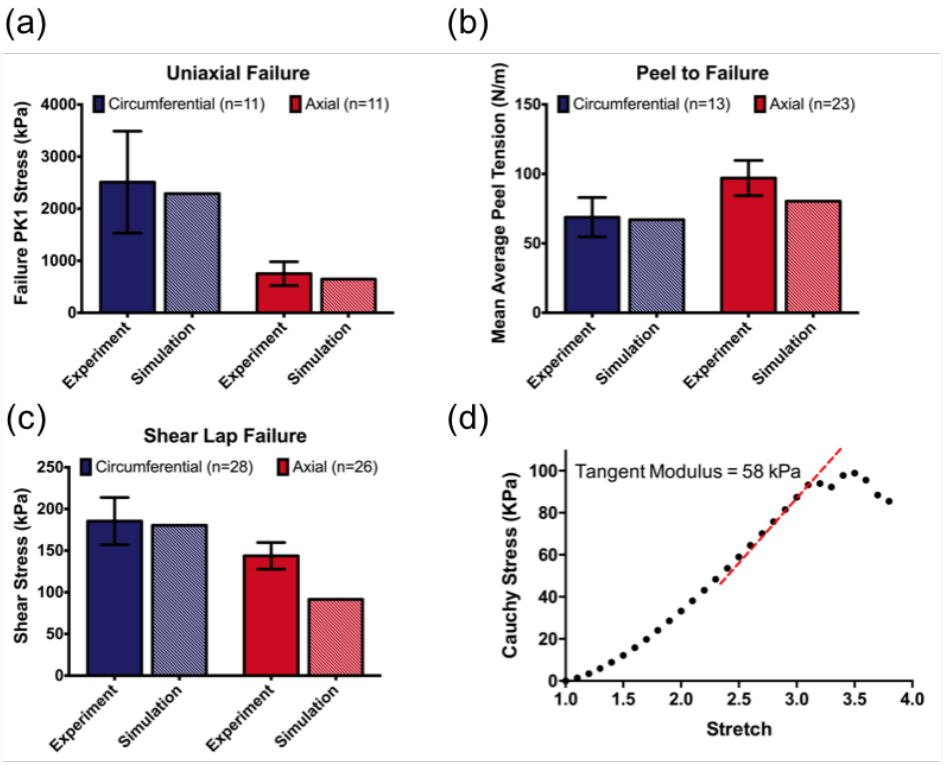


Figure 5.10: Summary of experimental and model results. (a) Experimental and model failure PK1 stress ($S_{\theta\theta}$ and $S_{zz}$) in uniaxial tension tests for samples oriented circumferentially and axially. (b) Experimental and model failure tension in peel tests for samples oriented circumferentially and axially. (c) Experimental and model failure shear stress ($S_{r\theta}$ and $S_{rz}$) in shear lap tests for samples oriented circumferentially and axially. All the experimental data show mean $\pm$ 95% CI. (d) The model showed failure at a stretch ratio of 3.1 with a tangent modulus of 58 kPa in the region prior to failure, comparing well to MacLeans [MacLean et al., 1999] reported tangent modulus of 61 kPa.

# Chapter 6

# Conclusions and Future Work

## 6.1 Summary

The research studies presented in the chapters of this dissertation help frame an understanding of the microscopic mechanisms affecting the mechanical properties of native and engineered soft tissues.

Using discrete fiber networks of linear viscoelastic members, we showed in Chapter 2 the presence of evolving time scales in the relaxation spectrum of the network that arise from its heterogeneous structure and the non-affine deformations occurring within it. For a 3-D network composed of only fibers with two different characteristic relaxation times, the instantaneous relaxation time of the system evolved over time and showed a highly non-linear behavior. The relaxation spectrum for such a network showed multiple peaks, and it was very similar to that obtained for reconstituted collagen gels, suggesting that some of the relaxation time scales observed in the viscoelastic spectra of collagenous tissues might be purely structure-based, arising from their inherent network arrangement.

In Chapter 3, we used fiber-level failure rules to compute the fatigue behavior of the whole network. We observed that, for reasonable magnitudes of loads, an

irregular fiber network structure can undergo more loading cycles than a single fiber or a regular fiber lattice. The network geometry enables an uneven distribution of stresses within the network fibers, with some fibers bearing higher loads than others. This nonuniform stress distribution leads to a gradual progression of fatigue within the network resulting in the network structure outlasting the individual fiber. Furthermore, a comparison of the fatigue failure behavior of networks having the same fiber mechanical properties but different network topologies suggested that geometric interactions between the fibers also affects the failure properties of the network. We simulated the fatigue behavior of three different network geometries — Delaunay, Voronoi, and Erdős-Rényi. The Delaunay network geometry showed the best low-stress, high-cycle behavior, so a Delaunay architecture might be preferable for fibrous structures undergoing repeated low to moderate loads.

Finally, in Chapters 4 and 5, we used a multiscale approach to highlight the effect of microscale network behavior and structure on the macroscale mechanics of tissues. We used networks of contracting fibers to simulate actin-myosin kinetics in the cell cytoskeleton (Chapter 4). This model of cell contraction was applied to study contracting cells fixed on concave substrates. The model matched a key experimental observation of stress-fibers forming primarily along free edges of the cells. We also observed that the steady-state shape of the cell was significantly affected by the choice of network architecture used to represent the cytoskeletal actin network. In Chapter 5, we presented a histology-based multiscale model of pre-failure and failure behavior of the aorta. The multiscale model was able to match the experimentally measured properties of the healthy porcine ascending aorta in four different loading configurations and two different directions, and it was successful when applied to experiments in the literature that were not used during the fitting and specification project.

## 6.2 Future work

The network model presented in this dissertation simulated biopolymer networks minus any chemical effects present in biological tissues. The only chemical mechanism simulated was the actin-myosin motor kinetics, which was modeled using a phenomenological Hill-like constitutive model; external biochemical signals initiating the contraction of fibers were not explicitly modeled. Chemical effects, however, can significantly affect both the active and the passive mechanics of tissues, e.g., mechanical overloading of collagen fibrils places them in a stable, denatured state [Veres et al., 2014]. Denaturation of collagen can also lead to changes in the rest length of fibers, and affect the local stiffness of the tissue and its capacity to remodel [Dittmore et al., 2016]. Thus, a logical extension to the model would be to include these mechanobiological effects in the model which could have significant effects on the mechanics and failure of the network.

Additionally, the network model did not account for growth and remodeling taking place in living tissues. Even in the cytoskeleton of cells, the actin fiber network structure is dynamic, and it changes as the cell migrates, and as the concentration of focal adhesions between the cell and the extracellular matrix evolves. Thus, another area for future work will be to include the effects of remodeling in the network. Fiber-based rules to create cross links between fibers, or to remove connections can be easily added to the model. The network can also be remodelled by conditionally changing the radius of fibers. Such a model can then be used to gain a better insight into, e.g., experimental observations resulting from micromanipulation of single stress-fibers within cell cytoskeletons using laser ablation [Strahs and Berns, 1979, Kumar et al., 2006].

Finally, failure in networks was assumed to occur only within the fibers, and not in the connections between fibers. In certain network constructs, e.g., metallic foams [McCullough et al., 1999], however, fatigue and failure can also occur at fiber cross

links. Furthermore, the network model assumed highly flexible fibers. While this assumption is reasonable for the biopolymer networks considered in this dissertation, networks where the fiber persistence length is comparable to its contour length may require a modified theoretical framework, e.g., bending of fibers can become an important mode of deformation in addition to axial deformation.

# Bibliography

[ABAQUS, 2009] ABAQUS (2009). *ABAQUS/Standard User's Manual, Version 6.9*. Simulia.

[Abel et al., 2013] Abel, J., Luntz, J., and Brei, D. (2013). Hierarchical architecture of active knits. *Smart Materials and Structures*, 22.

[Abhilash et al., 2014] Abhilash, A. S., Baker, B. M., Trappmann, B., Chen, C. S., and Shenoy, V. B. (2014). Remodeling of Fibrous Extracellular Matrices by Contractile Cells: Predictions from Discrete Fiber Network Simulations. *Biophysical Journal*, 107(8):1829–1840.

[Abramowitch and Woo, 2004] Abramowitch, S. D. and Woo, S. L. Y. (2004). An improved method to analyze the stress relaxation of ligaments following a finite ramp time based on the quasi-linear viscoelastic theory. *Journal of Biomechanical Engineering*, 126(1):92–97.

[Aghvami et al., 2016] Aghvami, M., Billiar, K. L., and Sander, E. A. (2016). Fiber network models predict enhanced cell mechanosensing on fibrous gels. *Journal of Biomechanical Engineering*, 138(10):101006–11.

[Amos and Amos, 1991] Amos, L. A. and Amos, W. B. (1991). *Molecules of the Cytoskeleton*. Macmillan Education UK, London.

[Andarawis-Puri and Flatow, 2011] Andarawis-Puri, N. and Flatow, E. L. (2011). Tendon fatigue in response to mechanical loading. *Journal of Musculoskeletal and Neuronal Interactions*, 11:106–114.

[Andrews et al., 1999] Andrews, E., Gibson, L., and Ashby, M. (1999). The creep of cellular solids. *Acta Materialia*, 47(10):2853 – 2863.

[Arruda and Boyce, 1993] Arruda, E. M. and Boyce, M. C. (1993). A three dimensional constitutive model for the large stretch behavior of rubber elastic materials. *J. Mech. Phys. Solids*, 41:389–412.

[Ashby et al., 2000] Ashby, M., Evans, A., Fleck, N., Gibson, L., Hutchinson, J., and Wadley, H., editors (2000). *Metal Foams: A Design Guide*. Butterworth-Heinemann, Burlington.

[ASTM, 2014] ASTM (2014). Standard Test Method for Lap Shear Adhesion for Fiber Reinforced Plastic (FRP) Bonding. Technical report.

[Avanzini et al., 2014] Avanzini, A., Battini, D., Bagozzi, L., and Bisleri, G. (2014). Biomechanical Evaluation of Ascending Aortic Aneurysms. *BioMed Research International*, 2014:1–9.

[Azadani et al., 2013] Azadani, A. N., Chitsaz, S., Mannion, A., Mookhoek, A., Wisneski, A., Guccione, J. M., Hope, M. D., Ge, L., and Tseng, E. E. (2013). Biomechanical Properties of Human Ascending Thoracic Aortic Aneurysms. *The Annals of Thoracic Surgery*, 96(1):50–58.

[Babaei et al., 2015] Babaei, B., Davarian, A., Pryse, K. M., Elson, E. L., and Genin, G. M. (2015). Efficient and optimized identification of generalized maxwell viscoelastic relaxation spectra. *Journal of the mechanical behavior of biomedical materials*, 55:32–41.

[Babu et al., 2015] Babu, A. R., Byju, A. G., and Gundiah, N. (2015). Biomechanical Properties of Human Ascending Thoracic Aortic Dissections. *Journal of Biomechanical Engineering*, 137(8):081013.

[Ban et al., 2016] Ban, E., Barocas, V. H., Shephard, M. S., and Picu, R. C. (2016). Softening in random networks of non-identical beams. *Journal of the Mechanics and Physics of Solids*, 87:38 – 50.

[Ban et al., 2017] Ban, E., Zhang, S., Zarei, V., H Barocas, V., Winkelstein, B., and R Picu, C. (2017). Collagen organization in facet capsular ligaments varies with spinal region and with ligament deformation. *Journal of Biomechanical Engineering*, 139.

[Barnes et al., 2007] Barnes, C. P., Sell, S. A., Boland, E. D., Simpson, D. G., and Bowlin, G. L. (2007). Nanofiber technology: Designing the next generation of tissue engineering scaffolds. *Advanced Drug Delivery Reviews*, 59(14):1413 – 1433. Intersection of Nanoscience and Modern Surface Analytical Methodology.

[Barreto et al., 2013] Barreto, S., Clausen, C. H., Perrault, C. M., Fletcher, D. A., and Lacroix, D. (2013). A multi-structural single cell model of force-induced interactions of cytoskeletal components. *Biomaterials*, 34(26):6119–26.

[Beloussov et al., 2000] Beloussov, L. V., Louchinskaia, N. N., and Stein, A. L. A. (2000). Tension-dependent collective cell movements in the early gastrula ectoderm of xenopus laevis embryos. *Development Genes and Evolution*, 210:92–104.

[Beningo et al., 2001] Beningo, K. A., Dembo, M., Kaverina, I., Small, V. J., and Yuli, W. (2001). Nascent focal adhesions are responsible for the generation of strong propulsive forces in migrating fibroblasts. *Journal of Cell Biology*, 153:881–888.

[Berger and Elefteriades, 2012] Berger, J. and Elefteriades, J. (2012). Toward Uniformity in Reporting of Thoracic Aortic Diameter. *International Journal of Angiology*, 21(04):243–244.

[Billiar and Sacks, 2000] Billiar, K. L. and Sacks, M. (2000). Biaxial mechanical properties of the native and glutaraldehyde-treated aortic valve cusp: Part ii - A structural constitutive model. *J. Biomech. Eng.*, 122:327–335.

[Black et al., 2008] Black, L. D., Allen, P. G., Morris, S. M., Stone, P. J., and Suki, B. (2008). Mechanical and failure properties of extracellular matrix sheets as a function of structural protein composition. *Biophys. J.*, 94:1916–1929.

[Boey et al., 1998] Boey, S. K., Boal, D. H., and Discher, D. E. (1998). Simulations of the Erythrocyte Cytoskeleton at Large Deformation. I. Microscopic Models. *Biophysical Journal*, 75(3):1573–1583.

[Bottino, 1998] Bottino, D. C. (1998). Modeling Viscoelastic Networks and Cell Deformation in the Context of the Immersed Boundary Method. *J. Comput. Phys.*, 147:86–113.

[Broedersz et al., 2010a] Broedersz, C. P., Depken, M., Yao, N. Y., Pollak, M. R., Weitz, D. A., and MacKintosh, F. C. (2010a). Cross-link-governed dynamics of biopolymer networks. *Phys. Rev. Lett.*, 105:238101.

[Broedersz et al., 2010b] Broedersz, C. P., Kasza, K. E., Jawerth, L. M., Mnster, S., Weitz, D. A., and MacKintosh, F. C. (2010b). Measurement of nonlinear rheology of cross-linked biopolymer gels. *Soft Matter*, 6:4120–4127.

[Broedersz and MacKintosh, 2014] Broedersz, C. P. and MacKintosh, F. C. (2014). Modeling semiflexible polymer networks. *arXiv:1404.4332 [cond-mat, physics:physics]*. arXiv: 1404.4332.

[Burd, 2008] Burd, H. J. (2008). A structural constitutive model for the human lens capsule. *Biomech Model Mechanobiol*, 8(3):217–231.

[Chandran and Barocas, 2005] Chandran, P. L. and Barocas, V. H. (2005). Representative microstructure finite elements for collagen gels. In Gladwell, G., Huyghe, J., Raats, P., and Cowin, S., editors, *IUTAM Symposium on Physicochemical and Electromechanical Interactions in Porous Media*, volume 125 of *Solid Mechanics and Its Applications*, pages 37–42. Springer Netherlands.

[Chandran and Barocas, 2006a] Chandran, P. L. and Barocas, V. H. (2006a). Affine versus non-affine fibril kinematics in collagen networks: theoretical studies of network behavior. *Journal of Biomechanical Engineering*, 128:259–270.

[Chandran and Barocas, 2006b] Chandran, P. L. and Barocas, V. H. (2006b). Deterministic material-based averaging theory model of collagen gel micromechanics. *Journal of Biomechanical Engineering*, 129(2):137–147.

[Chandran et al., 2008] Chandran, P. L., Stylianopoulos, T., and Barocas, V. H. (2008). Microstructure-Based, Multiscale Modeling for the Mechanical Behavior of Hydrated Fiber Networks. *Multiscale Modeling & Simulation*, 7(1):22–43.

[Clark and Glagov, 1985] Clark, J. M. and Glagov, S. (1985). Transmural organization of the arterial media. The lamellar unit revisited. *Arteriosclerosis (Dallas, Tex.)*, 5(1):19–34.

[Davies et al., 2006] Davies, R. R., Gallo, A., Coady, M. A., Tellides, G., Botta, D. M., Burke, B., Coe, M. P., Kopf, G. S., and Elefteriades, J. A. (2006). Novel Measurement of Relative Aortic Size Predicts Rupture of Thoracic Aortic Aneurysms. *The Annals of Thoracic Surgery*, 81(1):169–177.

[Davies et al., 2002] Davies, R. R., Goldstein, L. J., Coady, M. A., Tittle, S. L., Rizzo, J. A., Kopf, G. S., and Elefteriades, J. A. (2002). Yearly rupture or dissection rates for thoracic aortic aneurysms: simple prediction based on size. *The Annals of thoracic surgery*, 73(1):17–27; discussion 27–8.

[De Vita and Slaughter, 2007] De Vita, R. and Slaughter, W. S. (2007). A constitutive law for the failure behavior of medial collateral ligaments. *Biomechanics and Modeling in Mechanobiology*, 6(3):189–197.

[Delaunay, 1934] Delaunay, B. (1934). Sur la sphère vide. *Bulletin de l'Academie des Sciences de l'URSS, Classe des sciences mathématiques et naturelles*, 6:793–800.

[Deshpande and Fleck, 2000] Deshpande, V. S. and Fleck, N. A. (2000). Isotropic constitutive models for metallic foams. *J. Mech. Phys. Solids*, 48:1253–1283.

[Deshpande et al., 2006] Deshpande, V. S., McMeeking, R. M., and Evans, A. G. (2006). A bio-chemo-mechanical model for cell contractility. *Proceedings of the National Academy of Sciences*, 103(38):14015–14020.

[Dhume et al., 2018] Dhume, R. Y., Shih, E. D., and Barocas, V. H. (2018). Multiscale model of fatigue of collagen gels. *Biomechanics and Modeling in Mechanobiology*.

[Dingemans et al., 2000] Dingemans, K. P., Teeling, P., Lagendijk, J. H., and Becker, A. E. (2000). Extracellular matrix of the human aortic media: an ultrastructural histochemical and immunohistochemical study of the adult aortic media. *The Anatomical record*, 258(1):1–14.

[Dittmore et al., 2016] Dittmore, A., Silver, J., Sarkar, S. K., Marmer, B., Goldberg, G. I., and Neuman, K. C. (2016). Internal strain drives spontaneous periodic buckling in collagen and regulates remodeling. *Proceedings of the National Academy of Sciences*, 113(30):8436–8441.

[Dobrin, 1978] Dobrin, P. B. (1978). Mechanical properties of arteries. *Physiological Reviews*, 58(2):397–460.

[Dong et al., 1991] Dong, C., Skalak, R., and Sung, K.-L. P. (1991). Cytoplasmic rheology of passive neutrophils. *Biorheology*, 28:557–567.

[Dotter et al., 1950] Dotter, C. T., Roberts, D. J., and Steinberg, I. (1950). Aortic length: angiocardiographic measurements. *Circulation*, 2(6):915–20.

[Driessen et al., 2005] Driessen, N. J. B., Bouten, C. V. C., and Baaijens, F. P. T. (2005). A structural constitutive model for collagenous cardiovascular tissues incorporating the angular fiber distribution. *J. Biomech. Eng.*, 127:494–503.

[Edwards, 1973] Edwards, E. (1973). A review of: Biomechanics: Its foundations and objectives. Edited by Y. C. Fung, N. Perrone and M. Anliker. *Ergonomics*, 16(4):543–544. PMID: 28086286.

[Elefteriades, 2010] Elefteriades, J. A. (2010). Indications for aortic replacement. *The Journal of Thoracic and Cardiovascular Surgery*, 140(6):S5–S9.

[Erdős and Rényi, 1959] Erdős, P. and Rényi, A. (1959). On random graphs. *Publicationes Mathematicae*, 6:290–297.

[Etz et al., 2012] Etz, C. D., Misfeld, M., Borger, M. A., Luehr, M., Strotdrees, E., and Mohr, F.-W. (2012). Current Indications for Surgical Repair in Patients with Bicuspid Aortic Valve and Ascending Aortic Ectasia. *Cardiology Research and Practice*, 2012:1–9.

[Evans and Yeung, 1989] Evans, E. and Yeung, A. (1989). Apparent viscosity and cortical tension of blood granulocytes determined by micropipet aspiration. *Biophysical Journal*, 56:151–160.

[Fabry et al., 2001] Fabry, B., Maksym, G. N., Butler, J. P., Glogauer, M., Navajas, D., and Fredberg, J. J. (2001). Scaling the microrheology of living cells. *Phys. Rev. Lett.*, 87:148102.

[Ferrara and Pandolfi, 2008] Ferrara, A. and Pandolfi, A. (2008). Numerical modelling of fracture in human arteries. *Computer Methods in Biomechanics and Biomedical Engineering*, 11(5):553–567.

[Flory, 1953] Flory, P. J. (1953). *Principles of Polymer Chemistry*. Cornell University Press, Ithaca, NY.

[Flory and Rehner, 1943] Flory, P. J. and Rehner, J. J. (1943). Statistical mechanics of crosslinked polymer networks i. rubberlike elasticity. *J. Chem. Phys.*, 11:512.

[Floyd, 1962] Floyd, R. W. (1962). Algorithm 97: Shortest path. *Commun. ACM*, 5(6):345–.

[Freeman, 1999] Freeman, M. A. R. (1999). Is collagen fatigue failure a cause of osteoarthrosis and prosthetic component migration? a hypothesis. *Journal of Orthopaedic Research*, 17:3–8.

[Fung, 1967] Fung, Y. (1967). Elasticity of soft tissues in simple elongation. *American Journal of Physiology-Legacy Content*, 213(6):1532–1544. PMID: 6075755.

[Fung, 1981] Fung, Y. C. (1981). *Bio-viscoelastic Solids*, pages 196–260. Springer New York, New York, NY.

[Gardel et al., 2006] Gardel, M., Nakamura, F., and Weitz, D. (2006). Prestressed f-actin networks cross-linked by hinged filamins replicate mechanical properties of cells. *Proc. Natl. Acad. Sci. USA*, 103:1762–1767.

[Gardel et al., 2004a] Gardel, M., Shin, J., and Weitz, D. (2004a). Elastic behavior of cross-linked and bundled actin networks. *Science*, 304:1301–1305.

[Gardel et al., 2004b] Gardel, M. L., Shin, J. H., MacKintosh, F. C., Mahadevan, L., Matsudaira, P. A., and Weitz, D. A. (2004b). Scaling of f-actin network rheology to probe single filament elasticity and dynamics. *Phys. Rev. Lett.*, 93:188102.

[Gasser and Holzapfel, 2006] Gasser, T. C. and Holzapfel, G. A. (2006). Modeling the propagation of arterial dissection. *European Journal of Mechanics - A/Solids*, 25(4):617–633.

[Gordon, 1976] Gordon, M. (1976). The physics of rubber elasticity (third edition). l. r. g. treloar, clarendon press, oxford. 1975 pp. xii + 370. price: 14.00. *British Polymer Journal*, 8(1):39–39.

[Gow and Taylor, 1968] Gow, B. S. and Taylor, M. G. (1968). Measurement of viscoelastic properties of arteries in the living dog. *Circ Res*, 23(1):111–122.

[Gray et al., 2000] Gray, H., Lewis, W. H. W. H., and Bartleby.com, I. (2000). *Anatomy of the human body*. Bartleby.com.

[Gregory et al., 2011] Gregory, D. E., Veldhuis, J. H., Horst, C., Wayne Brodland, G., and Callaghan, J. P. (2011). Novel lap test determines the mechanics of delamination between annular lamellae of the intervertebral disc. *Journal of Biomechanics*, 44(1):97–102.

[Guo et al., 2012] Guo, C.-L., Ouyang, M., Yu, J.-Y., Maslov, J., Price, A., and Shen, C.-Y. (2012). Long-range mechanical force enables self-assembly of epithelial tubular patterns. *Proceedings of the National Academy of Sciences*, 109(15):5576–5582.

[Hadi et al., 2012] Hadi, M. F., Sander, E. A., and Barocas, V. H. (2012). Multiscale Model Predicts Tissue-Level Failure From Collagen Fiber-Level Damage. *Journal of Biomechanical Engineering*, 134(9):091005.

[Hansen et al., 1996] Hansen, J., Skalak, R., Chien, S., and Hoger, A. (1996). An elastic network model based on the structure of the red blood cell membrane skeleton. *Biophys. J.*, 70:146–166.

[Harris et al., 1981] Harris, A. K., Stopak, D., and Wild, P. (1981). Fibroblast traction as a mechanism for collagen morphogenesis. *Nature*, 290:249 EP –.

[Haskett et al., 2012] Haskett, D., Speicher, E., Fouts, M., Larson, D., Azhar, M., Utzinger, U., and Vande Geest, J. (2012). The effects of angiotensin II on the coupled microstructural and biomechanical response of C57BL/6 mouse aorta. *Journal of Biomechanics*, 45(5):772–779.

[Hatami-Marbini and Mofrad, 2015] Hatami-Marbini, H. and Mofrad, M. R. K. (2015). Rheology and Mechanics of the Cytoskeleton. pages 187–205. Springer, New York, NY.

[Hill, 1938] Hill, A. V. (1938). The heat of shortening and the dynamic constants of muscle. *Proceedings of the Royal Society of London B: Biological Sciences*, 126(843):136–195.

[Holmes et al., 2013] Holmes, K. W., Maslen, C. L., Kindem, M., Kroner, B. L., Song, H. K., Ravekes, W., Dietz, H., Weinsaft, J. W., Roman, M. J., Devereux, R. B., Pyeritz, R. E., Bavaria, J., Milewski, K., Milewicz, D., LeMaire, S. A., Hendershot, T., Eagle, K. A., Tolunay, H. E., Desvigne-Nickens, P., Silberbach, M., and GenTAC Registry Consortium (2013). GenTAC registry report: Gender differences among individuals with genetically triggered thoracic aortic aneurysm and dissection. *American Journal of Medical Genetics Part A*, 161(4):779–786.

[Holzapfel and Gasser, 2000] Holzapfel, G. A. and Gasser, T. C. (2000). A new constitutive framework for arterial wall mechanics and a comparative study of material models. *J. Elasticity*, 61:1–48.

[Huisman et al., 2007] Huisman, E. M., Dillen, v. T., and van der Giessen, E. (2007). Three-dimensional cross-linked f-actin networks: relation between network architecture and mechanical behavior. *Phys. Rev. Lett.*, 99:208103.

[Humphrey, 1995] Humphrey, J. (1995). Mechanics of arterial wall: Review and directions. *Critical reviews in Biomed. Engr.*, 23:1–162.

[Huxley, 1957] Huxley, A. F. (1957). Muscle structure and theories of contraction. *Progress in biophysics and biophysical chemistry*, 7:255–318.

[Iliopoulos et al., 2009] Iliopoulos, D. C., Kritharis, E. P., Giagini, A. T., Papadodima, S. A., and Sokolis, D. P. (2009). Ascending thoracic aortic aneurysms are associated with compositional remodeling and vessel stiffening but not weakening in age-matched subjects. *The Journal of Thoracic and Cardiovascular Surgery*, 137(1):101–109.

[Ingber, 2003] Ingber, D. E. (2003). Tensegrity i. cell structure and hierarchical systems biology. *Journal of Cell Science*, 116(7):1157–1173.

[Isabey et al., 2016] Isabey, D., Pelle, G., André Dias, S., Bottier, M., Nguyen, N.-M., Filoche, M., and Louis, B. (2016). Multiscale evaluation of cellular adhesion alteration and cytoskeleton remodeling by magnetic bead twisting. *Biomechanics and Modeling in Mechanobiology*, 15(4):947–963.

[Isselbacher, 2005] Isselbacher, E. M. (2005). Thoracic and Abdominal Aortic Aneurysms. *Circulation*, 111(6):816–828.

[Jabbari-Farouji et al., 2008] Jabbari-Farouji, S., Atakhorrami, M., Mizuno, D., Eiser, E., Wegdam, G. H., MacKintosh, F. C., Bonn, D., and Schmidt, C. F. (2008). High-bandwidth viscoelastic properties of aging colloidal glasses and gels. *Phys. Rev. E*, 78:061402.

[Johnson et al., 1994] Johnson, G., Tramaglini, D., Levine, R., Kazunori, O., NamY-ong, C., and Savio, L. W. (1994). Tensile and viscoelastic properties of human patellar tendon. *Journal of Orthopaedic Research*, 12(6):796–803.

[Kaiser et al., 2008] Kaiser, T., Kellenberger, C. J., Albisetti, M., Bergsträsser, E., and Valsangiacomo Buechel, E. R. (2008). Normal values for aortic diameters in children and adolescents assessment in vivo by contrast-enhanced CMR-angiography. *Journal of Cardiovascular Magnetic Resonance*, 10(1):56.

[Kiehart et al., 2000] Kiehart, D. P., Galbraith, C. G., Edwards, K. A., Rickoll, W. L., and Montague, R. A. (2000). Multiple forces contribute to cell sheet morphogenesis for dorsal closure in drosophila. *The Journal of Cell Biology*, 149:471 – 490.

[Knappeis and Carlsen, 1962] Knappeis, G. G. and Carlsen, F. (1962). The ultrastructure of the z disc in skeletal muscle. *The Journal of Cell Biology*, 13(2):323–335.

[Koch et al., 2014] Koch, R. G., Tsamis, A., D'Amore, A., Wagner, W. R., Watkins, S. C., Gleason, T. G., and Vorp, D. A. (2014). A custom image-based analysis tool for quantifying elastin and collagen micro-architecture in the wall of the human aorta from multi-photon microscopy. *Journal of biomechanics*, 47(5):935–943.

[Koeller, 1984] Koeller, R. (1984). Applications of fractional calculus to the theory of viscoelasticity. *J Appl Mech*, 51:299–307.

[Koh et al., 2013] Koh, C., Strange, D., Tonsomboon, K., and Oyen, M. (2013). Failure mechanisms in fibrous scaffolds. *Acta Biomaterialia*, 9:7326–7334.

[Kozuń, 2016] Kozuń, M. (2016). Delamination properties of the human thoracic arterial wall with early stage of atherosclerosis lesions. *Journal of Theoretical and Applied Mechanics*, 54(1):229.

[Krishnan et al., 2015] Krishnan, K., Ge, L., Haraldsson, H., Hope, M. D., Saloner, D. A., Guccione, J. M., and Tseng, E. E. (2015). Ascending thoracic aortic

aneurysm wall stress analysis using patient-specific finite element modeling of in vivo magnetic resonance imaging. *Interactive cardiovascular and thoracic surgery*, 21(4):471–80.

[Kuhl et al., 2005] Kuhl, E., Garikipati, K., Arruda, E. M., and Grosh, K. (2005). Remodeling of biological tissue: Mechanically induced reorientation of a transversely isotropic chain network. *Journal of the Mechanics and Physics of Solids*, 53(7):1552 – 1573.

[Kumar et al., 2006] Kumar, S., Maxwell, I. Z., Heisterkamp, A., Polte, T. R., Lele, T. P., Salanga, M., Mazur, E., and Ingber, D. E. (2006). Viscoelastic Retraction of Single Living Stress Fibers and Its Impact on Cell Shape, Cytoskeletal Organization, and Extracellular Matrix Mechanics. *Biophysical Journal*, 90(10):3762–3773.

[Ladoux, 2009] Ladoux, B. (2009). Cells guided on their journey. *Nature Physics*, 5:377.

[Lai et al., 2013] Lai, V. K., Hadi, M. F., Tranquillo, R. T., and Barocas, V. H. (2013). A multiscale approach to modeling the passive mechanical contribution of cells in tissues. *Journal of Biomechanical Engineering*, 135(7):0710071–0710079.

[Lai et al., 2012] Lai, V. K., Lake, S. P., Frey, C. R., Tranquillo, R. T., and Barocas, V. H. (2012). Mechanical behavior of collagen-fibrin co-gels reflects transition from series to parallel interactions with increasing collagen content. *J. Biomech. Eng.*, 134:011004–9.

[Lake and Barocas, 2012] Lake, S. P. and Barocas, V. H. (2012). Mechanics and kinematics of soft tissue under indentation are determined by the degree of initial collagen fiber allignment. *J. Mech. Behav. Biomed. Mater.*, 13:25–35.

[Lanir, 1983] Lanir, Y. (1983). Constitutive equations for fibrous connective tissues. *J. Boimech.*, 16:1–12.

[Li et al., 2007] Li, J., Lykotrafitis, G., Dao, M., and Suresh, S. (2007). Cytoskeletal dynamics of human erythrocyte. *PNAS*, 104(12):4937–4942.

[Liao et al., 2006] Liao, J., Yang, L., Grashow, J., and Sacks, M. S. (2006). The relation between collagen fibril kinematics and mechanical properties in the mitral valve anterior leaflet. *Journal of Biomechanical Engineering*, 129(1):78–87.

[Linka et al., 2018] Linka, K., Hillgrtner, M., and Itskov, M. (2018). Fatigue of soft fibrous tissues: Multi-scale mechanics and constitutive modeling. *Acta biomaterialia*, 71:398410.

[Ma et al., 2013] Ma, X., Schickel, M., Stevenson, M., Sarang-Sieminski, A., Gooch, K., Ghadiali, S., and Hart, R. (2013). Fibers in the extracellular matrix enable long-range stress transmission between cells. *Biophys. J.*, 104:1410–1418.

[MacKintosh et al., 1995] MacKintosh, F. C., Käs, J., and Janmey, P. A. (1995). Elasticity of semiflexible biopolymer networks. *Phys. Rev. Lett.*, 75:4425–4428.

[MacLean et al., 1999] MacLean, N. F., Dudek, N. L., and Roach, M. R. (1999). The role of radial elastic properties in the development of aortic dissections. *Journal of vascular surgery*, 29(4):703–10.

[Maksym et al., 1998] Maksym, G. N., Fredberg, J. J., and Bates, J. H. (1998). Force heterogeneity in a two-dimenstional network model of lung tissue. *Appl. Physiol.*, 85:1223–1229.

[Mao et al., 2008] Mao, S. S., Ahmadi, N., Shah, B., Beckmann, D., Chen, A., Ngo, L., Flores, F. R., lin Gao, Y., and Budoff, M. J. (2008). Normal Thoracic Aorta Diameter on Cardiac Computed Tomography in Healthy Asymptomatic Adults. *Academic Radiology*, 15(7):827–834.

[Martin and Sun, 2013] Martin, C. and Sun, W. (2013). Modeling of long-term fatigue damage of soft tissue with stress softening and permanent set effects. *Biomech Model Mechanobiol*, 12:645–655.

[Martin and Sun, 2014] Martin, C. and Sun, W. (2014). Simulation of long-term fatigue damage in bioprosthetic heart valves: effects of leaflet and stent elastic properties. *Biomechanics and Modeling in Mechanobiology*, 13(4):759–770.

[Martin et al., 2015] Martin, C., Sun, W., and Elefteriades, J. (2015). Patient-specific finite element analysis of ascending aorta aneurysms. *American Journal of Physiology-Heart and Circulatory Physiology*, 308(10):H1306–H1316.

[Martufi et al., 2014] Martufi, G., Gasser, T. C., Appoo, J. J., and Di Martino, E. S. (2014). Mechano-biology in the thoracic aortic aneurysm: a review and case study. *Biomechanics and Modeling in Mechanobiology*, 13(5):917–928.

[MATLAB, 2013] MATLAB (2013). *version 8.0.2.701 (R2013b)*. The MathWorks Inc., Natick, Massachusetts.

[Matura et al., 2007] Matura, L. A., Ho, V. B., Rosing, D. R., and Bondy, C. A. (2007). Aortic Dilatation and Dissection in Turner Syndrome. *Circulation*, 116(15):1663–1670.

[Maxwell, 1864] Maxwell, J. C. (1864). L. on the calculation of the equilibrium and stiffness of frames. *Philos. Mag.*, 27:294–299.

[McCullough et al., 1999] McCullough, K. Y. G., Fleck, N. A., and Ashby, M. F. (1999). The stress-life fatigue behaviour of aluminium alloy foams. *Fatigue Fract. Engng. Mater. Struct.*, 23:199–208.

[Mijailovich et al., 2002] Mijailovich, S. M., Kojic, M., Zivkovic, M., Fabry, B., and Fredberg, J. J. (2002). A finite element model of cell deformation during magnetic bead twisting. *Journal of Applied Physiology*, 93(4):1429–1436. PMID: 12235044.

[Miner, 1945] Miner, M. A. (1945). Cumulative damage in fatigue. *Journal of Applied Mechanics*, 67:159–164.

[Mitchison and Cramer, 1996] Mitchison, T. and Cramer, L. (1996). Actin-based cell motility and cell locomotion. *Cell*, 84(3):371 – 379.

[Morin et al., 2013] Morin, K., Smith, A., Davis, G., and Tranquillo, R. (2013). Aligned human microvessels formed in 3-d fibrin gel by constraint of gel contraction. *Microvasc. Res.*, 190:12–22.

[Münster et al., 2013] Münster, S., Jawerth, L. M., Leslie, B. A., Weitz, J. I., Fabry, B., and Weitz, D. A. (2013). Strain history dependence of the nonlinear stress response of fibrin and collagen networks. *Proceedings of the National Academy of Sciences*, 110(30):12197–12202.

[Nachtrab et al., 2011] Nachtrab, S., Kapfer, S. C., Arns, C. H., Madadi, M., Mecke, K., and Schrder-Turk, G. E. (2011). Morphology and linear-elastic moduli of random network solids. *Advanced Materials*, 23(22-23):2633–2637.

[Nam et al., 2016] Nam, S., Hu, K., Butte, M., and Chaudhuri, O. (2016). Strain-enhanced stress relaxation impacts nonlinear elasticity in collagen gels. *Proceedings of the National Academy of Sciences of the United States of America*, 113(20):5492–5497.

[Newman, 2001] Newman, M. E. J. (2001). Scientific collaboration networks. II. Shortest paths, weighted networks, and centrality. *Phys. Rev. E.*, 64:016132.

[Newman, 2004] Newman, M. E. J. (2004). Analysis of weighted networks. *Phys. Rev. E. Stat. Nonlin. Soft Matter Phys.*, 70:056131.

[Nijs et al., 2014] Nijs, J., Gelsomino, S., Lucà, F., Parise, O., Maessen, J. G., and Meir, M. L. (2014). Unreliability of aortic size index to predict risk of aortic dissection in a patient with Turner syndrome. *World Journal of Cardiology*, 6(5):349.

[Okamoto et al., 2002] Okamoto, R. J., Wagenseil, J. E., DeLong, W. R., Peterson, S. J., Kouchoukos, N. T., and Sundt, T. M. (2002). Mechanical properties of dilated human ascending aorta. *Annals of biomedical engineering*, 30(5):624–35.

[Oliveira et al., 2014] Oliveira, C. L. N., Bates, J. H. T., and Suki, B. (2014). A network model of correlated growth of tissue stiffening in pulmonary fibrosis. *New Journal of Physics*, 16(6):065022. arXiv: 1312.7031.

[Pal et al., 2014] Pal, S., Tsamis, A., Pasta, S., D'Amore, A., Gleason, T. G., Vorp, D. A., and Maiti, S. (2014). A mechanistic model on the role of radially-running collagen fibers on dissection properties of human ascending thoracic aorta. *Journal of Biomechanics*, 47(5):981–988.

[Pape et al., 2007] Pape, L. A., Tsai, T. T., Isselbacher, E. M., Oh, J. K., O'Gara, P. T., Evangelista, A., Fattori, R., Meinhardt, G., Trimarchi, S., Bossone, E., Suzuki, T., Cooper, J. V., Froehlich, J. B., Nienaber, C. A., Eagle, K. A., and International Registry of Acute Aortic Dissection (IRAD) Investigators (2007). Aortic Diameter >=5.5 cm Is Not a Good Predictor of Type A Aortic Dissection: Observations From the International Registry of Acute Aortic Dissection (IRAD). *Circulation*, 116(10):1120–1127.

[Pasta et al., 2012] Pasta, S., Phillippi, J. A., Gleason, T. G., and Vorp, D. A. (2012). Effect of aneurysm on the mechanical dissection properties of the human ascending thoracic aorta. *The Journal of Thoracic and Cardiovascular Surgery*, 143(2):460–467.

[Pathak et al., 2008] Pathak, A., Deshpande, V. S., McMeeking, R. M., and Evans, A. G. (2008). The simulation of stress fibre and focal adhesion development in cells on patterned substrates. *Journal of the Royal Society Interface*, 5(22):507–524.

[Peeters et al., 2005] Peeters, E., Oomens, C., Bouten, C., Bader, D., and Baaijens, F. (2005). Mechanical and failure properties of single attached cells under compression. *Journal of Biomechanics*, 38(8):1685–1693.

[Pena, 2011] Pena, E. (2011). Prediction of the softening and damage effects with permanent set in fibrous biological materials. *J Mech Phys Solids*, 59:1808–1822.

[Pichamuthu et al., 2013] Pichamuthu, J. E., Phillippi, J. A., Cleary, D. A., Chew, D. W., Hempel, J., Vorp, D. A., and Gleason, T. G. (2013). Differential Tensile Strength and Collagen Composition in Ascending Aortic Aneurysms by Aortic Valve Phenotype. *The Annals of Thoracic Surgery*, 96(6):2147–2154.

[Picu, 2011] Picu, R. (2011). Mechanics of random fiber networks - a review. *Soft Matter*, 7:6768–6785.

[Provenzano et al., 2001] Provenzano, P., Lakes, R., Keenan, T., and vanderby, R. (2001). Nonlinear ligament viscoelasticity. *Annals of Biomedical Engineering*, 29(10):908–914.

[Pryse et al., 2003] Pryse, K. M., Nekouzadeh, A., Genin, G. M., Elson, E. L., and Zahalak, G. I. (2003). Incremental mechanics of collagen gels: New experiments and a new viscoelastic model. *Annals of Biomedical Engineering*, 31:1287–1296.

[Purslow et al., 1998] Purslow, P. P., Wess, T. J., and Hukins, D. W. (1998). Collagen orientation and molecular spacing during creep and stress-relaxation in soft connective tissues. *Journal of Experimental Biology*, 201(1):135–142.

[Puxkandl et al., 2002] Puxkandl, R., Zizak, I., Paris, O., Keckes, J., Tesch, W., Bernstorff, S., Purslow, P., and Fratzl, P. (2002). Viscoelastic properties of collagen: synchrotron radiation investigations and structural model. *Philosophical Transactions of the Royal Society B: Biological Sciences*, 357(1418):191–197.

[Raghupathy and Barocas, 2010] Raghupathy, R. and Barocas, V. H. (2010). Generalized Anisotropic Inverse Mechanics for Soft Tissues. *Journal of Biomechanical Engineering*, 132(8):081006.

[Raghupathy et al., 2011] Raghupathy, R., Witzenburg, C., Lake, S. P., Sander, E. A., and Barocas, V. H. (2011). Identification of Regional Mechanical Anisotropy in Soft Tissue Analogs. *Journal of Biomechanical Engineering*, 133(9):091011.

[Rajagopal et al., 2018] Rajagopal, V., Holmes, W. R., and Lee, P. V. S. (2018). Computational modeling of single-cell mechanics and cytoskeletal mechanobiology. *Wiley Interdisciplinary Reviews: Systems Biology and Medicine*, 10(2):e1407.

[Ritter et al., 2009] Ritter, M. C., Jesudason, R., Majumdar, A., Stamenovic, D., Buczek-Thomas, J. A., Stone, P. J., Nugent, M. A., and Suki, B. (2009). A zipper network model of the failure mechanics of extracellular matrices. *Proc Natl Acad Sci U S A*, 106(4):1081–1086.

[Roberts and Garboczi, 2001] Roberts, A. and Garboczi, E. (2001). Elastic moduli of model random three-dimensional closed-cell cellular solids. *Acta Materialia*, 49(2):189 – 197.

[Roberts and Garboczi, 2002] Roberts, A. and Garboczi, E. (2002). Elastic properties of model random three-dimensional open-cell solids. *Journal of the Mechanics and Physics of Solids*, 50(1):33 – 55.

[Rogers, 1983] Rogers, L. (1983). Operators and fractional derivatives for viscoelastic constitutive equations. *J Rheol*, 27:351–372.

[Sakamoto et al., 2016] Sakamoto, Y., Buchanan, R. M., and Sacks, M. S. (2016). On intrinsic stress fiber contractile forces in semilunar heart valve interstitial cells using a continuum mixture model. *Journal of the Mechanical Behavior of Biomedical Materials*, 54:244–258.

[Sander et al., 2009a] Sander, E., Stylianopoulos, T., Tranquillo, R., and Barocas, V. (2009a). Image-based multiscale modeling predicts tissue-level and network-level fiber reorganization in stretched cell-compacted collagen gels. *Proc. Natl. Acad. Sci. USA*, 106:17675–17680.

[Sander et al., 2009b] Sander, E. A., Stylianopoulos, T., Tranquillo, R. T., and Barocas, V. H. (2009b). Image-based multiscale modeling predicts tissue-level and network-level fiber reorganization in stretched cell-compacted collagen gels. *Proceedings of the National Academy of Sciences of the United States of America*, 106(42):17675–17680.

[Sarver et al., 2003] Sarver, J. J., Robinson, P. S., and Elliott, D. M. (2003). Methods for quasi-linear viscoelastic modeling of soft tissue: Application to incremental stress-relaxation experiments. *Journal of Biomechanical Engineering*, 125(5):754–758.

[Sarvestani and Picu, 2004] Sarvestani, A. S. and Picu, C. R. (2004). Network model for the viscoelastic behavior of polymer nanocomposites. *Polymer*, 45(22):7779 – 7790.

[Sasaki et al., 1993] Sasaki, N., Nakayama, Y., Yoshikawa, M., and Enyo, A. (1993). Stress relaxation function of bone and bone collagen. *Journal of Biomechanics*, 26(12):1369 – 1376.

[Schechtman and Bader, 1997] Schechtman, H. and Bader, D. L. (1997). In-vitro fatigue of human tendons. *J. Biomechanics*, 30:829–835.

[Screen, 2008] Screen, H. R. (2008). Investigating load relaxation mechanics in tendon. *Journal of the Mechanical Behavior of Biomedical Materials*, 1(1):51 – 58.

[Shah et al., 2014] Shah, S. B., Witzenburg, C., Hadi, M. F., Wagner, H. P., Goodrich, J. M., Alford, P. W., and Barocas, V. H. (2014). Prefailure and failure mechanics of the porcine ascending thoracic aorta: experiments and a multiscale model. *Journal of biomechanical engineering*, 136(2):021028.

[Shasavari and Picu, 2012] Shasavari, A. and Picu, R. (2012). Model selection for athermal cross-linked fiber networks. *Phys. Rev. E. Stat. Phys.*, 86:011923.

[Shieh and Athanasiou, 2003] Shieh, A. C. and Athanasiou, K. A. (2003). Principles of cell mechanics for cartilage tissue engineering. *Annals of Biomedical Engineering*, 31(1):1–11.

[Shin et al., 2004] Shin, J., Gardel, M., and Weitz, D. (2004). Relating microstructure to rheology of a bundled and cross-linked f-actin network in vitro. *Proc. Natl. Acad. Sci. USA*, 101:9636–9641.

[Snowhill et al., 2004] Snowhill, P. B., Foran, D. J., and Silver, F. H. (2004). A Mechanical Model of Porcine Vascular Tissues-Part I: Determination of Macromolecular Component Arrangement and Volume Fractions. *Cardiovascular Engineering*, 4(4):281–294.

[Sokolis et al., 2008] Sokolis, D. P., Boudoulas, H., and Karayannacos, P. E. (2008). Segmental differences of aortic function and composition: clinical implications. *Hellenic journal of cardiology : HJC = Hellenike kardiologike epitheorese*, 49(3):145–54.

[Sommer et al., 2008] Sommer, G., Gasser, T. C., Regitnig, P., Auer, M., and Holzapfel, G. A. (2008). Dissection Properties of the Human Aortic Media: An Experimental Study. *Journal of Biomechanical Engineering*, 130(2):021007.

[Storm et al., 2005] Storm, C., Pastore, J. J., MacKintosh, F. C., Lubensky, T. C., and Janmey, P. A. (2005). Nonlinear elasticity in biological gels. *Nature*, 435:191 EP –.

[Strahs and Berns, 1979] Strahs, K. R. and Berns, M. W. (1979). Laser microirradiation of stress fibers and intermediate filaments in non-muscle cells from cultured rat heart. *Experimental cell research*, 119(1):31–45.

[Stylianopoulos and Barocas, 2007] Stylianopoulos, T. and Barocas, V. (2007). Multiscale, structure-based modeling for the elastic mechanical behavior of arterial walls. *J. Biomech. Eng.*, 129:611–618.

[Suki et al., 1994] Suki, B., Barabasi, A. L., and Lutchen, K. R. (1994). Lung tissue viscoelasticity: a mathematical framework and its molecular basis. *Journal of Applied Physiology*, 76(6):2749–2759. PMID: 7928910.

[Suki et al., 2005] Suki, B., Ito, S., Stamenovic, D., Lutchen, K. R., and Ingenito, E. P. (2005). Biomechanics of the lung parenchyma: critical roles of collagen and mechanical forces. *Journal of Applied Physiology*, 98(5):1892–1899.

[Suki et al., 2012] Suki, B., Jesudason, R., Sato, S., Parameswaran, H., Araujo, A. D., Majumdar, A., Allen, P. G., and Bartolak-Suki, E. (2012). Mechanical failure, stress redistribution, elastase activity and binding site availability on elastin during the progression of emphysema. *Pulm Pharmacol Ther*, 25(4):268–275.

[Sun et al., 2004] Sun, W., Sacks, M., Fulchiero, G., Lovekamp, J., Vyavahare, N., and Scott, M. (2004). Response of heterograft heart valve biomaterials to moderate cyclic loading. *J Biomed Mater Res A*, 69:658–669.

[Svensson et al., 2003] Svensson, L. G., Kim, K.-H., Lytle, B. W., and Cosgrove, D. M. (2003). Relationship of aortic cross-sectional area to height ratio and the risk of aortic dissection in patients with bicuspid aortic valves. *The Journal of thoracic and cardiovascular surgery*, 126(3):892–3.

[Tanaka and Edwards, 1992] Tanaka, F. and Edwards, S. (1992). Viscoelatic properties of physically crosslinked networks. 1.Transient network theory. *Macromolecules*, 25:1516–1523.

[Théry et al., 2006] Théry, M., Pépin, A., Dressaire, E., Chen, Y., and Bornens, M. (2006). Cell distribution of stress fibres in response to the geometry of the adhesive environment. *Cell Motility*, 63(6):341–355.

[Timmins et al., 2010] Timmins, L. H., Wu, Q., Yeh, A. T., Moore, J. E., and Greenwald, S. E. (2010). Structural inhomogeneity and fiber orientation in the inner arterial media. *American Journal of Physiology-Heart and Circulatory Physiology*, 298(5):H1537–H1545.

[Todorovich-Hunter et al., 1988] Todorovich-Hunter, L., Johnson, D. J., Ranger, P., Keeley, F. W., and Rabinovitch, M. (1988). Altered elastin and collagen synthesis associated with progressive pulmonary hypertension induced by monocrotaline. A biochemical and ultrastructural study. *Laboratory investigation; a journal of technical methods and pathology*, 58(2):184–95.

[Tonar et al., 2015] Tonar, Z., Kubíková, T., Prior, C., Demjén, E., Liška, V., Králíčková, M., and Witter, K. (2015). Segmental and age differences in the elastin network, collagen, and smooth muscle phenotype in the tunica media of the porcine aorta. *Annals of Anatomy - Anatomischer Anzeiger*, 201:79–90.

[Tong et al., 2011] Tong, J., Sommer, G., Regitnig, P., and Holzapfel, G. A. (2011). Dissection Properties and Mechanical Strength of Tissue Components in Human Carotid Bifurcations. *Annals of Biomedical Engineering*, 39(6):1703–1719.

[Trabelsi et al., 2015] Trabelsi, O., Davis, F. M., Rodriguez-Matas, J. F., Duprey, A., and Avril, S. (2015). Patient specific stress and rupture analysis of ascending thoracic aneurysms. *Journal of Biomechanics*, 48(10):1836–1843.

[Treloar, 1946] Treloar, L. (1946). The elasticity of a network of long-chain molecules.iii. *Trans. Faraday Soc.*, 42:83–94.

[Tsamis et al., 2014] Tsamis, A., Pal, S., Phillippi, J. A., Gleason, T. G., Maiti, S., and Vorp, D. A. (2014). Effect of aneurysm on biomechanical properties of "radially-oriented" collagen fibers in human ascending thoracic aortic media. *Journal of biomechanics*, 47(16):3820–4.

[Tsamis et al., 2013] Tsamis, A., Phillippi, J. A., Koch, R. G., Pasta, S., D'Amore, A., Watkins, S. C., Wagner, W. R., Gleason, T. G., and Vorp, D. A. (2013). Fiber micro-architecture in the longitudinal-radial and circumferential-radial planes of ascending thoracic aortic aneurysm media. *Journal of biomechanics*, 46(16):2787–94.

[Vader et al., 2009] Vader, D., Kabla, A., Weitz, D., and Mahadevan, L. (2009). Strain-induced alignment in collagen gels. *PLOS ONE*, 4(6):1–12.

[van Baardwijk and Roach, 1987] van Baardwijk, C. and Roach, M. R. (1987). Factors in the propagation of aortic dissections in canine thoracic aortas. *Journal of biomechanics*, 20(1):67–73.

[van Dillen et al., 2008] van Dillen, T., Onck, P. R., and Van der Giessen, E. (2008). Models for stiffening in cross-linked biopolymer networks: A comparative study. *Journal of the Mechanics and Physics of Solids*, 56(6):2240–2264.

[Veres et al., 2014] Veres, S. P., Harrison, J. M., and Lee, J. M. (2014). Mechanically overloading collagen fibrils uncoils collagen molecules, placing them in a stable, denatured state. *Matrix Biology*, 33:54 – 59.

[Volokh, 2008] Volokh, K. (2008). Prediction of arterial failure based on a microstructural bi-layer fibermatrix model with softening. *Journal of Biomechanics*, 41(2):447–453.

[Voronoi, 1908] Voronoi, G. (1908). Nouvelles applications des paramètres continus à la théorie des formes quadratiques. *Journal für die reine und angewandte Mathematik*, 133:97–102.

[Vorp et al., 2003] Vorp, D. A., Schiro, B. J., Ehrlich, M. P., Juvonen, T. S., Ergin, M. A., and Griffith, B. P. (2003). Effect of aneurysm on the tensile strength and biomechanical behavior of the ascending thoracic aorta. *The Annals of thoracic surgery*, 75(4):1210–4.

[Žagar et al., 2015] Žagar, G., Onck, P., and van der Giessen, E. (2015). Two fundamental mechanisms govern the stiffening of cross-linked networks. *Biophysical Journal*, 108.

[Wagner et al., 2006] Wagner, B., Tharmann, R., and Bausch, A. (2006). Cytoskeletal polymer networks: the molecular structure of cross-linkers determines macroscopic properties. *Proc. Natl. Acad. Sci. USA*, 103:13974–13978.

[Wang et al., 2014] Wang, L., Roper, S. M., Luo, X., and Hill, N. A. (2014). Modelling of tear propagation and arrest in fibre-reinforced soft tissue subject to internal pressure.

[Wang and Guth, 1952] Wang, M. C. and Guth, E. (1952). Statistical theory of networks of nongaussian flexible chains. *J. Chem. Phys.*, 20:1144.

[Wei et al., 2008] Wei, Z., Deshpande, V. S., McMeeking, R. M., and Evans, A. G. (2008). Analysis and interpretation of stress fiber organization in cells subject to cyclic stretch. *Journal of Biomechanical Engineering*, 130(3):031009–031009–9.

[Weightman et al., 1978] Weightman, B., Chappell, D. J., and Jenkins, E. A. (1978). A second study of tensile fatigue properties of human articular cartilage. *Annals of the Rheumatic Diseases*, 37:58–63.

[Weisel and Nagaswami, 1992] Weisel, J. and Nagaswami, C. (1992). Computer modeling of fibrin polymerization kinetics correlated with electron microscope and turbidity observations: Clot structure and assembly are kinetically controlled. *Biophysical Journal*, 63(1):111–128. cited By 199.

[Win et al., 2014] Win, Z., Steucke, K., Sevcik, E., Hald, E., and Alford, P. (2014). Smooth muscle architecture within cell-dense vascular tissue influences functional contractility. *Integr. Biol.*, 6:1201–1210.

[Wisneski et al., 2014] Wisneski, A. D., Mookhoek, A., Chitsaz, S., Hope, M. D., Guccione, J. M., Ge, L., and Tseng, E. E. (2014). Patient-specific finite element analysis of ascending thoracic aortic aneurysm. *The Journal of heart valve disease*, 23(6):765–72.

[Witzenburg et al., 2016] Witzenburg, C., Dhume, R., Shah, S., Korenczuk, C., Wagner, H., Alford, P., and Barocas, V. (2016). Failure of the porcine ascending aorta: Multidirectional experiments and a unifying microstructural model. *Journal of Biomechanical Engineering*.

[Witzenburg et al., 2012] Witzenburg, C., Raghupathy, R., Kren, S. M., Taylor, D. A., and Barocas, V. H. (2012). Mechanical changes in the rat right ventricle with decellularization. *Journal of biomechanics*, 45(5):842–9.

[Witzenburg et al., 2014] Witzenburg, C. M., Dhume, R. Y., Lake, S. P., and Barocas, V. H. (2014). Automatic Segmentation of Mechanically Inhomogeneous Tissues Based on Deformation Gradient Jump. *IEEE Transactions on Medical Imaging*, 35(1):29–41.

[Woo et al., 1981] Woo, S. L., Gomez, M. A., and Akeson, W. H. (1981). The time and history-dependent viscoelastic properties of the canine medial collateral ligament. *Journal of Biomechanical Engineering*, 103(4):293–298.

[Wood et al., 2002] Wood, W., Jacinto, A., Grose, R., Woolner, S., Gale, J., Wilson, C., and Martin, P. (2002). Wound healing recapitulates morphogenesis in drosophila embryos. *Nature Cell Biology*, 4:907–912.

[Zatzman et al., 1954] Zatzman, M., Stacy, R. W., Randall, J., and Eberstein, A. (1954). Time course of stress relaxation in isolated arterial segments. *American Journal of Physiology-Legacy Content*, 177(2):299–302.

[Zhang et al., 2013] Zhang, L., Lake, S., Lai, V., Picu, C., V.H., B., and M.S., S. (2013). A coupled fiber-matrix model demonstrates highly inhomogeneous microstructural interaction in soft tissues under tensile load. *J. Biomech. Eng.*, 135:011008.

[Zhang et al., 2018] Zhang, S., Zarei, V., Winkelstein, B. A., and Barocas, V. H. (2018). Multiscale mechanics of the cervical facet capsular ligament, with particular emphasis on anomalous fiber realignment prior to tissue failure. *Biomechanics and Modeling in Mechanobiology*, 17(1):133–145.

[Zulliger et al., 2004] Zulliger, M. A., Fridez, P., Hayashi, K., and Stergiopulos, N. (2004). A strain energy function for arteries accounting for wall composition and structure. *Journal of Biomechanics*, 37(7):989–1000.

# Appendix A

# Automatic Segmentation of Mechanically Inhomogeneous Tissues Based on Deformation Gradient Jump

Although the primary emphasis of this dissertation was to study the mechanics and failure of viscoelastic fiber networks, this appendix section briefly describes a method to automatically segment tissues into mechanically inhomogeneous regions, and provides two examples of the application of this technique. We use network theory to identify clustering within the network, and the network is then partitioned based on these clusters. While the segmentation process itself is not directly related to determining the mechanics of the network, the partitions resulting from segmentation of the network can be assigned different mechanical properties to simulate the behavior of inhomogeneous tissues.

The content of this appendix section is part of a research article published in *IEEE Transactions on Medical Imaging* by Witzenburg, Dhume, Lake, and Barocas [Witzenburg et al., 2014]. For a detailed description of the segmentation algorithm, and results from the entire set of simulated and experimental data sets used to test the algortihm, the interested reader is directed to the full research article. I contributed to the programming part of this study, and implemented the network partitioning algorithm using C and MATLAB [MATLAB, 2013].

## A.1 Introduction

Variations in properties, active behavior, injury, scarring, and/or disease can all cause a tissue's mechanical behavior to be heterogeneous. Advances in imaging technology allow for accurate full-field displacement tracking of both in vitro and in vivo deformation from an applied load. While detailed strain fields provide some insight into tissue behavior, material properties are usually determined by fitting stress-strain behavior with a constitutive equation. However, the determination of the mechanical behavior

of heterogeneous soft tissues requires a spatially varying constitutive model, i.e., one in which the material parameters vary with location. If the strain field is to be used for partitioning, the next issue is how to implement the strain-based segmentation process efficiently and effectively. Manual thresholding is common, but an automated scheme capable of determining partitions from a strain field would be attractive.

In this work, we developed an approach that computationally dissected the sample domain into many homogeneous subdomains, wherein subdomain boundaries were formed by applying a *betweenness*-based graphical analysis to the deformation gradient field to identify locations with large discontinuities. This novel partitioning technique successfully determined the shape, size and location of regions with locally similar material properties for: (1) a series of simulated soft tissue samples prescribed with both abrupt and gradual changes in anisotropy strength, prescribed fiber alignment, stiffness, and nonlinearity, (2) tissue analogs (PDMS and collagen gels) which were tested biaxially and speckle tracked (3) and soft tissues which exhibited a natural variation in properties (cadaveric supraspinatus tendon), a pathologic variation in properties (thoracic aorta containing transmural plaque), and active behavior (contracting cardiac sheet). The routine enables the dissection of samples computationally rather than physically, allowing for the study of small tissues specimens with unknown and irregular inhomogeneity.

## A.2 Methods

### A.2.1 Full-field displacement tracking

Accurate estimation of full-field displacements from motion capture of soft tissue deformation is crucial for tissue segmentation. Accordingly, high-resolution digital video was captured of various tissue equivalent and soft tissue samples during deformation and digital image correlation was utilized to determine full-field displacement per Raghupathy [Raghupathy and Barocas, 2010, Raghupathy et al., 2011]. The video was synchronized and downsampled to construct grayscale image sequences corresponding to the loading curves of each extension. The image of the sample before the start of test was used as the reference configuration. Using Abaqus (6.11, Simulia, Inc., Providence, RI), the tissue boundary was sketched on top of the reference image and meshed with quadrilateral elements. Successive pairs of images were correlated to track the movement of the mesh throughout the loading sequence. Displacement fields were constructed from movement of the mesh and smoothed to reduce noise.

### A.2.2 Deformation gradient jump calculations

The deformation gradient tensor at the midpoint of each element edge (Figure A.1) was calculated from the bilinear isoparametric representation of the displacement field. For each element edge, the deformation gradient tensor was calculated as fol-

lows:

$$F = \begin{bmatrix} \frac{\partial x}{\partial X} & \frac{\partial x}{\partial Y} \\ \frac{\partial y}{\partial X} & \frac{\partial y}{\partial Y} \end{bmatrix} = \begin{bmatrix} \frac{\partial x}{\partial \xi} & \frac{\partial x}{\partial \eta} \\ \frac{\partial y}{\partial \xi} & \frac{\partial y}{\partial \eta} \end{bmatrix} \begin{bmatrix} \frac{\partial X}{\partial \xi} & \frac{\partial X}{\partial \eta} \\ \frac{\partial Y}{\partial \xi} & \frac{\partial Y}{\partial \eta} \end{bmatrix}^{-1}$$

where $(X, Y)$ is the initial position, $(x, y)$ is the final position, and $(\xi, \eta)$ is the computational coordinate.

The deformation gradient tensor for each element edge point $j$ was

$$F = \left( \sum_{j=1}^{4} \begin{bmatrix} x^j \\ y^j \end{bmatrix} \begin{bmatrix} \frac{\partial \phi^j}{\partial \xi} & \frac{\partial \phi^j}{\partial \eta} \end{bmatrix} \right) \left( \sum_{j=1}^{4} \begin{bmatrix} X^j \\ Y^j \end{bmatrix} \begin{bmatrix} \frac{\partial \phi^j}{\partial \xi} & \frac{\partial \phi^j}{\partial \eta} \end{bmatrix} \right)^{-1}$$

where $\phi$ is the bilinear function and $j$ is the index variable looping through the four basis functions for a given element. All shared edges were identified (Figure A.1), and the deformation gradient jump was defined as the double contraction of the difference between the deformation tensors across the edge with itself,

$$\Delta_k = \sum_{i=4}^{4} \left( F_i^{element1} - F_i^{element2} \right)^2$$

where elements 1 and 2 are the two elements sharing the edge $k$ and $i$ is the index variable looping through the four components of the deformation gradient tensor.

### A.2.3 Tissue segmentation

The flow chart in Figure A.2 summarizes the tissue segmentation scheme. In order to segment the tissue into homogeneous subregions, the finite element geometry for a sample was converted into an equivalent unweighted network. A network node was created for each finite element and if two elements shared an edge, their corresponding network nodes were considered connected (Figure A.1). Once the unweighted network was constructed, it was analyzed to determine the shortest path between each pair of network nodes. Then, a betweenness value for each connection was determined using a breadth-first search algorithm (per [Newman, 2001]). The *betweenness* value for a connection, as defined by Newman [Newman, 2001, Newman, 2004], is the number of shortest paths between any given pair of nodes that run along that connection. If there was more than one geodesic path joining a pair of network nodes, then each path contributed a fractional amount to the betweenness. Next, the network connection betweenness values were multiplied by the deformation gradient jump for the corresponding finite element edge. Thus, the final weighted value of betweenness for each network connection was determined both by the sample geometry and by the deformation gradient jump. Following [Newman, 2001, Newman, 2004], the network connection with the largest value of weighted betweenness was removed. The new, less-connected network was then reanalyzed to determine the new set of shortest paths and the process was repeated. When the network split into disconnected subnetworks,

communities were formed, and the network modularity was calculated. Modularity [Newman, 2004] is defined to be the difference between the fraction of connections that fall within communities and the expected value of the same quantity if connections are assigned at random.

## A.3 Results

### A.3.1 Heterogeneous polydimethysiloxane (PDMS) sample

Deformation data from equibiaxial and two strip biaxial extensions performed on a heterogeneous PDMS cruciform was analyzed. The sum of the normalized deformation gradient jumps for the three extensions (equibiaxial, vertical strip biaxial, and horizontal strip biaxial) and the partitions resulting from the automatic segmentation scheme for the PDMS sample are shown in Figure A.3. It is readily apparent from Figure A.3a that the 3-D nature of the modification and the deformation leads to a thick ring of high deformation gradient jumps around the compliant central region rather than a sharp, well-defined boundary as would occur in a purely 2-D experiment. The partitioning scheme immediately and compellingly identified the compliant central region of the sample, Figure A.3b. Figure A.3c shows the modularity for the partitioning scheme as connections are removed. For this sample, we stopped the partitioning scheme after two communities had been formed.

### A.3.2 Arteriosclerotic plaque

A segment of fresh diseased thoracic human aorta was obtained from the Anatomy Bequest Program at the University of Minnesota. A portion of the ascending thoracic aorta was cut into a cruciform such that a large transmural arteriosclerotic plaque resided in the central region of the sample, and the circumferential and axial orientations of the aorta coincided with the cruciform axes. The sample then underwent an equibiaxial and two strip biaxial extension tests to obtain strain fields.

The sum of the normalized deformation gradient jumps from all three extensions for the sample containing the large arteriosclerotic transmural plaque is shown in Figure A.4a. The partitioning results are overlaid on an image of the intimal surface sample taken prior to testing in which visible location of the plaque was noted, arrow in Figure A.4b. The sample was segmented into 10 separate partitions. Of the resulting partitions, one encompasses the plaque with little extraneous tissue. In addition, other partitions seem to identify visually similar regions of the tissue. Figure A.4c shows the modularity for the partitioning scheme as connections are removed.

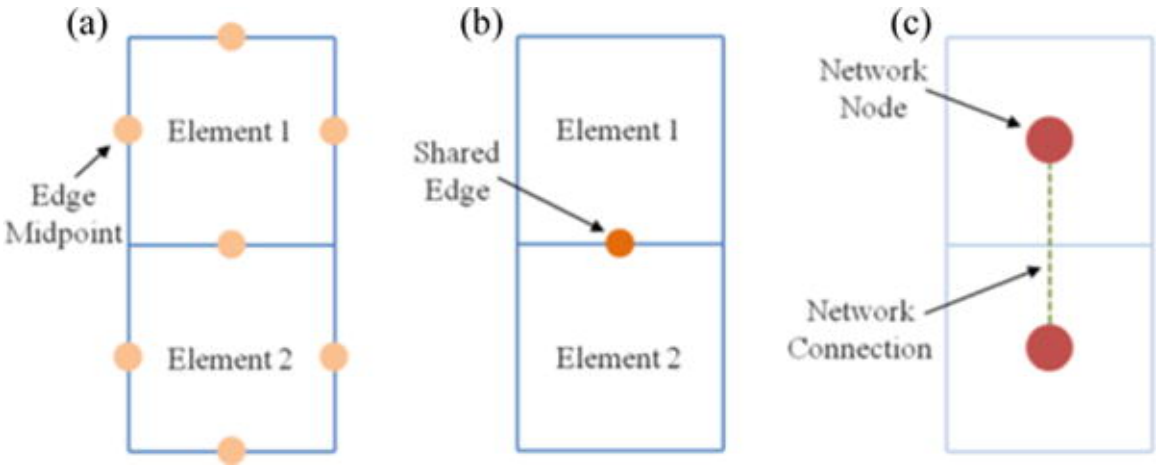


Figure A.1: (a) Schematic showing two finite elements indicating the midpoint of each element edge. A deformation gradient tensor was determined for every edge midpoint within the finite element (FE) mesh. (b) Schematic showing two finite elements indicating their shared edge. A deformation gradient jump was calculated for every shared edge. (c) Schematic showing two finite elements and indicating how the FE mesh geometry is converted into a network. The deformation gradient jump was utilized when weighting the network connection.

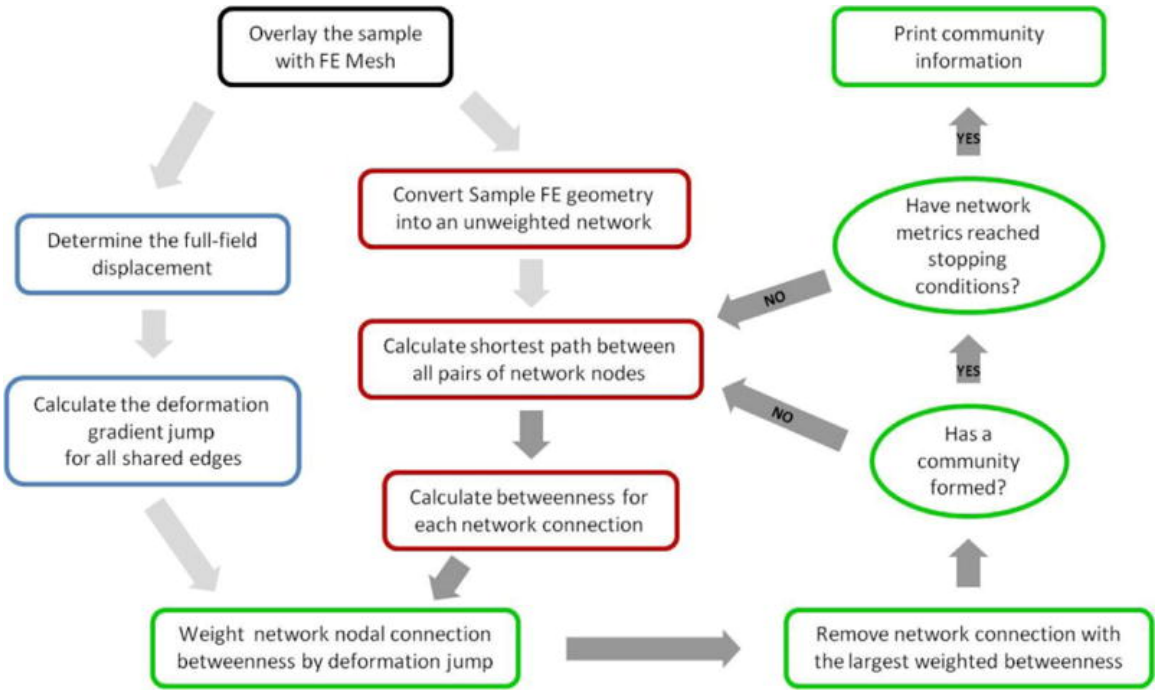


Figure A.2: Flowchart summarizing tissue segmentation scheme.

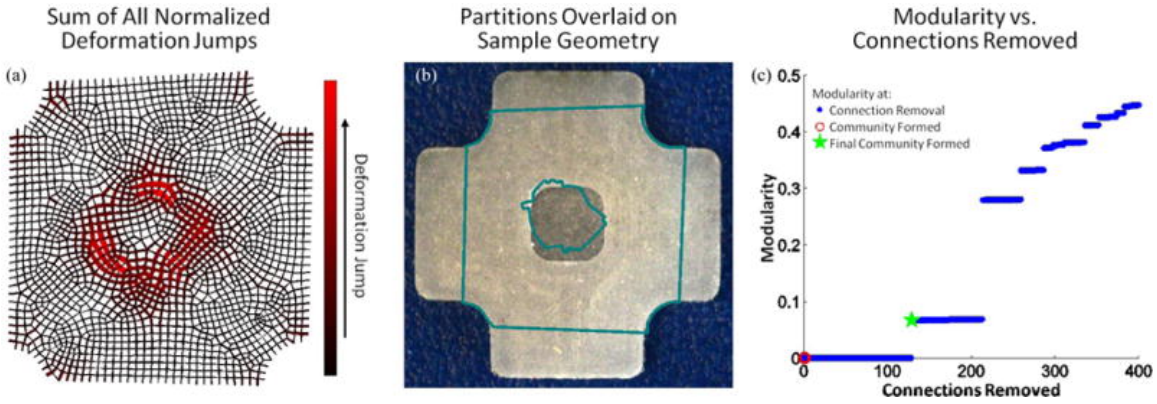


Figure A.3: (a) Sum of normalized deformation gradient jumps for all three extensions for the heterogeneous PDMS sample. (b) Partitions, overlaid on sample geometry, strongly mirror sample heterogeneity. (c) Modularity as a function of connections removed. Blue dots indicate values when a connection is removed and the green star mark when the final community formed.

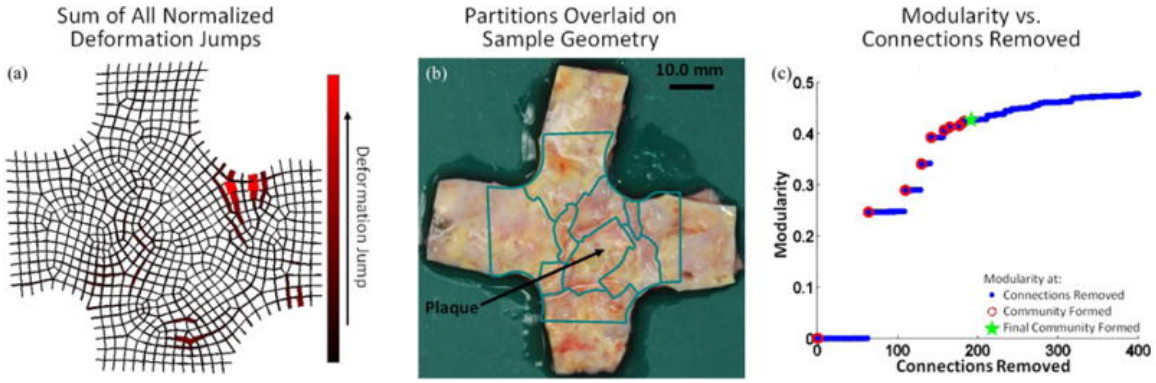


Figure A.4: (a) Sum of normalized deformation gradient jumps for all three extensions for the aortic sample containing a large arteriosclerotic transmural plaque. (b) Partitions are overlaid on an image of the sample taken prior to testing in which the plaque was identified. (c) The modularity as a function of connections removed. Blue dots indicate values when a connection is removed, open red circles indicate when a community is formed, and the green star mark when the final community was allowed to form.